

**ANDERSON-NEWNS HAMILTONIAN MOLECULAR DYNAMICS
APPROACH TO UNDERSTANDING ELECTROCHEMICAL DOUBLE
LAYER EFFECTS IN HYDROGEN ELECTROCATALYSIS**

by

Jon C. Wilson

A dissertation submitted to the Faculty of the University of Delaware in partial fulfillment of the requirements for the degree of Doctor of Philosophy in Chemical Engineering

Spring 2023

© 2023 Jon C. Wilson
All Rights Reserved

**ANDERSON-NEUNS HAMILTONIAN MOLECULAR DYNAMICS
APPROACH TO UNDERSTANDING ELECTROCHEMICAL DOUBLE
LAYER EFFECTS IN HYDROGEN ELECTROCATALYSIS**

by

Jon C. Wilson

Approved: _____
Millicent O. Sullivan, Ph.D.
Chair of the Department of Chemical and Biomolecular Engineering

Approved: _____
Levi T. Thompson, Ph.D.
Dean of the College of Engineering

Approved: _____
Louis F. Rossi, Ph.D.
Vice Provost for Graduate and Professional Education and
Dean of the Graduate College

I certify that I have read this dissertation and that in my opinion it meets the academic and professional standard required by the University as a dissertation for the degree of Doctor of Philosophy.

Signed:

Yushan Yan, Ph.D.
Professor in charge of dissertation

I certify that I have read this dissertation and that in my opinion it meets the academic and professional standard required by the University as a dissertation for the degree of Doctor of Philosophy.

Signed:

Dionisios Vlachos, Ph.D.
Professor in charge of dissertation

I certify that I have read this dissertation and that in my opinion it meets the academic and professional standard required by the University as a dissertation for the degree of Doctor of Philosophy.

Signed:

Marat Orazov, Ph.D.
Member of dissertation committee

I certify that I have read this dissertation and that in my opinion it meets the academic and professional standard required by the University as a dissertation for the degree of Doctor of Philosophy.

Signed:

Feng Jiao, Ph.D.
Member of dissertation committee

I certify that I have read this dissertation and that in my opinion it meets the academic and professional standard required by the University as a dissertation for the degree of Doctor of Philosophy.

Signed:

Stavros Caratzoulas, Ph.D.
Member of dissertation committee

I certify that I have read this dissertation and that in my opinion it meets the academic and professional standard required by the University as a dissertation for the degree of Doctor of Philosophy.

Signed:

Vasudevan Venkateshwaran, Ph.D.
Member of dissertation committee

ACKNOWLEDGMENTS

First, I give a big thank you to my advisors, Profs. Dion Vlachos and Yushan Yan. Dion has taught me a ton about surface chemistry and has exposed me to a wide breadth of the possibilities in catalysis. I am also grateful for his advice and feedback which has helped me to greatly hone my science communication skills. Yushan has similarly been a source of invaluable guidance. He has always encouraged me to zoom out and think about the big picture of our work, which has made a big impact on how I approach scientific problems and career decisions. It has been a fascinating journey to explore the theory of the electrochemical interface, and I believe we both learned a lot from each other!

I also thank the other members of my committee, Profs. Marat Orazov, Feng Jiao, Dr. Stavros Caratzoulas, and Dr. Vasu Venkateshwaran. They have all provided unique perspectives and valuable feedback on my project, which I greatly appreciate. In particular, I thank Dr. Stavros Caratzoulas for his advice and hands-on support with my research. We have had countless fruitful discussions over the last several years that I have valued highly. His high-standards and rigorous approach to chemical physics has continuously challenged me and has made me a better scientist.

The members of the Yan and Vlachos groups have also been a huge source of support for me. We have persevered through globally difficult times that have been extremely challenging for all of us, and the mutual support we provided each other has kept me going throughout it all. In no particular order, I would like to thank Jon Lym, Prof. Ezgi Toraman, Yifan Wang, Zhaoxing Wang, Natalia Rodriguez-Quiroz, Lina

Lee, Alfred Worrad, Sophia Kurdziel, Stephen Giles, Jared Nash, Brian Setzler, Nicholas Oliveira, and Stephanie Matz. Thank you and keep doing awesome things!

I also give a very special thank you to my closest friends, Himaghna Bhattacharjee, Divyanshi Srivastava, Robert O’Dea, Catherine Weiss, and Douglass Nmagu. We have had some really amazing and unexpected adventures together, and I look forward to more of them in the future. We’ve brought each other a lot of happiness and great memories, and even though many of them have moved away, I look forward to visiting them and learning about the exciting things they are doing in the future.

My parents Lisa and Dan Wilson have been my biggest supporters of all. Since I was young, they have pushed me to be curious and to follow my interests. I was homeschooled for many years, and I give my mom a huge amount of credit for her dedication to my education- I have not always been the most focused or studious person! Both my parents, and particularly my dad, have been very engaged with my graduate research along the way. I appreciate their patience and readiness to ask thoughtful questions about my work, even though my research has often made me hard to reach and generally a bit difficult! Outside of the academic world, I am grateful that they have instilled in me a love for nature, gardening, and cooking. I love you guys!

Lastly, I thank my partner, Kelly Jacobs. I never expected to meet my partner during a global pandemic, and I’m doubly surprised that we didn’t even meet through the internet! In the few years we’ve known each other, we have become an awesome team and have made some unforgettable memories. Her honesty, strength, empathy, and passionate attitude are just a few of the reasons why I love her. Thank you, Kelly!

TABLE OF CONTENTS

LIST OF TABLES	x
LIST OF FIGURES	xi
ABSTRACT	xx

Chapter

1	INTRODUCTION	1
1.1	Motivation: Green Hydrogen in the Energy Transition	1
1.2	Practical Hydrogen Electrocatalysis and Hydroxide Exchange Membrane Fuel Cells & Electrolyzers	9
1.3	A Primer on the Electrochemical Interface	13
1.4	Recent Progress in pH-dependent HOR/HER Kinetics and Hydrogen Electrocatalysis Simulation	20
1.4.1	Thermodynamic Descriptors & Hydrogen Binding Energy	20
1.4.2	Hydroxide Binding Energy	22
1.4.3	Beyond Thermodynamic Descriptors: Electrochemical Interface Effects	24
1.4.4	Prospects for Insights from Theory	26
1.5	Dissertation Overview	28
2	EMBEDDED ANDERSON-NEUNS HAMILTONIAN MOLECULAR SIMULATION METHODS AND DEVELOPMENT	31
2.1	Introduction and Theory	31
2.2	Electronic Hamiltonian details.	34
2.3	Constant potential method.	36
2.4	Vertical energy gap and interaction potentials.	37
2.5	Summary	41
3	INSIGHTS INTO SOLVENT AND SURFACE CHARGE EFFECTS IN HYDROGEN ELECTROCATALYSIS	42
3.1	Abstract	42
3.2	Introduction	43

3.3	Results	47
3.3.1	Diabatic Free Energy Curves for HER/HOR.	47
3.3.2	Potential-dependent solvent dynamics.	51
3.3.3	Adiabatic Free Energy Surfaces.	53
3.3.4	Implications for pH-dependent HOR/HER kinetics.	59
3.4	Conclusions	62
3.5	Computational Resources	63
3.6	Methods	64
3.6.1	Electronic Hamiltonian.	64
3.6.2	Diabatic and Adiabatic Simulations.	65
3.6.3	Electrolyte Interaction Potentials and Simulation Cell Details. ..	66
4	INVESTIGATING NON-COVALENT CATION EFFECTS IN THE VOLMER STEP ON PT (111) WITH MOLECULAR DYNAMICS	67
4.1	Introduction	68
4.2	Results	70
4.2.1	Z Distributions of Ionic Species	70
4.2.2	Cylindrical Pair Correlations	74
4.2.3	Contributions to the electrostatic potential of H ⁺ in the double layer	77
4.2.4	Diabatic Electron Transfer Analysis	79
4.2.5	Adiabatic Free Energy Surfaces	85
4.2.6	Entropic contributions to H ⁺ free energies in the EDL	88
4.3	Implications for Cation-Dependent and pH-dependent HOR/HER Kinetics.	90
4.4	Conclusions	93
4.5	Computational Resources	93
5	FUTURE DIRECTIONS	94
5.1	Introduction	94
5.2	The role of hydroxide in alkaline hydrogen electrocatalysis.	94
5.3	Opportunities for improved constant voltage techniques	97
	REFERENCES	101

Appendix

A	SUPPLEMENTARY INFORMATION FOR CHAPTER 3	112
	Double layer charging relation	112
	Water equilibrium orientation around H^+	114
	Potential-dependent interfacial water configurations	116
	Solvation water dipole autocorrelation relaxation.....	118
	Proton electrostatic potential autocorrelation functions	120
	Effect of overpotential on adiabatic ET.....	121
	Hydrogen – water coordination numbers for adiabatic ET	123
	Referencing procedure for proton free energies	125
	Coordination Numbers of water around H^{\ddagger}	128
B	SUPPLEMENTARY INFORMATION FOR CHAPTER 4.....	129
	Cs^+ Cylindrical Pair Correlation Functions	129
	H^+ Radial Distribution Functions	130
	Diabatic free energies for H^+/H redox in 1M CsCl and 1M NaCl	131
	Cylindrical pair correlation functions for OHL Cs^+ atoms.....	132
	Hydrogen bonding and water dipole angle distributions for waters adsorbed on Pt (111).....	133

LIST OF TABLES

Table 1. Interaction parameters for the redox ion-system potentials.	40
---	----

LIST OF FIGURES

- Figure 1.1. Cost decline trends for renewable energy technologies.** A) solar PV modules and B) hydrogen electrolyzers. Adapted from Way et al⁵. The forecast shows the expected cost declines, 50% CI (dark shading) and 95% CI (light shading) based on historical exponential growth trends. The red lines show past forecasts from the International Energy Agency, which do not use Wright’s law. The inset shows the Wright’s law relationship between production cost and number of cumulative units produced. In the inset, the vertical lines show the projected cost and total deployment by 2050 three possible energy transition scenarios: no transition, slow transition, and a fast transition. The fast transition case corresponds to continued growth at the historically observed rate. Note that electrolyzers have wider confidence intervals since the technology is younger and less data is available. 4
- Figure 1.2. Schematic drawing of the “duck curve” as observed in springtime in California.** As the deployment of solar PV has increased exponentially over the last decade, the intraday variation in net load on the electrical grid has increased. The inset shows how solar PV generation output varies over the course of a typical day. 5
- Figure 1.3. Breakdown of global energy-related CO₂ emissions by sector in 2015.** Adapted from the IRENA Hydrogen from renewable power: Technology outlook for the energy transition report. Green hydrogen can be used to abate carbon emissions in sectors which have historically had no economically viable option for decarbonization. 7
- Figure 1.4. PEMEL vs. HEMEL chemistry and device configuration.** On the left, a PEM device is shown. In a PEMEL, water is split at the anode and H⁺ migrates across the proton-conducting membrane (pink) from the anode to the cathode to form H₂. On the right, in a HEM device, water is split at the cathode and OH⁻ ions migrate across the hydroxide-conducting membrane (light green) from the cathode to the anode. In both cases, the anode and cathode are cast on either side of the membrane and form the MEA. Figure created by Alexandra Oliveira. 11

- Figure 1.5. pH-dependent catalyst activity change on typical HOR/HER catalysts materials.** Reproduced from Durst et al¹⁷. The exchange current density, a measure of catalyst activity, decreases by about two orders of magnitude in pH 13 vs. pH 0 on typical catalysts. Pt/C, Ir/C, and Pd/C are platinum, iridium, and palladium catalysts cast on carbon supports..... 12
- Figure 1.6. Atomistic representation of the electrochemical interface between a platinum (111) electrode surface and an aqueous electrolyte containing NaCl.** At the surface, the water molecules form a more planar structured hydrogen bonding network compared to electrolyte in the bulk solution. Water molecules are shown in red and white and NaCl atoms are shown in green and orange, respectively..... 14
- Figure 1.7. Summary sketch of the process of solvent reorganization and non-adiabatic electron transfer.** Non-adiabatic electron transfer can be described as a rapid “jump” from one curve to another without change in nuclear positions, shown on the left. The initial and final states correspond to the reduced and oxidized states at equilibrium solvation. The solvent must reorganize to reach the crossing point (where the energies are equal) of the two free energy curves before redox is likely to occur. After redox, the solvent relaxes to equilibrium solvation for the product states. The central ion is the electron donor to the acceptor ion shown in gray. 16
- Figure 1.8. Summary sketch of adiabatic electron transfer for H/H⁺ redox.** When there is strong donor-acceptor electronic coupling, electron transfer proceeds along a ground state free energy surface. The equivalent weak-coupling free energies are traced with the dotted lines. The relationship between the electronic coupling magnitude, Δ , and the activation barrier height in adiabatic electron transfer is shown. Strong coupling between hydrogen and the electrode electronic states is the essence of what enables catalysis in hydrogen fuel cells and electrolyzers. 19
- Figure 1.9. Volcano plot of experimental HOR/HER activity on various monometallic catalysts versus catalyst hydrogen binding energy computed from DFT.** Reproduced with permission from Sheng et al²⁵. On the left branch, the hydrogen binding energy is too strong, and on the right branch, hydrogen binding is too weak. 21

Figure 1.10. 3D HER activity volcano plot with OHBE and HBE as kinetic descriptors. Reproduced with permission from McCrum et al⁴⁰. In this model, both HBE and OHBE must be neither too strong nor too weak for fast alkaline HER kinetics. 23

Figure 3.1. Schematics of Volmer reaction along the collective solvent coordinate and proton-surface distance, z. A) Illustration of chemisorption and solvent reorganization around H⁺ in the Volmer step at charged Pt (111). Approaching the electrode, H⁺ moves through the surface field and loses significant solvation energy before reaching the charge transfer transition state. B) Diabatic free energy curves of the H⁺/H pair at fixed z; solvent reorganization energy, λ , and overpotential, η , are shown. Changes in surface charge can potentially modulate solvent polarization fluctuations, which in turn determines the free energy curvature (green) and solvent reorganization energy. C) Free energies of the H⁺/H pair projected onto the z coordinate. Reduced hydrogen at the surface is denoted H^{*}. Surface charge can affect the energy to move H⁺ to the double layer, $\Delta G(\text{H}^+ \rightarrow \text{H}_{\text{dl}}^+)$, by changes in electrostatics and solvation. In the adiabatic representation, H^{*} has a partial charge, and thus HBE is also affected by electrostatics. More broadly, the change in double layer structure and composition with changing surface charge can also indirectly affect the free energy of hydrogen near the surface. 45

Figure 3.2. Diabatic free energies for H⁺ and reduced H along the solvent coordinate at fixed z. The reduced state free energies are calculated by the relation $F^{\text{H}}(\Delta e) = F^{\text{H}^+}(\Delta e) + \Delta e + \epsilon_a - \epsilon_f$ and the overpotential is set to $\eta = 0$ in each case for ease of comparison. A) $z = 4.0 \text{ \AA}$, B) $z = 3.0 \text{ \AA}$, C) $z = 2.0 \text{ \AA}$. The cell electrostatic potential is set to $V - V_{\text{pzc}} = 0 \text{ V}$, i.e., the PZC for both electrodes. The orange and blue curves correspond to the oxidized and reduced states, respectively. Parabolas fitted near the proton minimum are shown as dashed lines. 48

Figure 3.3. Effect of surface charge on diabatic free energies at fixed z. A) solvent reorganization λ ; B) equilibrium Δe value for H⁺, $\Delta e^{\text{H}^+}_{\text{min}}$; C) free energy to reach the diabatic crossing with the effect of overpotential subtracted off, $\Delta F^{\ddagger}_{\eta=0}$; and D) reduction free energy change, ΔF , for the diabatic curves where $F^{\text{H}}(\Delta e) = F^{\text{H}^+}(\Delta e) + \Delta e$. The blue, red, green, and purple curves are computed from diabatic free energy curves at electrode voltages relative to PZC of $V - V_{\text{pzc}} = 0 \text{ V}$, -0.5 V , -1 V , -2 V , respectively. 49

Figure 3.4. Dipole vector autocorrelation function for water molecules near the Pt (111) electrode. A) Double layer waters near the outer Helmholtz layer within $4 < z < 5$ Å. B) Adsorbed waters where $z < 3$ Å. Surface water is attracted to the Pt surface, and the lattice spacing of Pt (111) is suitable for water to form a network of hydrogen bonds parallel to the electrode plane. Consequently, the reorientation time of water increases at the surface due to confinement effects. (Blue, red, and green curves correspond to water near the electrode with voltages of $V - V_{pzc} = 0$ V, -1 V, -2 V, respectively.)..... 52

Figure 3.5. Simulated adiabatic free energy surfaces of the H^+/H redox pair near a Pt (111) electrode as functions of the collective solvent coordinate, Δe , and the H's z-coordinate along the normal to the surface, at varying cell electrostatic potentials: A) $V - V_{pzc} = 0$ V B) $V - V_{pzc} = -1$ V C) $V - V_{pzc} = -2$ V. The Fermi level is set such that $\epsilon_a - \epsilon_f = -10.19$ eV. Minimum free energy paths (MFEP) are shown as traced solid lines. The white filled shapes mark the H^* minima, the teal shapes mark the redox saddle point, H^\ddagger , and the purple shapes mark the H^+_{dl} minima at negative voltages. The hydrogen adsorption energy is calculated as the free energy difference between the H^* minima and H^+ in the bulk, which is the reference for all cases..... 54

Figure 3.6. Further analysis of the adiabatic free energy surfaces at varying $V - V_{pzc}$. A) Contours of expected H orbital occupancy $\langle n_a \rangle$ versus the collective solvent coordinate, Δe , and the z-coordinate of redox H along the normal to the surface. B) Free energy profiles along respective MFEPs of adiabatic free energy surfaces shown previously in Figure 4. C) Average electrostatic potential energy $V_\phi = q_H \langle \phi \rangle$ experienced by H^* , H^\ddagger , H^+_{dl} at the three applied potentials. The partial charge of hydrogen is related to its occupancy by $q_H = 1 - \langle n_a \rangle$. In A: The overlaid solid, dotted, and dashed lines are the minimum free energy paths for the free energy surfaces corresponding to $V - V_{pzc} = 0$ V, -1 V, -2 V, respectively. In B: White shapes: Adsorbed H (H^*). Teal shapes: Redox transition states (H^\ddagger). Purple shapes: Proton minima in the double layer (H^+_{dl}). Pink circle: bulk proton reference state (H^+_{bulk}). In C: the bars correspond to 0 V (diagonal hatches), -1 V (dots), and -2 V (horizontal hatches). V_ϕ for the reference, H^+_{bulk} , is shown for comparison to H^+_{dl} 56

- Figure 4.1. Z distribution functions for supporting electrolyte species above the Pt (111) surface.** A) Cs⁺ in 1M CsCl, B) Cl⁻ in 1M CsCl, C) Na⁺ in 1M NaCl, D) Cl⁻ in 1M NaCl. The coverages shown in A and C are obtained by integration of the first peak of the ZDF. Colors are $V - V_{pzc} = 0$ V, -1 V, -2 V in blue, red, and green, respectively. In this case, the distributions are obtained when no redox hydrogen is in the system to enable a larger timestep ($\Delta t = 2$ fs, 20ns sampling) and to show how the electrolyte ions spatially arrange before H⁺ approaches the surface..... 72
- Figure 4.2. Cylindrical pair correlation functions ρ_{ij}/ρ_{bulk} between the H⁺ ion and supporting electrolyte ions in CsCl and in NaCl.** The single H⁺ ion is placed at fixed z in the cell in each case. A-D) z = 6 Å for H⁺, E-H) z = 4 Å, I-L) z = 3 Å, M-P) z = 2 Å. From left to right, the columns correspond to H⁺/Cs⁺, H⁺/Na⁺, Gray curves on the plot correspond to radial distance isolines $r = (r_{||}^2 + r_z^2)^{1/2}$ 76
- Figure 4.3. Electrostatic potential decomposition of the H⁺ ion at various fixed z above the electrode surface.** A) proton-water electrostatic potential, B) proton-electrolyte electrostatic potential, including the sum of both water and the supporting electrolyte ions. The CsCl and NaCl cases are shown in purple and green, respectively. 78
- Figure 4.4. Diabatic free energy analysis for H⁺/H redox at fixed z in 1M CsCl.** A) Schematic showing how λ , Δe_{min} , and ΔF are calculated from the simulated free energies. Values for B-D are for 1M CsCl. B) Solvent reorganization energy, λ , C) equilibrium ΔE value for H⁺, $\Delta e^{H^+}_{min}$, D) Diabatic reduction free energy change, ΔF 81
- Figure 4.5. Further analysis of diabatic free energies for H⁺/H redox at fixed z.** Differences in values calculated for the 1M CsCl cases relative to the 1M NaCl cases (notated using $\Delta^{Cs_{Na}}$) are shown. A) differences in λ values calculated by the vertical difference at $\Delta e^{H^+}_{min}$, B) Differences in the intrinsic barrier for diabatic crossing when $\Delta F = 0$, ΔF^\ddagger_0 , C) differences in $\Delta e^{H^+}_{min}$ values, D) differences in Δe^H_{min} values, and E) differences in H⁺ reduction ΔF values..... 82
- Figure 4.6. Adiabatic free energy surfaces for H⁺/H redox with 1 M CsCl and 1M NaCl electrolytes.** A) 1 M CsCl, B) 1 M NaCl, C) minimum free energy pathways for the CsCl case (solid) and the NaCl case (dashed). For the electronic model, the Fermi level is set such that $\epsilon_a - \epsilon_f = -12.14$ eV. The cell electrostatic potential is set to $V - V_{pzc} = 0$ V..... 86

Figure 4.7. Entropy contribution to the free energy of adiabatic ET in the Volmer step. Entropy is calculated as a function of the collective coordinate ΔE and the redox hydrogen distance from the surface, z , at 300K. A) $-T\langle S \rangle$ for H⁺/H redox in 1M CsCl, B) $-T\langle S \rangle$ for H⁺/H redox in 1M CsCl, C) entropy contribution along the Volmer step minimum free energy pathways (MEP) from A) and B) projected onto 1D. The dashed line is the MFEP for the NaCl system and the solid line is for the CsCl system. In A) and B), data in the white regions are omitted due to limited sampling. The color bar scale is $-T\langle S \rangle$ in eV. ... 89

Figure A.1. Potential profile and double charging relation in capacitor cell with neat water. A) Diagram of capacitor cell with gap $D = 50 \text{ \AA}$ between image planes. Waters are placed between two slabs with Pt (111) facets exposed. B) planar-averaged Poisson potential along the length of the capacitor at various applied voltages, C) average surface charge as a function of applied potential, $V - V_{pzc}$. The slope of the line is the double layer capacitance, $C_{dl} \cong 6 \text{ \mu F/cm}^2$, and is due to reorientation of water molecules. (In B, the blue, red, and green curves correspond to $\Delta V = 0 \text{ V}$, 2 V , and 4 V , respectively.) 113

Figure A.2. Angular distribution functions of waters solvating the proton. Statistics collected for the redox H oxidized diabatic state at fixed z . A), B), C): $z = 6.0 \text{ \AA}$ and D), E), F): $z = 2.0 \text{ \AA}$ for three different voltages. $V - V_{pzc} = 0 \text{ V}$, -1 V , -2 V correspond to blue, red, and green, respectively. 115

Figure A.3. Potential-dependent interfacial water configurations. A) Characteristic snapshot of adsorbed water configurations at different voltages $V - V_{pzc} = 0 \text{ V}$, -1 V , -2 V (top to bottom). B) z -distribution functions of oxygen atoms belonging to water. C) z -distribution functions of hydrogen atoms belonging to water. D) distribution of $\cos(\theta)$ of adsorbed water's dipole angles with respect to the surface normal. E) probability distribution of the numbers of hydrogen bonds (donors + acceptors) per adsorbed water..... 117

Figure A.4. Dipole moment autocorrelation functions for waters solvating H⁺. The results are plotted for the proton at fixed z where A) $z = 6.0 \text{ \AA}$ B) $z = 2.0 \text{ \AA}$ for three different voltages. $V - V_{pzc} = 0 \text{ V}$, -1 V , -2 V shown in blue, red, and green, respectively. 119

Figure A.5. Autocorrelation for electrostatic potential of the proton at fixed z .
 The rate of relaxation of the electrostatic potential is proportional to the solvation time of the ion. Close to the surface, the solvation becomes more sluggish due to confinement of water on Pt (111). At more negative potentials, the librational contribution at short times (< 50 fs) is faster, and solvation occurs more rapidly. A) $z = 2.0 \text{ \AA}$, B) $z = 4.0 \text{ \AA}$, C) $z = 6.0 \text{ \AA}$ 121

Figure A.6. Raising the Fermi level biases the reaction to reduction. 2D adiabatic surfaces analysis for H^+/H redox near Pt (111). Here, the electrode electrostatic potential $V - V_{pzc}$ and the Fermi level are connected. Three cases are shown: $V - V_{pzc} = 0 \text{ V}$ with $\epsilon_a - \epsilon_f = -10.2 \text{ eV}$, $V - V_{pzc} = -1 \text{ V}$ with $\epsilon_a - \epsilon_f = -11.2 \text{ eV}$, and $V - V_{pzc} = -2 \text{ V}$ with $\epsilon_a - \epsilon_f = -12.2 \text{ eV}$. **A)** the MFEP along the reaction coordinates ΔE and z for the three electrode potentials. **B)** the free energies along the MFEP projected onto 1D. **C)** the free energy changes for the steps along the MFEP are shown. **D)** the average electrostatic potential experienced by hydrogen is shown for H^* , H^\ddagger , and $H^{+_{dl}}$. **E)** the average expected occupancy is shown for H^* and for H^\ddagger . (In A and B, the solid, dotted, and dashed lines correspond to the 0 V, -1 V, and -2 V cases, respectively. In C, D, and E, the diagonal bar hatches, dotted hatches, and horizontal bar hatches correspond to the 0 V, -1 V, and -2 V cases, respectively.) 122

Figure A.7. Coordination numbers of water atoms around the redox hydrogen for adiabatic ET at fixed hydrogen z and varied cell voltage $V - V_{pzc}$. The Fermi level is set to $\epsilon_a - \epsilon_f = -10.2 \text{ eV}$. At $z > 2.0 \text{ \AA}$, hydrogen is oxidized, and at $z \leq 2.0 \text{ \AA}$, hydrogen is reduced. Changing $V - V_{pzc}$ only slightly affects the equilibrium solvation of hydrogen. A) CNs of water O around redox H at $V - V_{pzc} = 0 \text{ V}$. B) CNs of water O around redox H at $V - V_{pzc} = -2 \text{ V}$. C) CNs of water H around redox H at $V - V_{pzc} = 0 \text{ V}$. D) CNs of water H around redox H at $V - V_{pzc} = -2 \text{ V}$ 124

Figure A.8. Coordination numbers (CN) of water atoms around redox H at the transition state from adiabatic ET simulations. Here we set $\epsilon_a - \epsilon_f = -10.2$ eV. A) H^\ddagger / water-hydrogen CNs. B) H^\ddagger / water-oxygen CNs. At $V - V_{pzc} = -2$ V, there is higher water-H density near H^\ddagger around $r = 2.5$ Å and slightly lower water - O density in the 2nd layer of solvating waters, $r > 2.5$ Å. Since H^\ddagger has a partial positive charge, the change in CNs imply less attractive H^\ddagger /water interactions, thus the solvent is polarized further away from equilibrium solvation at the negative voltage transition state. (Blue: electrode at $V - V_{pzc} = 0$ V, Green: $V - V_{pzc} = -2$ V. 128

Figure B.1. Surface Cs⁺ cylindrical pair correlations. A) conditional pair correlations between surface Cs⁺ atoms (within $z < 3$ Å of the surface) and A) other Cs⁺ atoms, B) water oxygen atoms. The average spacing between surface Cs⁺ atoms is about $r_{||} = 5.2$ Å, which is slightly smaller than the diameter of the first solvation shell of $d \cong 6$ Å, indicating a high degree of overlap between OHL Cs⁺ solvation shells. 129

Figure B.3. Radial distribution functions of electrolyte ions around H⁺ at various fixed distances z from the Pt surface. The surface potential is set to $V - V_{pzc} = 0$ V. A) H^+/Cs^+ RDFs in 1M CsCl, B) H^+/Cl^- RDFs in 1M CsCl, C) H^+/Na^+ RDFs in 1M NaCl, D) H^+/Cl^- RDFs in 1M NaCl. Error bars are estimated from the variance in distribution function bin block averages after dividing the trajectories into five blocks. 130

Figure B.3. Diabatic free energy curves for H⁺/H redox at fixed z; used to produce Figure 4.3. A-F) Free energies in 1 M CsCl where z of Green: neutral H free energies F^H calculated from $F^H(\Delta e) = F^{H^+}(\Delta e) + \Delta e$. Error bars are shown but are small. 131

Figure B.4. Cylindrical pair correlation functions ρ_{ij}/ρ_{bulk} between the reduced redox H at fixed z and supporting electrolyte ions in 1 M CsCl and in 1 M NaCl. A-D) $z = 3$ Å, E-H) $z = 2$ Å. From left to right, the columns correspond to H/Cs⁺, H/Na⁺, Gray curves on the plot correspond to radial distance isolines $r = (r_{||}^2 + r_z^2)^{1/2}$ 132

Figure B.5. Adsorbed water hydrogen bonding & water dipole angle statistics.

Water molecules are included in the statistics if its oxygen z position is less than $z = 3.0 \text{ \AA}$. Statistics are collected from a trajectory of 10 ns with no proton included in the cell. A) Mean and distribution of the number of hydrogen bonds (donors + acceptors) per adsorbed water in 1 M CsCl and B) 1 M NaCl. C) Distribution of water dipole vector angles with respect to the surface normal vector in 1 M CsCl at $V - V_{pzc} = 0 \text{ V}$ and D) 1 M NaCl. Cs^+ adsorption is more favorable and significantly disrupts hydrogen bonding. As the surface potential is set more negatively, Na^+ has a stronger tendency to migrate to the surface and disrupt the hydrogen bonding network. Cs^+ decreases the number of water molecules hydrogen bonded parallel to the surface compared to Na^+ . Instead, more water hydrogens point away from the surface.... 133

ABSTRACT

Today, green hydrogen is at the cusp of widespread adoption. However, to meet critical CO₂ emission reduction targets sooner, faster scale up of green hydrogen infrastructure is needed. To that end, progress in device design is needed to reduce the material costs in fuel cell and electrolyzer production.

The development of hydroxide exchange membrane fuel cells (HEMFCs) and electrolyzers (HEMELs) is a promising route towards lower device costs. However, design challenges remain in the way of commercialization. The hydrogen oxidation (HOR) and evolution reaction (HER) kinetics are much slower at high pH. Several theories have been proposed to explain pH-dependent kinetics, however, debate is ongoing. Changes in interfacial electrostatic potential and the presence of supporting electrolyte ions greatly affect HOR and HER kinetics but are not well understood.

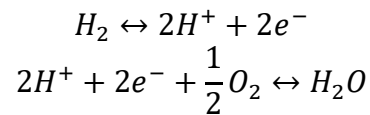
To clarify how interfacial effects are related to kinetic trends in HOR and HER, we developed a composite model to simulate the rate limiting Volmer reaction step. We embed an Anderson-Newns Hamiltonian electronic model for the redox event into classical molecular dynamics simulation of the Pt (111) – aqueous electrified interface. We show how solvent reorganization energy is not sensitive to interfacial electric fields as was previously thought. Instead, changes in the interfacial electrostatic potential affect the redox activation barrier by changing the local potential of interfacial H⁺. Second, we show that slower kinetics in Cs⁺-containing electrolyte versus Na⁺-containing electrolyte are governed by increased solvent reorganization energy in the Cs⁺ case as well as increased entropy loss as H⁺ approaches the surface.

Chapter 1

INTRODUCTION

1.1 Motivation: Green Hydrogen in the Energy Transition

The idea of using hydrogen as a fuel and energy storage medium at large scales took shape in the early 1970s. At that time, Turhan Nejat Veziroğlu, John Appleby, and John Bockris popularized the concept of the “hydrogen economy” in a series of conference meetings and publications¹. The basic principle is to use electricity to split water into hydrogen and oxygen, called electrolysis, and store the hydrogen to be sold or used later for a variety of applications. In the reverse direction, hydrogen can be used as a fuel and oxidized in a device called a fuel cell to create electricity. The basic reaction steps are as follows:



In a fuel cell, H_2 is consumed at the anode catalyst and O_2 is consumed to produce water at the cathode catalyst, and vice versa for an electrolyzer. Because the reactions produce no CO_2 and the electricity for electrolysis can be generated from renewable energy, storing energy as hydrogen fuel is a promising alternative to using fossil fuels. Such hydrogen produced from renewable electricity is called “green hydrogen.” Interest in producing green hydrogen at large scales has waxed and waned over the years, but finally, we are now approaching a turning point for the feasibility of the hydrogen economy. In this section, I will explain the case for green hydrogen.

Since the popularization of the “hydrogen economy” concept in the 1970s, humanity has released an additional 1,000 gigatons of CO₂ into the atmosphere, increasing the average global temperature by at least 1.1 °C relative to the beginning of the industrial revolution as of 2022². The global urgency to transition away from fossil fuels has reached anxious new heights, and a decidedly vast body of evidence shows that drastic curtailments of CO₂ emissions are necessary within the next two decades to avoid the worst effects of climate change^{2,3}. The Intergovernmental Panel on Climate Change (IPCC) and scientific community have warned that warming above 1.5°C will increasingly magnify the severity of global sea level rise, hurricanes, heat waves, and extreme drought, as well as accelerate species loss and extinction^{2,4}. Continued warming is expected to worsen our collective mental health, accelerate the spread of tropical diseases, decrease crop yields, and dramatically increase the number of refugees fleeing natural disasters⁴. Both policy change and technological progress must develop in tandem to phase out the combustion of fossil fuels as quickly as possible.

Fortunately, progress in clean energy technologies have given us one renewed cause for optimism. The levelized cost of energy (LCOE) sourced from wind turbines and solar photovoltaics (PV) have dropped by an estimated 99.5% and 90% in the past 40 years, respectively⁵. In 2021, the LCOE of wind and solar PV range from \$26 – 50MWh⁻¹ and \$30 – 40MWh⁻¹, respectively, making them significantly cheaper to build than new gas combined cycle or coal fired plants in nearly all situations⁶.

Production cost trends for wind and solar have closely followed an empirical phenomenon called Wright’s law, which states that for every cumulative doubling of production of some good, the production costs decrease by a fixed percentage⁵. The

fixed percentage is called the “learning rate” and reflects how rapidly manufacturers learn from accumulated experience to reduce production costs for a particular good. Additionally, the learning rate is also likely governed by improved production efficiencies that accompany economies of scale. This power law scaling has been observed for many technologies, including transistors, televisions, cars, batteries, hydrogen electrolyzers, and more^{5,7}. Critically, once the Wright’s law trend is established for a particular product, the exponential growth and power-law cost declines for that product tend to persist until the market becomes saturated. Moreover, historical cumulative production and cost data can be used to produce accurate forecasts of future product costs^{5,7}. Reproduced from Way et al., Figure 1.1 shows the observed Wright’s law trend for the capital cost of solar PV and hydrogen electrolyzers and forecasted cost reductions⁵. Renewable technologies have become significantly less expensive over the last several decades, and the various costs associated with these technologies are expected to continue following this downward trend.

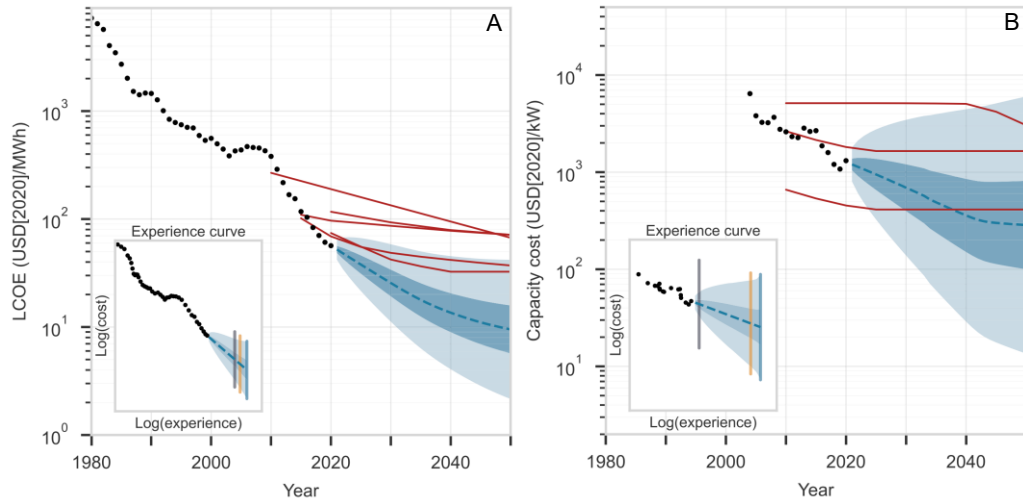


Figure 1.1. Cost decline trends for renewable energy technologies. A) solar PV modules and B) hydrogen electrolyzers. Adapted from Way et al⁵. The forecast shows the expected cost declines, 50% CI (dark shading) and 95% CI (light shading) based on historical exponential growth trends. The red lines show past forecasts from the International Energy Agency, which do not use Wright’s law. The inset shows the Wright’s law relationship between production cost and number of cumulative units produced. In the inset, the vertical lines show the projected cost and total deployment by 2050 three possible energy transition scenarios: no transition, slow transition, and a fast transition. The fast transition case corresponds to continued growth at the historically observed rate. Note that electrolyzers have wider confidence intervals since the technology is younger and less data is available.

Without scalable energy storage, wind and solar deployment cannot continue at its current growth rates. Consequently, crucial CO_2 emission reduction targets may be jeopardized. The intermittency of renewable electricity generation poses a sizable hurdle, which is the major reason why scalable energy storage is needed. This intermittency problem can be illustrated with the idea of the “duck curve,” as depicted in Figure 1.2.

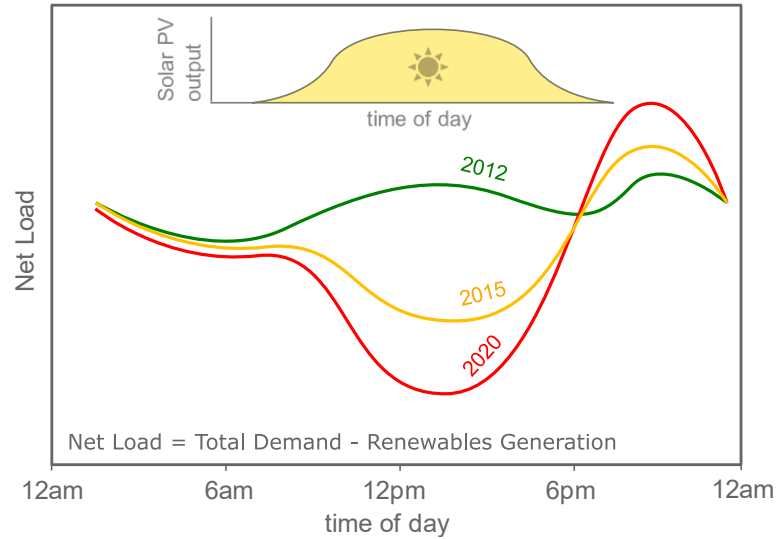


Figure 1.2. Schematic drawing of the “duck curve” as observed in springtime in California. As the deployment of solar PV has increased exponentially over the last decade, the intraday variation in net load on the electrical grid has increased. The inset shows how solar PV generation output varies over the course of a typical day.

While solar PV generation peaks during the day, electricity demand peaks in the evening. As a result, the net electricity load on the grid, minus renewables, dips during the day and rises sharply to peak during the evening hours before declining overnight⁸. Figure 1.2 shows how the variation in net load is increasingly magnified as the percentage of electricity from solar increases over time. The resulting net load curves form the shape of a duck – cute, but quite problematic. Consequently, the large intraday fluctuations in net load can lead to electrical grid instability, necessitating energy storage to smooth out the supply and demand imbalances⁸. Often, solar PV is simply switched off when electricity demand is too low, which means those panels are producing no value at that time. Simply put, if clean energy cannot be stored for when it is needed, there is little reason to produce more of it. Instead of curtailing solar PV, electrolyzers can be switched on, or operated at higher loads, to soak up excess mid-

day electricity and produce inexpensive green hydrogen. Hydrogen can be stored and used in a fuel cell to generate electricity later, or it can be sold as a commodity. Green hydrogen production incentivizes renewables by ensuring electricity is not wasted, thus improving the value proposition of deploying more solar PV and wind turbines.

As a complement to electrical grid load balancing, green hydrogen can be used to decarbonize heavy industries. In essence, hydrogen is a medium that can be used to transform electricity into a more versatile stored chemical energy. Hydrogen can be used to produce ammonia for fertilizer, refine iron ore into steel, produce industrial chemicals, and ship freight by land and sea in a more environmentally sustainable manner^{9, 10}. Cumulatively, these industries make up around 25-30% of total global energy consumption and are notorious CO₂ emitters, see Figure 1.3¹⁰. The Hydrogen Council has estimated that green H₂ can displace fossil fuels to provide 20% of total carbon abatement needed to reach net zero by 2050⁹. Due to various physical constraints, decarbonization of these heavy industries is impractical with clean electricity alone, and hydrogen can provide the necessary bridge to facilitate decarbonization.

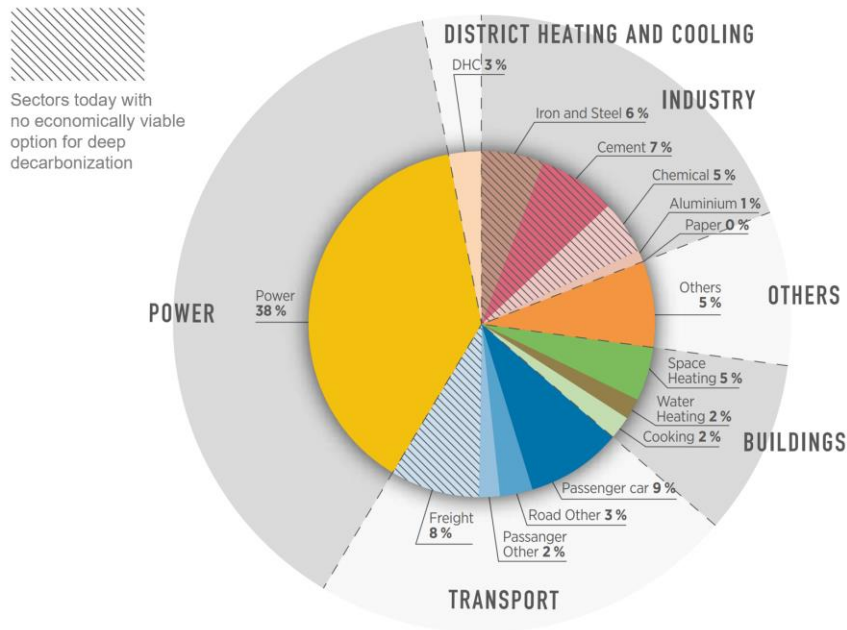


Figure 1.3. Breakdown of global energy-related CO₂ emissions by sector in 2015. Adapted from the IRENA Hydrogen from renewable power: Technology outlook for the energy transition report. Green hydrogen can be used to abate carbon emissions in sectors which have historically had no economically viable option for decarbonization.

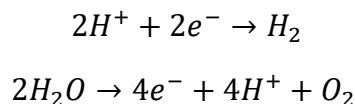
Currently, the cost to produce green hydrogen is \$4-6/kg¹¹. To become competitive with fossil-fuel derived hydrogen, the price of green hydrogen must decrease to below \$1.5/kg¹¹. Approximately 60% of the cost to produce green hydrogen today comes from electricity costs, i.e. operating costs⁵. Given the exponential growth and Wright’s law scaling of wind and solar PV, the cost of clean electricity will continue to drop as deployment accelerates, perhaps 40-60% over the next decade⁵. The cost of green hydrogen will naturally follow the declines in clean electricity costs that accompany the growth of renewables.

In addition to electricity costs, electrolyzers have a significant upfront cost that factors into the price of green hydrogen. As noted earlier, hydrogen electrolyzers also

follow Wright's power law scaling. Electrolyzer capital costs are forecasted to decrease 80-95% over the next two decades as production grows exponentially, assuming an observed learning rate of ~15%⁵. This ongoing trend is similar to the observed exponential growth of solar PV and consequent cost declines of 95% from 2000 to 2020⁵. Reducing the price of green H₂ to below \$1.5/kg is projected to happen soon and possibly before 2030. However, the cumulative global deployed capacity of wind (>800GW) and solar PV production (>900GW) are much farther along than H₂ electrolyzers (~1GW in 2022)⁵. If electrolyzer costs can be reduced faster, then adoption will accelerate rapidly, hopefully keeping pace with renewables growth. Consequently, by reducing the likelihood of creating energy storage bottlenecks during the renewable transition, meeting CO₂ reduction targets could be achieved sooner. In addition to the benefits of economies of scale, technological advancements can help accelerate electrolyzer cost declines. Developing inexpensive fuel cells and electrolyzers is a major motivator for the present work.

1.2 Practical Hydrogen Electrocatalysis and Hydroxide Exchange Membrane Fuel Cells & Electrolyzers

In the previous section, we introduced the basic chemistry of hydrogen electrolyzers and fuel cells without discussing the practical matter of how these reactions are harnessed in a device. This section will explore how these reactions can be harnessed in a cost-effective way. The familiar and simplest physical configuration of an electrochemical cell is two electrodes immersed in an electrolyte and connected by an external circuit. In acidic hydrogen electrolysis, hydrogen is produced at the cathode by the hydrogen evolution reaction (HER), and oxygen is produced at the anode by the oxygen evolution reaction (OER):



The protons produced from OER must diffuse through the electrolyte from the anode to the cathode where they are reduced. After reduction, H atoms bonded to the surface combine to produce hydrogen gas. In hydrogen fuel cells where electricity is produced from H_2 , the half-cell reactions proceed in the reverse direction, commonly referred to as the hydrogen oxidation reaction (HOR) and oxygen reduction reaction (ORR). By judicious design of device materials and physical configuration, the performance and cost of fuel cells and electrolyzers can be adjusted to meet various desirable criteria. However, a challenging design problem exists. For fuel cells and electrolyzers to be economical, these devices need to be durable, energy efficient, reasonably compact, and produced from inexpensive materials.

To meet these design criteria, it is advantageous to separate the electrodes with an ion-conducting polymer electrolyte rather than immersing the electrodes in liquid electrolyte. In practice, this is achieved by producing a thin sheet of polymer and

casting a layer of anode and cathode electrode materials on either side of the polymer to create a membrane-electrode assembly (MEA)¹². When the polymer backbone contains certain negatively charged functional groups, the membranes conduct protons from one electrode to the other. These devices are referred to as proton exchange membrane electrolyzers (PEMEL) and proton exchange membrane fuel cells (PEMFC).

Using polymer electrolytes rather than liquid electrolytes improves efficiency and shrinks the physical footprint of the devices. The short conduction path for ions through the thin membrane reduces the energy losses due to resistance and improves overall cell efficiency. Because the MEAs form a thin sheet, compact devices can be produced— compactness is important for transportation applications. Because of the benefits of the MEA configuration, PEMFCs and PEMELs have become increasingly popular in recent years. Today, several private companies are building factories which are designed for PEMEL and PEMFC production volumes amounting to >1GW rated capacity per year^{13, 14}. However, within the ion-exchange membrane device scheme, additional optimizations are possible to further improve device cost and performance.

Performing hydrogen electrocatalysis in an alkaline environment is a particularly promising route to reduce upfront costs for MEA-based fuel cells and electrolyzers. When the backbone of the ion-conducting polymer is engineered to contain certain positively charged functional groups, the membrane conducts hydroxide ions from one electrode to the other. Devices that use MEAs with hydroxide-conducting membranes are referred to as hydroxide exchange membrane fuel cells (HEMFC) and hydroxide exchange membrane electrolyzers (HEMEL). The layout and chemistry of PEMFCs/PEMELs is compared to HEMFCs/HEMELs in

Figure 1.4. The use of the alkaline medium permits the use of less expensive materials. For example, less expensive metals can be used for the bipolar plates, and non-precious metals can be used for the electrode catalysts¹⁵. Developing durable, efficient, and cost-effective HEMFCs and HEMELs is an active area of research, and a few major challenges must be addressed before commercialization of inexpensive HEMFCs and HEMELs is possible^{15, 16}. If low-cost HEMELs can be commercialized at scale, then producing green H₂ should become less expensive, leading to greater adoption.

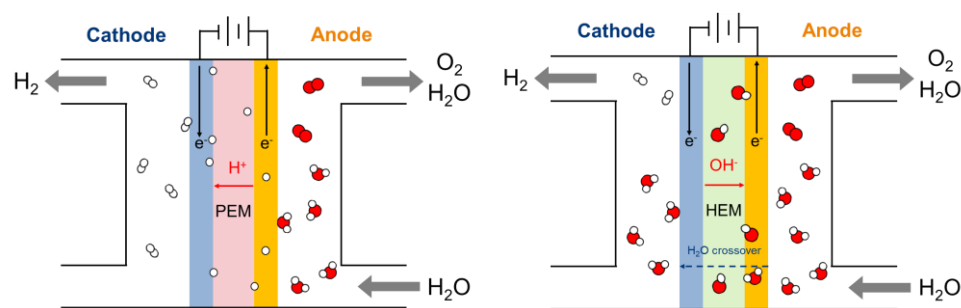


Figure 1.4. PEMEL vs. HEMEL chemistry and device configuration. On the left, a PEM device is shown. In a PEMEL, water is split at the anode and H^+ migrates across the proton-conducting membrane (pink) from the anode to the cathode to form H_2 . On the right, in a HEM device, water is split at the cathode and OH^- ions migrate across the hydroxide-conducting membrane (light green) from the cathode to the anode. In both cases, the anode and cathode are cast on either side of the membrane and form the MEA. Figure created by Alexandra Oliveira.

In this work, we will focus on understanding one hindrance to HEMFC and HEMEL commercialization: the HOR and HER reactions are much slower in alkaline than in acid on typical catalysts, shown in Figure 1.5¹⁷. Sluggish alkaline catalyst activity is undesirable and necessitates higher overpotentials to achieve the same current performance as PEM devices. Higher cell overpotential reduces cell efficiency and therefore makes HEMFC/HEMEL economically less favorable.

The mechanism(s) underlying pH-dependent HOR/HER activity has been a long-standing puzzle in the field of electrocatalysis. Clearly identifying the underlying cause(s) of HOR/HER pH-dependent kinetics is expected to improve strategies for device design. If researchers can definitively identify why the alkaline kinetics are slow, then a workaround can be engineered. Moreover, because HOR and HER are such fundamental electrochemical reactions, explaining why the reaction kinetics are slower in base is important to the development of electrochemistry theory.

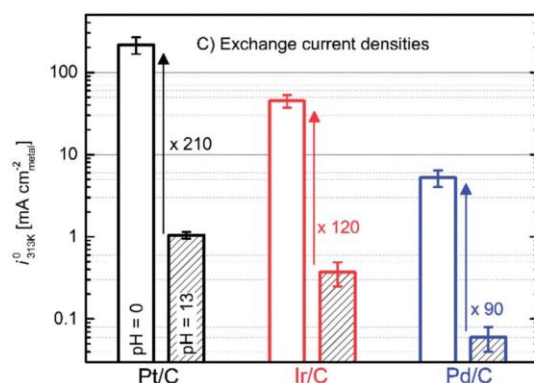


Figure 1.5. pH-dependent catalyst activity change on typical HOR/HER catalysts materials. Reproduced from Durst et al¹⁷. The exchange current density, a measure of catalyst activity, decreases by about two orders of magnitude in pH 13 vs. pH 0 on typical catalysts. Pt/C, Ir/C, and Pd/C are platinum, iridium, and palladium catalysts cast on carbon supports.

1.3 A Primer on the Electrochemical Interface

So far, the fuel cell and electrolyzer reactions have been discussed broadly. To better understand the present work, the fundamental physics involved in electrocatalysis reactions will be briefly summarized. In electrocatalysis, redox ions diffuse between the electrolyte solution and the electrode and undergo reactions near the surface. The electrodes act as a catalyst to facilitate redox reactions by electrode-ion quantum-mechanical interactions. This region where redox occurs is called the electrochemical interface, which is formed by contact between the catalyst electrodes and the electrolyte, on the order of 1 nm thickness. The interfacial region is neither exactly like the metal phase nor the electrolyte phase; it has unique properties due to the inter- and intramolecular interactions between the electrolyte atoms and the electrode atoms. Figure 1.6 depicts a representative electrochemical interface between water and platinum and shows how the solvent forms a “structure” near the surface that is unlike the bulk solvent. In general, the physical properties of the electrolyte at and near the surface significantly affect how quickly electrochemical reactions occur. The intermolecular interactions between ions and the electrolyte may help or hinder reduction and oxidation reactions.

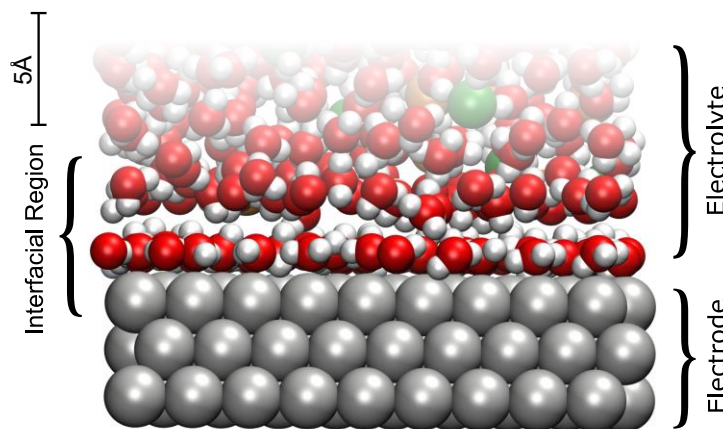


Figure 1.6. Atomistic representation of the electrochemical interface between a platinum (111) electrode surface and an aqueous electrolyte containing NaCl. At the surface, the water molecules form a more planar structured hydrogen bonding network compared to electrolyte in the bulk solution. Water molecules are shown in red and white and NaCl atoms are shown in green and orange, respectively.

The energetics of electrolyte-electrolyte and electrolyte-metal intermolecular interactions depend on the charge, location, concentration, and size of other atoms in the surrounding medium. Additionally, because a voltage is applied, the electrode may bear some excess charge on its surface, which repels/attracts ions of like/unlike charge. Electrode surface charge can also influence the motion and intermolecular structure of nearby polar solvent molecules which, in turn, affect the interaction energies between ionic species and the solvent, modifying redox kinetics.

Marcus Theory is a landmark development in theoretical electrochemistry which describes how the interactions between the electrolyte and redox ions govern the reaction rate of redox kinetics¹⁸⁻²⁰. Here, we consider the regime of non-adiabatic and radiationless electron transfer. For electron transfer between two ions in solution, we recognize that both ions have two available states relevant to the redox process – the reduced and oxidized states. In the electron transfer, one ion is the electron donor

and the other is the acceptor. The solvent has a preferred arrangement around the redox species in each state. This preferred arrangement, also referred to as the equilibrium solvation structure, is different for each state. Because energy must be conserved, any change in the energy of the two ions during charge transfer must be counterbalanced by an opposing change in the energy of the solvent assuming radiationless charge transfer. Additionally, electron transfer happens very fast relative to the slow reorientation of solvent molecules. Therefore, we can approximate the solvent nuclei as fixed in space during electron transfer, as shown in Figure 1.7. In non-adiabatic electron transfer, because energy is conserved and the free energy change due to solvent motion is negligible, electron transfer is most likely when the energy change associated with the change in oxidation state is zero, i.e. the two states are degenerate.

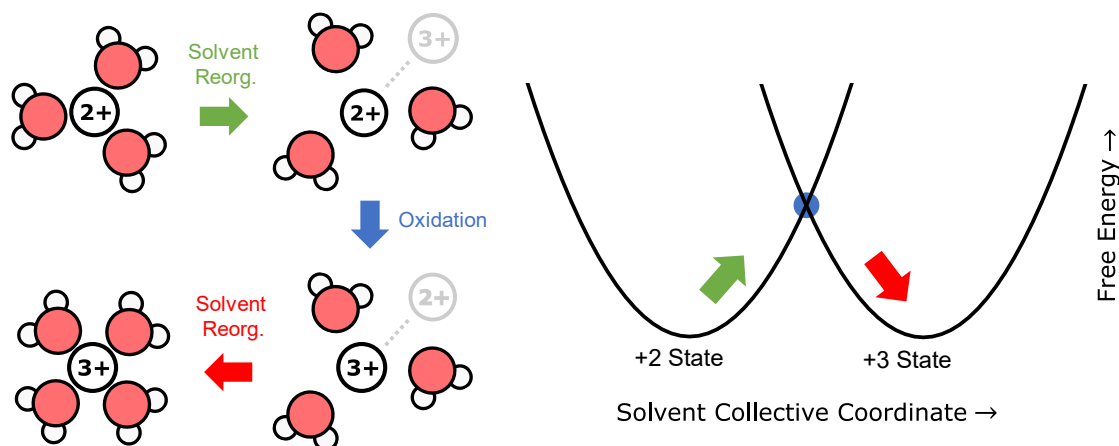


Figure 1.7. Summary sketch of the process of solvent reorganization and non-adiabatic electron transfer. Non-adiabatic electron transfer can be described as a rapid “jump” from one curve to another without change in nuclear positions, shown on the left. The initial and final states correspond to the reduced and oxidized states at equilibrium solvation. The solvent must reorganize to reach the crossing point (where the energies are equal) of the two free energy curves before redox is likely to occur. After redox, the solvent relaxes to equilibrium solvation for the product states. The central ion is the electron donor to the acceptor ion shown in gray.

The two redox states have different equilibrium solvation structures and energies, shown in Figure 1.7. Therefore, the energy of the solvent must change before redox occurs. To reach the point where the two states are equal in energy, that is, the transition state, the solvent molecules must reorganize around the redox ion by rotation and translation. Solvent reorganization is a function of the interaction energy between all the nearby electrolyte molecules and the redox ion, illustrated in Figure 1.7. The progress of this reorganization can be tracked by a single collective variable, called the solvent coordinate, which tracks the electric polarization of the solvent. In molecular simulations, the solvent coordinate can be calculated from the sum of all interaction energies between the charged redox ion and the polar electrolyte molecules. One key feature of Marcus Theory is that the free energy of the solvent

plus the ion is approximately a parabolic function of the solvent coordinate, that is, how far the solvent is polarized from redox ion equilibrium solvation, shown in Figure 1.7. The activation barrier for the reaction in the non-adiabatic electron transfer regime can be estimated from two variables: the solvent reorganization energy, related to the difference in solvent polarization between the two equilibrium states, and total energy change between the initial reactant state and the product state. Assuming a symmetric double well potential for the two states, the redox activation energy can then be written using the celebrated Marcus theory expression:

$$\Delta G^\ddagger = \frac{(\Delta G + \lambda)^2}{4\lambda}$$

Where ΔG is the Gibbs free energy of reaction and λ is the solvent reorganization energy. Thus, Marcus theory provides a theoretical basis to relate the properties of the solvent fluctuations to redox reaction rate kinetics.

At the electrochemical interface, the presence of the electrode introduces another layer of complexity. Charge transfer between an ion in electrolyte and a solid phase is called heterogeneous electron transfer because the electron is transferred between two different phases. Because the electrode is a macroscopic object, there are many quantum states available to interact with the redox ion's quantum states. When the redox ion moves close to the metal, the electronic states of the ion interact with the metal states, called electronic coupling. The magnitude of electronic coupling typically decays approximately exponentially with respect to the ion's distance from the electrode. When the electronic coupling is large, charge transfer proceeds in the electronically adiabatic regime. Roughly speaking, the strength of the electronic coupling determines how much the redox activation barrier is lowered relative to the non-adiabatic regime. Moreover, the degree to which the redox ion is stabilized by

electronic interactions with the metal determines its adsorption energy. The adsorption energy of reaction intermediates determines the reaction free energy for intermediate reaction steps and therefore greatly affects the overall reaction rate. These factors capture the essence of designing electrochemical catalysts: how can we manipulate the material to tune the electronic interactions between redox ions and the catalyst to make the desired chemical reactions proceed faster?

In the 1960s, Noel Hush developed a foundational theory of adiabatic electron-transfer²¹. When electronic coupling between a donor and acceptor orbital is strong, as is the case in hydrogen electrocatalysis, electron transfer proceeds along a ground-state free energy surface. Unlike the case of non-adiabatic charge transfer, which occurs as rapid “jumps” from one state to another, adiabatic charge transfer proceeds smoothly along a ground-state free energy surface as a function of changing nuclear coordinates. Specifically, charge transfer, i.e. the expectation value of redox orbital occupancy, is a continuous function of the solvent polarization around the redox ion. In adiabatic charge transfer, the electronic coupling induces an avoided crossing at the point where the free energies of the equivalent pure states would cross. Consequently, strong coupling in the adiabatic case lowers the transition state energy relative to the equivalent non-adiabatic, weak-coupling case, illustrated in Figure 1.8.

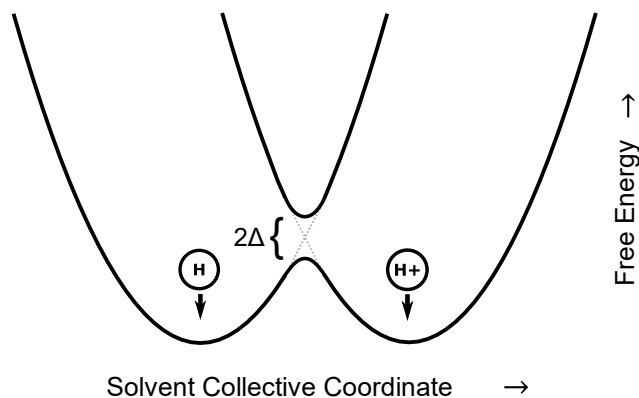


Figure 1.8. Summary sketch of adiabatic electron transfer for H/H⁺ redox. When there is strong donor-acceptor electronic coupling, electron transfer proceeds along a ground state free energy surface. The equivalent weak-coupling free energies are traced with the dotted lines. The relationship between the electronic coupling magnitude, Δ , and the activation barrier height in adiabatic electron transfer is shown. Strong coupling between hydrogen and the electrode electronic states is the essence of what enables catalysis in hydrogen fuel cells and electrolyzers.

To summarize, the rate of chemical reactions in electrocatalysis, and in this case hydrogen electrocatalysis, is governed by both the solvent reorganization energy and favorability of the ion-catalyst electronic interactions.

Here, an example of the interplay between interfacial solvent structure and electronic effects is instructive. Recalling Figure 1.6, water molecules can form an ordered hydrogen-bonding network on surfaces like platinum. Large ions like Fe³⁺ are strongly solvated and resist desolvation, i.e. solvent reorganization. Fe³⁺ does not approach very close to the electrode because the ordered solvent at the surface does not easily reorient to accommodate the preferred solvation structure of the ion. Since the ion is not chemisorbed, Fe³⁺ can only weakly couple electronically to the catalyst. Consequently, redox kinetics are slow²².

1.4 Recent Progress in pH-dependent HOR/HER Kinetics and Hydrogen Electrocatalysis Simulation

1.4.1 Thermodynamic Descriptors & Hydrogen Binding Energy

One of the dominant design principles for improving the activity of electrocatalysts is tuning thermodynamic descriptors such as the adsorbate binding energy of reaction intermediates. The assumption of this approach is that thermodynamic descriptors linearly correlate with the reaction activation barriers, called Bronsted-Evans-Polanyi (BEP) relationships²³. In the same vein, the Sabatier principle states the adsorption energy of some adsorbate on a catalyst should neither be too strong nor too weak to maximize reaction rate of both the adsorption and desorption steps of a reaction. For example, in HER, when the proton is reduced to neutral H in the Volmer step, it adsorbs and forms a bond with the catalyst surface. Adsorbed H (H^*) then combines with another H^* to form H_2 . If the energy of binding H to the surface is too weak, then reducing the proton to surface H^* is less favorable. If the bond between H and the surface is too strong, then H will tend to stay on the surface and inhibit the formation of H_2 . Therefore, an optimal binding energy of hydrogen is required to make both steps in the overall reaction proceed quickly, resulting in a “volcano” shaped relationship between activity and binding energy, shown in Figure 1.9^{24,25}. The hydrogen binding energy is determined by its electronic interactions with the catalyst and can be tuned by choice of the catalyst material²⁶.

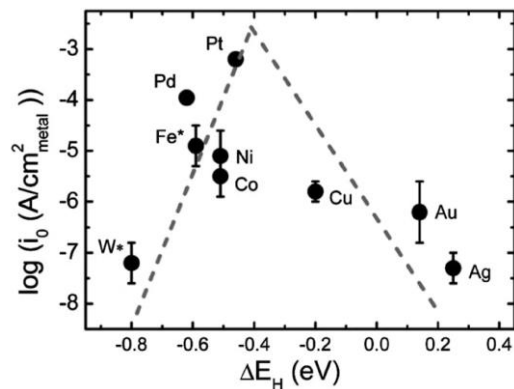


Figure 1.9. Volcano plot of experimental HOR/HER activity on various monometallic catalysts versus catalyst hydrogen binding energy computed from DFT. Reproduced with permission from Sheng et al²⁵. On the left branch, the hydrogen binding energy is too strong, and on the right branch, hydrogen binding is too weak.

The Yan group proposed that hydrogen binding energy (HBE) in the presence of electrolyte can be estimated by measuring the electrode potential at which hydrogen adsorbs or desorbs, i.e. by the potential where peak current for adsorption/desorption occurs, E_{peak} ²⁴. As pH increases, hydrogen desorbs at higher potentials on typical platinum-group catalysts, implying a stronger HBE which should result in sluggish alkaline kinetics. Sheng et al. and the Yan group later proposed that the positive correlation between HBE and pH is due to a weakening of water binding energy, which competes with hydrogen for surface sites^{27, 28}. Thus, the measured HBE is an *apparent* value which reflects the total free energy of hydrogen adsorption in the presence of the electrolyte. Density functional theory molecular dynamics (DFTMD) simulations by Cheng et al. supported the apparent HBE theory by showing that water binding weakens and HBE strengthens on Pt (100) at conditions corresponding to alkaline HOR and HER²⁹.

However, recent evidence indicates that the apparent HBE theory is incomplete as a predictor of pH-dependent kinetics. The reaction rates of all tested metals decrease by up to 2 orders of magnitude going from acid to base^{30, 31}. Even metals with a weak HBE show decreased activity at high pH where HBE is expected to strengthen, which is inconsistent with the BEP/Sabatier principle. These results suggest there is another pH-dependent determinant of HOR/HER kinetics.

Additionally, the Janik and Koper groups argued that E_{peak} is not solely determined by HBE and water adsorption energy, and that the desorption of H^* is accompanied by the replacement with OH^* on stepped sites³²⁻³⁴. In these situations, E_{peak} is also expected to be correlated with hydroxide binding energy, and therefore E_{peak} may not accurately measure the hydrogen binding energy quantity relevant to HOR/HER kinetics. In recent years, several theories have been put forth to explain sluggish alkaline kinetics beyond the HBE approach.

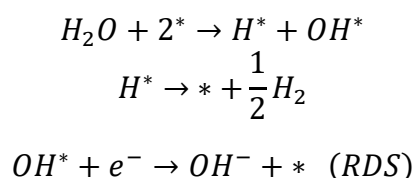
1.4.2 Hydroxide Binding Energy

Hydroxide binding energy (OHBE) has also been proposed as a descriptor for alkaline HOR and HER. Several authors have argued that alkaline HER is rate limited by water splitting at the interface since there is very little free H^+ available as a proton source³⁵⁻⁴⁰. Markovic et al. proposed that alkaline HER kinetics may be tailored by tuning both HBE as well as the energy required to dissociate water, with the following RDS³⁵:



In this mechanistic picture, tuning surface oxophilicity promotes the dissociation of water at the surface by stabilization of OH^* . For example, the addition of oxophillic surface species such as $Ni(OH)_2$ accelerate water splitting on catalysts which have

favorable HBE but, by themselves, have weak OHBE. By studying decorated step sites on Pt through a combination of DFT simulations and experiments, McCrum et al. clarified how OHBE affects the activation energy in the HOR/HER bifunctional mechanism⁴⁰. Even when OHBE is weak and OH* is not a direct product of HER, stabilization of surface hydroxide by the catalyst at the HER transition state accelerates water splitting. When OHBE is strong and OH* is a stable intermediate, water splitting is fast, so HER is rate-limited by OH* desorption:



Thus, McCrum proposed a Sabatier relationship for HOR/HER which is a function of both HBE and OHBE:

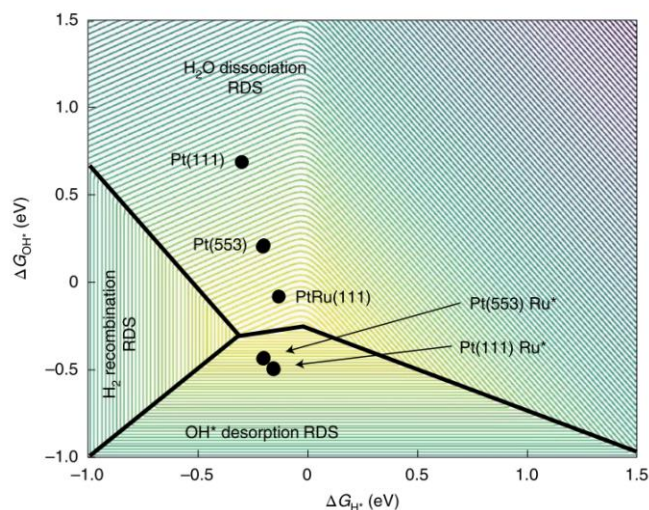


Figure 1.10. 3D HER activity volcano plot with OHBE and HBE as kinetic descriptors. Reproduced with permission from McCrum et al⁴⁰. In this model, both HBE and OHBE must be neither too strong nor too weak for fast alkaline HER kinetics.

However, even with both OHBE and HBE as descriptors for alkaline hydrogen electrocatalysis kinetics, there are still several outstanding puzzles related to kinetic trends in hydrogen electrocatalysis. Since water hydrogens are more strongly bound to the central O atom in H_2O molecules as compared to free protons in acid, i.e. H_3O^+ , it has been argued that breaking the O-H bond in alkaline water splitting is a slow process that explains the pH-dependence of alkaline HER kinetics^{39, 41}. However, hydroxide adsorption sourced from water molecules on stepped Pt as well as Pt (111) has been shown to be extremely fast in both acid and base, which implies that alkaline water splitting is fast at *both* low and high pH^{42, 43}. If alkaline water splitting is fast, why must OHBE be optimized in alkaline to facilitate water splitting and fast HER kinetics? To resolve contradictions such as these, we must understand how the physical properties of the electrochemical interface affect the HOR/HER barriers at an atomistic level, beyond descriptor-based approaches³¹.

1.4.3 Beyond Thermodynamic Descriptors: Electrochemical Interface Effects

Given the shortcomings of thermodynamic descriptor-based approaches, there has been increasing interest in understanding the structure and dynamics of the interfacial electrolyte and its interrelationship with redox kinetics³¹. While HBE and OHBE are convenient targets for catalyst design, these descriptors do not capture all the underlying physical factors that determine electrocatalysis kinetics. As introduced in Section 1.3, the solvent reorganization energy for redox ions in the interfacial region is a key determinant of electrocatalysis kinetics. Moreover, because the electrode may be charged, the electrostatic potential near the surface exhibits spatial variation that influences how easily reactants and supporting electrolyte ions can access the surface, further affecting redox kinetic rates⁴⁴. The mechanism of kinetic

trends related these electrochemical double layer (EDL) effects are less well-understood in hydrogen electrocatalysis compared to thermodynamic descriptors. Additional research is needed to understand the interplay between ion-adsorbate electronic interactions, solvent reorganization, and other non-covalent EDL effects⁴⁵.

Recently, researchers have proposed theories which relate changes in solvent reorganization to hydrogen electrocatalysis kinetic trends. Ledezma-Yanez et al. claimed the decrease in the interfacial electric field strength is responsible for the 5-9x improvement in HER activity when Ni(OH)₂ is added to the surface of Pt catalysts⁴⁶,⁴⁷. The authors argued that interfacial water is less mobile when interfacial field is strong due to polarization effects⁴⁶. Rigid water structure was proposed to make solvent reorganization more difficult for ions moving through the double layer, thereby slowing HER kinetics. However, it is unclear whether surface Ni(OH)₂ modulates activity via field effects or by strengthening OHBE^{31, 35}.

Huang et al. recently proposed that alkali cation-dependent HOR/HER kinetics are governed by trends in solvent reorganization energy⁴⁸. It has been well-established that the presence of large alkali cations like Cs⁺ at the interface result in sluggish HOR/HER kinetics compared to when smaller cations like Li⁺ are present. Large cations like Cs⁺ and Rb⁺ were shown to disrupt interfacial water hydrogen bonding, whereas Li⁺ was shown to promote interfacial hydrogen bonding⁴⁸. Weakened hydrogen bonding in the presence of large cations appears to correlate with an increased interfacial dielectric constant. Additionally, in the Born continuum model of reorganization energy, a higher dielectric constant implies a larger solvent reorganization energy and slower redox kinetics. Thus, Huang et al. concluded that larger cations slow redox kinetics by modulation of interfacial hydrogen bonding.

However, changes in solvent reorganization energy were inferred from current density data rather than direct measurements of solvent polarization at the interface. Current density may be impacted by factors other than solvent reorganization such as the energy associated with ion migration through the EDL. Thus, fitting solvent reorganization energy to experimental current density does not conclusively rule out other factors. While the argument is intuitive, the notion of cation-dependent reorganization energy needs to be tested by further research.

1.4.4 Prospects for Insights from Theory

Given that solvent reorganization, interfacial electric fields, and supporting electrolyte ions can influence heterogeneous ET kinetics, developing methods to study the atomic-scale behavior of electrode-electrolyte interactions is necessary to improve our theoretical understanding of heterogeneous ET. However, experimentally probing electrolyte structure and dynamics in the electrochemical double layer is notoriously challenging, especially under in situ and in operando conditions⁴⁹. Major advances in theory and high-performance computing have enabled simulation techniques to provide mechanistic insights into electrocatalysis. For example, DFTMD has been utilized to understand phenomena including trends in aqueous-phase HBE, the fractional charge of protons in the double layer, and the molecular origin of trends in Helmholtz capacitance, to name a few⁵⁰⁻⁵². However, one downside of DFT based approaches is that sampling solvent fluctuations at timescales relevant to solvent reorganization is currently computationally intractable⁵³. Moreover, simulating the constant-voltage electrode in DFT-based simulations of the electrochemical interface is challenging from both a theoretical and numerical calculation point of view, and this task is the subject of ongoing work⁵³⁻⁵⁶.

To address some of these limitations, theoretical mathematical models and have been successfully employed to study adiabatic electron transfer in electrocatalysis. Santos and Schmickler developed a hydrogen electrocatalysis model that incorporates hydrogen-metal electronic coupling as well as solvent reorganization⁵⁷. The Santos and Schmickler model was a major development and helped to link catalyst electronic structure to HOR/HER catalyst activity with solvent reorganization included. Later, the Hammes-Schiffer group developed proton-coupled electron transfer models based on empirical valence bond theory which incorporate both solvent reorganization and interfacial electric fields in the calculation of electron transfer free energy surfaces, further refining the understanding of the complex interplay between electronic coupling, solvent reorganization, and interfacial electrostatics^{58, 59}.

However, within these theoretical modeling approaches, interfacial electrostatics are treated using mean-field approximations and do not account for the strong electrostatic potential heterogeneity in the double layer^{60, 61}. Moreover, without atomistic simulation of the EDL, theoretical models of hydrogen electrocatalysis have so far not captured the large spatial and temporal heterogeneities of the electrolyte in the electrochemical interface⁶²⁻⁶⁴. In other words, the interfacial solvent is highly structured in a way that depends on how molecules physically arrange near the surface. The heterogeneity of both the electrolyte species and the electric potential in the interfacial region are expected to significantly affect electrocatalysis kinetics. While theoretical approaches are undoubtedly instrumental for understanding electrocatalysis, progress in atomistic simulation techniques is also needed to drive new mechanistic insights into EDL effects. A more detailed review of electron transfer models will be explored in Chapter 2.

1.5 Dissertation Overview

The objective of this work is two-fold. First, we set out to develop a computational method to study the EDL effects in hydrogen electrocatalysis using molecular dynamics. Second, we employ our model to investigate EDL effects relevant to pH-dependent HOR and HER kinetics. Specifically, we investigate the mechanism by which interfacial electrostatic potential and supporting electrolyte effects alter the Volmer step activation barrier. In this work, we use an embedded Anderson-Newns Hamiltonian molecular dynamics approach to sample redox events for HOR and HER. Moreover, we examine how the Volmer step free energies are connected to atomistic changes in EDL structure and dynamics. This dissertation is organized into five chapters, and the remaining chapters are outlined below.

Chapter 2: Methodological development. Here, we develop an embedded Anderson-Newns Hamiltonian (ANH) molecular dynamics approach to sample the electronically adiabatic Volmer step in HOR and HER. With this technique, we can simulate redox events for an explicit hydrogen atom at the electrochemical interface. This approach is advantageous because it can be used to calculate solvent reorganization energies for redox events while also providing an all-atom explicit EDL. Here, we make controllable electrode potential compatible with the embedded ANH approach for the first time. With this method, we are able to investigate how redox kinetics and solvent reorganization energy are affected by changes in electrode potential and surface charge.

Chapter 3: Surface charge and solvent reorganization. We employ the embedded-ANH molecular dynamics approach to study how surface charge affects Volmer kinetics on Pt (111). Strong negative surface charge has been recently proposed to explain pH-dependent changes in HER kinetics by modulation of solvent reorganization energy. In this chapter, we show that interfacial electric fields near negatively charged electrodes are not strong enough to significantly modulate solvent reorganization energy at relevant potentials. Instead, the negative surface lowers the local electrostatic potential of double layer H^+ and increases the barrier for HER, essentially by decreasing the driving force for H^+ reduction.

Chapter 4: Electrolyte effects on Volmer kinetics. We study the Volmer redox event on Pt (111) in two electrolyte solutions, 1M NaCl and 1M CsCl, to investigate how the choice of cation type affects HOR and HER kinetics. It has been well-established that larger alkali cations like Cs^+ inhibit HOR and HER more so than smaller cations, but the mechanism is not well understood. In recent work, it was proposed that the cation size-dependence on HOR and HER kinetics is mediated by changes in solvent reorganization energy. Larger cations like Cs^+ were proposed to slow kinetics via increased solvent reorganization energy. We show that the redox solvent reorganization is indeed larger very close to the surface in the electrolyte containing Cs^+ compared to the electrolyte containing Na^+ . However, surprisingly, the increase in reorganization energy is not due to the solvent but due to the reorganization of the ions. Moreover, the high interfacial density of solvated Cs^+ ions hinders the approach of H^+ to the surface, reducing the entropy of H^+ and thus increasing the activation energy for the Volmer step.

Chapter 5: Outlook and Future directions. In this section, we briefly summarize the present work and expand on its limitations. We also suggest improvements to modeling approaches for future work. The embedded-ANH molecular dynamics approach is useful to uncover qualitative kinetic trends in electrocatalysis, however, more detailed treatments of ion-metal electronic coupling as well as the spatial distributions of surface charge are necessary to achieve better quantitative accuracy.

In alkaline HOR and HER, OH^- or OH^* likely participates in the Volmer mechanism, which has not been studied here. Given the practical and theoretical importance of understanding pH-dependent HOR/HER kinetics, we suggest that an embedded-ANH OH^* adsorption model would be useful to shed light on EDL effects in strongly alkaline electrolytes. Lastly, we close by suggesting potential methodological improvements upon the present approach.

Chapter 2

EMBEDDED ANDERSON-NEWNS HAMILTONIAN MOLECULAR SIMULATION METHODS AND DEVELOPMENT

2.1 Introduction and Theory

To motivate our choice of model features, we briefly recap key theory developments leading up to the current understanding of hydrogen electrocatalysis. R. A. Marcus formulated a general theory of electron transfer which has much well-established experimental support and broad applicability to a wide range of electron transfer (ET) systems^{18, 20}. In Marcus theory, redox systems display parabolic free energy curves with respect to the solvent polarization, and charge transfer is most likely near the crossing point of the two redox states for non-adiabatic ET¹⁸.

In heterogenous ET systems, there is frequently strong ion-metal coupling resulting in adiabatic ET, that is, charge transfer smoothly proceeds as a function of the relevant nuclear coordinates. In chemisorption, which involves strong adatom-metal coupling, the Anderson-Newns Hamiltonian (ANH) approach clarified the relationship between the electronic structure of catalysts, electronic coupling, and chemisorption energies⁶⁵. Still, a model which incorporates solvent reorganization was needed to study electrocatalysis. Later, Santos and Schmickler developed an ANH-based mathematical model which incorporated linear ion-solvent coupling to model solvent reorganization. By parametrizing the model using DFT, Santos and Schmickler showed how the electronic structure of transition metals affects the free energy surface in hydrogen electrocatalysis⁶⁶. The Anderson-Newns-Schmickler

theory was a significant step in the study of electrocatalysis *beyond* the weak ion-metal coupling regime. However, in the work by Schmickler et al, the EDL was only treated implicitly.

Straus and Voth et al. developed an embedded ANH approach which incorporated an approximate solution to the ANH into classical molecular dynamics. Because Voth et al. studied outer-sphere heterogeneous ET, the ANH was approximated using weak-coupling limit, and thus the electronic ion-catalyst interactions were greatly simplified. The embedded-ANH approach of course incorporates an atomistic representation of EDL effects into adiabatic ET studies. Given the large spatial heterogeneity of electrolyte at the electrochemical interface, atomistic representations of the double layer are a significant improvement over dielectric continuum treatments of the EDL²².

Modeling ion-solvent electronic coupling, solvent reorganization, and electrode potential together is a grand challenge in electrochemistry theory. Theoretical efforts to incorporate all these essential features in a comprehensive electrocatalysis model are ongoing⁶⁷. Recently, Lam and the Hammes-Schiffer group formulated an empirical valence bond theory model to study Volmer proton coupled electron transfer in the electronically adiabatic regime. In the Lam et al. model, solvent interactions are treated under the linear-response approximation, and additionally, an electrode potential and a mean-field electrostatic model of the EDL are included⁵⁹. The inclusion of the interfacial electric field has a significant effect on Volmer free energies. For example, it was shown that after PCET, the conjugate base of the proton donor moves away from the surface due repulsion from a negatively

charged electrode. These significant works are still only a small sampling of a wide body of theoretical efforts which have been reviewed in more detail elsewhere⁶⁷.

In this work, our focus is to model how the structure and dynamics of the EDL affect Volmer kinetics. One important feature of the hydrogen electrocatalysis models by Schmickler et al. and Hammes-Schiffer et al. is that the effects of surface electrostatic potential are either not included explicitly or reduced to mean-field approximations^{58, 66}. In this work, we take a different approach and extend Voth's embedded ANH molecular dynamics model to simulate the Volmer step, treating the solvent degrees of freedom classically with molecular dynamics²². We additionally incorporate conducting interface boundary conditions which enable control over the cell voltage in a capacitor cell configuration, and we define the vertical excitation coordinate appropriately in the presence of polarized metal atoms⁶⁰. This approach is complementary to other works which treat the strong metal-ion electronic coupling in more detail^{57, 58}. Here, we treat metal-ion coupling in a simplified way, choosing instead to focus on double layer effects, which are less well understood in the context of the Volmer step. With this model, we do not assume the linear response approximation for the solvent a-priori and we do not assume mean-field electrostatics for the interfacial fields, both of which are drastic approximations in the EDL.

2.2 Electronic Hamiltonian details.

The electronic Hamiltonian term is added to the molecular dynamics Hamiltonian to describe the electronically adiabatic charge transfer:

$$\mathcal{H} = \mathcal{H}_{sol} + \mathcal{H}_{el}$$

Initially, the electronic Hamiltonian term \mathcal{H}_{el} can be written in the second quantized formalism as follows:

$$\mathcal{H}_{el} = (\epsilon_a + \Delta E)n_a + \sum_k (\epsilon_k n_k + \mathcal{V}_{ak} c_a^\dagger c_k + \mathcal{V}_{ka} c_k^\dagger c_a)$$

Where ϵ_a is the vacuum energy level of the hydrogen orbital $|a\rangle$. We assume there is a single H orbital state that interacts with the continuum of states on the metal. This single hydrogen orbital has occupancy n_a which has values 0 or 1. ΔE is the vertical energy gap collective coordinate, defined as the potential energy difference between the reduced and oxidized states at fixed nuclear coordinates. The summation over the k electronic states includes contributions from occupied metal states as well as ion-metal interaction terms representing the charge transfer between the ion orbital to the metal states. V_{ak} are the electronic resonance integrals between $|a\rangle$ and $|k\rangle$, and $c_a^\dagger, c_a, c_k^\dagger, c_k$ are the electron creation and annihilation operators for the respective states.

To embed the electronic term into molecular dynamics, an analytic form for \mathcal{H}_{el} is needed. Thus, we must make simplifying assumptions about the electronic interaction between the hydrogen state and the metal states. We make the adiabatic assumption of separability between the solvent and electronic degrees of freedom. It has been shown that the electronic Hamiltonian can be simplified to yield the following analytic form when we consider a single redox ion state with broadband coupling to the metal:

$$E_0(\Delta E) = \frac{1}{2} \Delta E + \frac{1}{\pi} (\epsilon_a + \Delta E - \epsilon_f) \tan^{-1} \left[\frac{\epsilon_f - (\epsilon_a + \Delta E)}{\Delta} \right] + \frac{\Delta}{2\pi} \ln \left[(\epsilon_a + \Delta E - \epsilon_f)^2 + \Delta^2 \right]$$

Where ϵ_f is the Fermi level of the metal and Δ is the energy broadening which lowers the transition state energy and enables electrocatalysis. The level-broadening parameter Δ is the coupling between the hydrogen state and the k metal states and is formally given by:

$$\Delta(\epsilon) = \pi \sum_k |V_{ak}|^2 \delta(\epsilon - \epsilon_k)$$

With the broadband coupling assumption, Δ becomes independent of energy. Since the magnitude of coupling decreases approximately exponentially as the redox atom moves away from the surface, we make the first order approximation for Δ :

$$\Delta = \Delta_0 \exp(-\beta z)$$

Where β is the rate of decay of the coupling as the ion moves away from the surface. Parametrization of the coupling is approximated by calculating the H orbital DOS at various z -distances from the surface using DFT. We have chosen $\beta = 1.1 \text{\AA}^{-1}$ and $\Delta = 16 \text{eV}$ for this work.

Briefly, we can summarize the behavior of the electronic Hamiltonian. In the adiabatic simulations, the H orbital occupancy is a continuous function of the electronic coupling, Δ , and the fluctuating vertical energy gap, ΔE . In the MD simulation, ΔE and Δ are computed at each timestep and used to calculate the electronic energies in E_0 and the corresponding electronic forces. In the limit of $\langle n_a \rangle = 0$, the interaction potentials between the redox hydrogen and the solvent are that of H^+ . In the limit of $\langle n_a \rangle = 1$, the interaction potentials between the redox hydrogen and the solvent are that of reduced hydrogen. Moreover, in the reduced state, we add an additional Morse bond term to bond H^* to the Pt surface.

2.3 Constant potential method.

To model the electrified interface, we incorporate a method of enforcing controllable constant-potential boundary conditions in molecular dynamics. We adopt the protocol from Voth et al. which is based on the classical electrostatics method of images. Voth et al. utilize two sets of explicit primary image charges in a capacitor-cell configuration⁶⁰. The conducting image planes are chosen as the center of the exposed layer of metal atoms on each electrode. The nonuniform portion of surface charge distribution is modeled by the primary image charges. The excess free charge Q_0 necessary to set a voltage ΔV_0 in a cell containing electrolyte is the same as for an equivalent empty capacitor:

$$\Delta V_0 = \frac{Q_0}{\epsilon_\alpha A} D$$

Where D is the cell gap width and A is the surface area. The higher-order images and excess charge are distributed evenly across the surface through an efficient method as follows:

$$q_{LE} = \sum_{i=1}^n \frac{q_{R_i} z_{R_i}}{D} + Q_0$$
$$q_{RE} = \sum_{i=1}^n q_{R_i} \left(1 - \frac{z_{R_i}}{D}\right) - Q_0$$

Where q_{R_i} and z_{R_i} are the real electrolyte charges and z positions in the cell, respectively. q_{LE} is the charge on the left electrode and q_{RE} is for the right electrode. At each timestep, the primary image charges and uniform charges are updated. As redox occurs in adiabatic ET, the ion's primary images as well as the uniform charges are similarly updated to reflect the changing charge state of the ion due to the ANH.

2.4 Vertical energy gap and interaction potentials.

Next, we define the vertical gap energy coordinate which tracks solvent reorganization. As previous work by Sprik has shown, it is convenient to adopt the diabatic vertical energy gap ΔE between the reduced and oxidized diabatic states as the collective coordinate. The vertical energy gap is defined as the potential energy required to change a particle from the oxidized to reduced state, keeping all nuclear coordinates \mathbf{R} fixed:

$$\Delta E(\mathbf{R}) = V^{red}(\mathbf{R}) - V^{ox}(\mathbf{R})$$

First, it is instructive to write out the interaction potential terms which describe the interaction between the hydrogen ion (and its images) with the rest of the system. The Coulombic terms are as follows:

$$\begin{aligned} \mathcal{V}_{coulombic} = & (z - n_a)(\mathcal{V}_{elyte-ion} - \mathcal{V}_{elyte-ion images} - \mathcal{V}_{elyte images-ion} \\ & + (z - n_a)\mathcal{V}_{ion-ion images} + \mathcal{V}_{\sigma-ion}) + \mathcal{V}_{\sigma-water} \end{aligned}$$

Where $\mathcal{V}_{elyte-ion}$ is the Coulomb interaction between the ion and the rest of the electrolyte (excluding the ion itself), $\mathcal{V}_{elyte-ion image}$ is between the electrolyte and the ion images, $\mathcal{V}_{elyte images-ion}$ is between the electrolyte images and the ion, $\mathcal{V}_{ion-ion images}$ is between the ion and its own images, $\mathcal{V}_{\sigma-ion}$ is between the ion and the uniform electrode charges q_{LE} and q_{RE} , and $\mathcal{V}_{\sigma-water}$ is between the electrolyte and the uniform electrode charges. z is the charge of the ion, +1 for the proton.

When defining ΔE , it is often assumed that nonpolar interaction potentials are the same in the reduced and oxidized state of an ion. However, hydrogen is a special case because the solvated proton coordinates strongly with water, whereas reduced H-water interactions are repulsive. Therefore, we have fit simple functional forms to approximate the non-Coulombic contribution to hydrogen-water interactions for the

reduced and oxidized states. We add additional terms to the overall potential for the two redox states:

$$\mathcal{V}_{elyte-ion np} = n_a \mathcal{V}_{elyte-ion np}^H + (1 - n_a) \mathcal{V}_{elyte-ion np}^{H^+}$$

$\mathcal{V}_{elyte-ion np}^H$ are the nonpolar interactions between reduced H and the electrolyte, and $\mathcal{V}_{elyte-ion np}^{H^+}$ are the nonpolar interactions between the proton and the electrolyte.

$$\begin{aligned} \mathcal{V}_{elyte-ion np}^H &= \sum_i^{n_o} A_O^H \exp(-B_{OH} r_i) + \sum_j^{n_H} A_H^H \exp(-B_{HH} r_j) \\ \mathcal{V}_{elyte-ion np}^{H^+} &= \sum_i^{n_o} \left(D_O^{H^+} \left(1 - \exp(-\alpha_O^{H^+} (r_i - r_0)) \right) \right)^2 - D_O^{H^+} \\ &\quad + \sum_j^{n_H} A_H^{H^+} \exp(-B_H^{H^+} r_j) \end{aligned}$$

Where i runs over all water oxygen atoms and j over all water hydrogens. We have parametrized the interaction potentials based on Gaussian calculations of small clusters of water solvating a single proton at the B3LYP/aug-cc-pvdz theory level. With our potential, solvating the proton in a cluster of two waters produces a Zundel-like ion with oxygen-proton bond length of 1.22 Å, matching well with the ab-initio calculated distance⁶⁸. The solvation enthalpy of the proton in a cluster of 128 TIP3P waters was calculated to be -10.7eV using our force field, reasonably close to ab-initio estimates for the bulk solvation enthalpy of -11.4eV to -11.9eV⁶⁸.

Additionally, there is a chemical bond contribution between hydrogen and the catalyst surface. Assuming a broadband coupling in our model does not sufficiently capture the chemisorption of H in the model; the Hilbert transform of Δ gives the level shift of the hydrogen DOS, Λ , sometimes called the chemisorption function. Λ becomes zero when Δ is constant, and consequently hydrogen is not stabilized as it

approaches the surface. To correct for the simplified coupling and make reduced H adsorb on the surface, we have added an additional platinum-hydrogen Morse bond term, fitted from DFT calculations in VASP. In the DFT calculations, the energies of hydrogen were calculated at several distances above a Pt (111) atop site for a relaxed 3x3x4 slab. We used the PBE functional, 7x7x1 Γ -centered kpoint mesh, 1st order Methfessel-Paxton smearing with width 0.15eV, and a 500eV planewave cutoff. We assume that the platinum-H interactions in the reduced state can be described by a z-dependent bonding term. By multiplying the potential with the orbital occupancy n_a , we create a switching function that describes the bond-breaking and formation as the oxidation state changes:

$$\mathcal{V}_{Pt-H} = n_a \left(D_{Pt}^H (1 - \exp(-\alpha_{Pt}^H (z_H - z_0)))^2 - D_{Pt}^H \right)$$

where D_{Pt}^H is the equilibrium bond energy, α_{Pt}^H is the decay constant, and z_0 is the equilibrium position for H on the Pt surface. This bond-breaking switching approximation has been used in the past to describe dissociative adsorption in similar MD models by Calhoun⁶⁹. In the reduced state, \mathcal{V}_{Pt-H} takes a Morse potential form, and it is zero in the oxidized state; instead, the attraction between the proton and the surface takes the form of the well-known image potential, which is grouped with the Coulombic terms. Interaction potential terms not relevant to the electronic Hamiltonian are grouped in with \mathcal{H}_{sol} because these \mathcal{H}_{sol} terms cancel out in the vertical energy gap for the system. Now, we have the total potential for the hydrogen ion:

$$\mathcal{V} = \mathcal{V}_{coulombic} + \mathcal{V}_{Pt-H} + \mathcal{V}_{elyte-ion np}$$

ΔE is defined as the difference between the reduced and oxidized states, i.e., occupancy 1 and 0:

$$\begin{aligned}
\Delta E(\mathbf{R}) &= \mathcal{V}^{red}(\mathbf{R}) - \mathcal{V}^{ox}(\mathbf{R}) \\
&= -(\mathcal{V}_{elyte-ion} - \mathcal{V}_{elyte-ion\ images} - \mathcal{V}_{elyte\ images-ion} + (2z - 1)\mathcal{V}_{ion-ion\ imgs}) \\
&\quad + (z - 1)\mathcal{V}_{\sigma-ion}^H - (z)\mathcal{V}_{\sigma-ion}^{H^+} + (\mathcal{V}_{elyte-ion\ np}^H - \mathcal{V}_{elyte-ion\ np}^{H^+}) + \mathcal{V}_{Pt-H}
\end{aligned}$$

where $\mathcal{V}_{\sigma-ion}^H$ represents the $\mathcal{V}_{\sigma-ion}$ term when the electrode is polarized in accordance with the reduced state charge, and $\mathcal{V}_{\sigma-ion}^{H^+}$ is similarly defined for the oxidized state charge. We exclude the contribution to ΔE from $\mathcal{V}_{\sigma-water}$, since it is an unphysical contribution from the higher-order image charges that arise from the microscopic capacitor configuration. In a real macroscopic electrochemical cell, there are no higher order images to be adjusted as redox occurs, thus there is no higher-order image contribution to the ion orbital energy. However, in the simulation, the surface charges q_{LE} and q_{RE} are correctly updated as q_H varies for the purpose of maintaining the correct potential difference ΔV . A summary of the interaction parameters used is shown in Table 1:

Table 1. Interaction parameters for the redox ion-system potentials.

Parameter	Value
A_O^H	1.10 eV
B_O^H	1.15 \AA^{-1}
A_H^H	3.50 eV
B_H^H	2.60 \AA^{-1}
$D_O^{H^+}$	1.50 eV
$\alpha_O^{H^+}$	2.50 \AA^{-1}
r_0	1.24 \AA
$A_H^{H^+}$	50.0 eV
$B_H^{H^+}$	12.5 \AA^{-1}
D_{Pt}^H	5.81 eV
α_{Pt}^H	1.00 \AA^{-1}
z_0	0.71 \AA

2.5 Summary

We have developed an embedded ANH molecular dynamics approach to study the Volmer reaction in hydrogen electrocatalysis. We make the embedded ANH molecular dynamics approach compatible with controllable cell voltage for the first time. Additionally, we parametrized an interaction potential for the solvated proton as well as for the reduced H – platinum bond. With this approach, we can simulate electronically adiabatic H^+/H^* redox in the Volmer step as a function of the vertical energy gap coordinate and the hydrogen ion's distance from the surface. In the subsequent chapters, we investigate how changes in the structure and dynamics of the electrochemical double layer drive changes in Volmer redox kinetics.

Chapter 3

INSIGHTS INTO SOLVENT AND SURFACE CHARGE EFFECTS IN HYDROGEN ELECTROCATALYSIS

Jon C. Wilson^{1,2}, Stavros Caratzoulas^{1,2}, Dionisios G. Vlachos^{1,2}, Yushan Yan¹

1) Department of Chemical and Biological Engineering, University of Delaware, 150 Academy St, Newark, DE 19713 USA,

2) Catalysis Center for Energy Innovation, University of Delaware, 221 Academy St, Newark, DE 19716, USA.

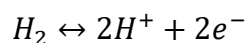
3.1 Abstract

The mechanism of pH-dependent hydrogen oxidation and evolution (HOR/HER) kinetics is still a matter of significant debate. To make progress, we study the Volmer step kinetics on Pt (111) using classical molecular dynamics simulations with an embedded Anderson-Newns Hamiltonian (ANH) for the redox process and constant potential electrodes. We investigate how negative surface charge affects Volmer step kinetics. We find that the redox solvent reorganization energy is insensitive to surface charge changes. The negatively charged surface attracts adsorbed H as well as H^+ , increasing hydrogen binding energy (HBE), but also trapping H^+ in the double layer. While negative surface charge accelerates the oxidation charge transfer, it becomes difficult for the proton to move to the bulk. Conversely, reduction becomes more difficult because the transition state occurs farther from equilibrium solvation polarization. Our results help to clarify how surface charge plays a role in HOR/HER kinetics.

Corresponding Authors: yanys@udel.edu, vlachos@udel.edu, cstavros@udel.edu

3.2 Introduction

Designing efficient and cost-effective electrochemical devices necessitates a deep understanding of the electrochemical interface where there is a rich interplay of physical phenomena. Historically, the study of chemisorption on electrodes has generated fruitful links between the electronic structure of catalysts and their electrocatalytic activity^{26, 65}. The resulting linear scaling relationships from these works have been useful guides for catalyst design; for example, hydrogen binding energy (HBE) correlates well with catalyst activity across several orders of magnitude^{24, 25, 70}. However, emerging research indicates a more detailed microscopic understanding of heterogeneous electron transfer (ET) is needed to resolve ongoing debates about kinetic trends³¹. We are particularly interested in understanding the origin of sluggish alkaline hydrogen oxidation and evolution (HOR/HER) kinetics. At its simplest, the reaction for HOR/HER can be written as follows in acid and base, respectively:



In base, the exchange current density for platinum group metals (PGMs) is about 2 orders of magnitude smaller than in acid. Changes in HBE and water structure, electrode surface charge, cation and hydroxyl adsorption, and variation in HOR/HER mechanism have all been invoked in explanations for pH dependence of HOR/HER activity^{27, 29, 47, 70-73}. These theories have been compared extensively in reviews by others^{31, 37, 74}. Here, our goal is to understand the effect of surface charge on HOR/HER kinetics.

Recently, there has been increasing interest in the potential of zero free charge (PZFC) of catalysts as a descriptor for pH dependent HOR/HER kinetics. As pH is increased, the equilibrium potential for HOR/HER shifts negatively by 59mV/pH unit. However, on Pt (111), the PZFC is about 0.3V vs. SHE and is relatively constant with pH. Following the Nernstian shift in equilibrium potential, the alkaline working potential is farther below the PZFC and the surface is more negatively charged, altering the electrochemical double layer (EDL) structure and composition. Such EDL effects are most relevant within around 1nm of the electrode surface where the local field can exceed 1V/nm and the local concentration of electrolyte species can deviate from the bulk concentration by multiple orders of magnitude. Thus far, mechanistic explanations linking such EDL effects to HOR/HER kinetics have been difficult to establish conclusively³¹.

To make progress in understanding EDL effects, we model the relevant physics of electron transfer and chemisorption with explicit solvent. Following the ideas of Marcus and Hush^{18, 21}, we model solvent dynamics along the collective polarization coordinate, using classical molecular dynamics (MD) to collect solvent fluctuation statistics. We embed the Anderson-Newns Hamiltonian (ANH) to model charge transfer while additionally incorporating controllable electrode potential into this framework for the first time^{22, 60}. Adding controllable electrode potential to the model enables us to study the relationship between surface charge and charge transfer kinetics. Moreover, explicitly modeling the electrolyte atoms allows us to probe the microscopic structure and dynamics of the EDL. By varying the electrode surface potential, we study how surface charge affects the physics of the Volmer step, using H⁺/H at the Pt (111)/water interface as our prototypical case study. To that end, we

perform importance sampling along the collective solvent coordinate to bias the system to sample redox events for the electronically adiabatic reaction and then estimate redox activation energies from potentials of mean force. We show that solvent reorganization energy is insensitive to surface charge at physically relevant potentials. We further show how, instead, the negative electrostatic potential directly affects the kinetic barriers for the redox process by stabilization of the H^+ state near the surface.

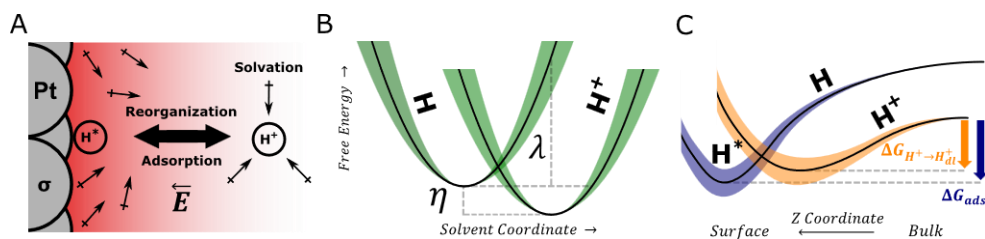


Figure 3.1. Schematics of Volmer reaction along the collective solvent coordinate and proton-surface distance, z . A) Illustration of chemisorption and solvent reorganization around H^+ in the Volmer step at charged Pt (111). Approaching the electrode, H^+ moves through the surface field and loses significant solvation energy before reaching the charge transfer transition state. B) Diabatic free energy curves of the H^+/H pair at fixed z ; solvent reorganization energy, λ , and overpotential, η , are shown. Changes in surface charge can potentially modulate solvent polarization fluctuations, which in turn determines the free energy curvature (green) and solvent reorganization energy. C) Free energies of the H^+/H pair projected onto the z coordinate. Reduced hydrogen at the surface is denoted H^* . Surface charge can affect the energy to move H^+ to the double layer, $\Delta G(H^+ \rightarrow H^*_{dl})$, by changes in electrostatics and solvation. In the adiabatic representation, H^* has a partial charge, and thus HBE is also affected by electrostatics. More broadly, the change in double layer structure and composition with changing surface charge can also indirectly affect the free energy of hydrogen near the surface.

To frame how we study surface charge effects, we briefly recap the possible mechanisms by which surface charge can affect HOR/HER kinetics. In the 1930's,

A.N Frumkin described how the local potential near the surface affects the kinetics for heterogeneous charge transfer^{44, 75}. Surface charge alters the electrochemical potential of double layer ions, inducing concentration polarization as well as modulating the free energy change and activation energy associated with redox reactions. Such effects are often called the “Frumkin effect” or “Frumkin correction” in the literature.

Beyond the direct electrostatic effect on ions, the surface electric field also polarizes the solvent, which may affect redox kinetics. Such electric field effects are complicated by the tendency for water to order at the surface. For example, at the catalyst surface, favorable platinum-water interactions induce water molecules to form a structured hydrogen bonding network. Moreover, the interfacial region has a reduced dielectric constant owing to slow orientational relaxation. In Ledezma-Yanez’s view, the water network becomes even more rigid as the interfacial field strength increases, impeding motion of charged species through the double layer (i.e., with respect to z), slowing alkaline HER kinetics⁴⁶. On the other hand, based on dielectric continuum theory, the reorganization energy for electron transfer should diminish when strong surface fields induce dielectric saturation, decreasing the redox activation barrier⁴¹. In Figure 1, we summarize these perspectives schematically and conceptualize the reaction as proceeding along two reaction coordinates: the collective solvent coordinate and the ion’s distance from the surface. In Figures 1B-1C, we decompose the surface charge EDL effects onto the two reaction coordinates. The Volmer step proceeds on the 2D surface, and trends in activation energy are governed by changes in free energies with respect to both coupled coordinates. In the following sections, we measure both how surface charge directly affects the electrostatics of the redox pair H^+/H as well as how it affects double layer solvent structure and reorganization.

3.3 Results

3.3.1 Diabatic Free Energy Curves for HER/HOR.

The solvent coordinate random variable, denoted ΔE , is modeled using the difference in potential energy between the redox ion's reduced and oxidized states at a fixed nuclear configuration, i.e. the vertical energy gap:

$$\Delta E(\mathbf{R}) = V^{red}(\mathbf{R}) - V^{ox}(\mathbf{R})$$

where \mathbf{R} is the set of all nuclear coordinates of the system at a given time and V^{red} , V^{ox} are the energies of the reduced and oxidized states given by the sum of interaction potential contributions between the ion and the system. Notably, here ΔE also includes contributions from the fluctuating charges on the constant-voltage electrodes. To estimate solvent reorganization energy, we first compute the diabatic free energy curves when the electrode is at the PZFC (hereafter shortened to PZC), shown in Figure 3.2. (Diabatic surfaces correspond to electronic states whose character, neutral H or H^+ , does not change with molecular geometry—the solvent polarization specifically—and electron transfer implies that the system has crossed from one diabatic potential to the other.) The diabatic redox overpotential at fixed z is related to the Fermi level of the metal by the energy conservation relation:

$$\eta = \epsilon_a - \epsilon_f + \Delta e_{min}^{H^+} - \lambda$$

where ϵ_a is the proton's vacuum level, ϵ_f is the Fermi level, $\Delta e_{min}^{H^+}$ is at the minimum of the proton diabatic free energy, i.e., equilibrium solvation, and λ is the solvent reorganization energy. Note that specific values of the random variable ΔE are denoted by Δe . The solvent reorganization energy is calculated to be 5.5 eV in bulk, higher than previous estimates of 3-4 eV⁵⁷. The reorganization energy decreases to 3.2 eV at $z = 2.0 \text{ \AA}$.

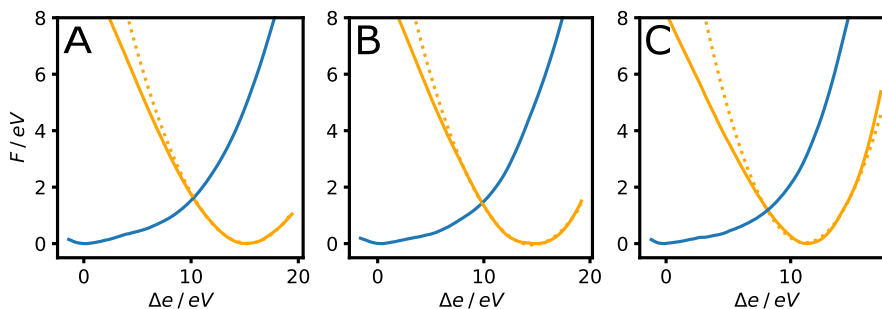


Figure 3.2. Diabatic free energies for H^+ and reduced H along the solvent coordinate at fixed z . The reduced state free energies are calculated by the relation $F^{\text{H}}(\Delta e) = F^{\text{H}^+}(\Delta e) + \Delta e + \epsilon_a - \epsilon_f$ and the overpotential is set to $\eta = 0$ in each case for ease of comparison. A) $z = 4.0 \text{ \AA}$, B) $z = 3.0 \text{ \AA}$, C) $z = 2.0 \text{ \AA}$. The cell electrostatic potential is set to $V - V_{\text{pzc}} = 0 \text{ V}$, i.e., the PZC for both electrodes. The orange and blue curves correspond to the oxidized and reduced states, respectively. Parabolas fitted near the proton minimum are shown as dashed lines.

In Figure 3.2, moving toward the surface, $\Delta e_{\text{min}}^{\text{H}^+}$ decreases due to proton desolvation with a concomitant decrease in λ . In other words, Δe decreases when the proton potential energy becomes less negative. The free energy curves markedly deviate from the symmetric parabolic behavior of Marcus theory, which indicates the solvent polarization does not respond linearly over the whole range. In addition, the curvature of the neutral state's (H atom) free energy profile is smaller curvature than the charged state. As the curvature is inversely proportional to $\langle (\delta \Delta E)^2 \rangle$ (the variance in the solvent collective variable, ΔE), its smaller value is a manifestation of the loose solvent organization around the neutral H atom. In contrast, the strong field around the H^+ strongly polarizes its solvation water.

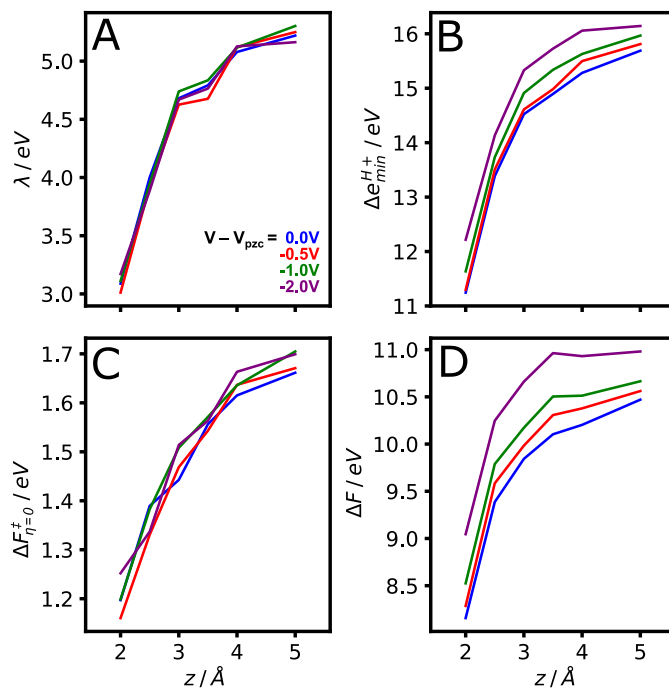


Figure 3.3. Effect of surface charge on diabatic free energies at fixed z . A) solvent reorganization λ ; B) equilibrium Δe value for H^+ , $\Delta e_{\min}^{H^+}$; C) free energy to reach the diabatic crossing with the effect of overpotential subtracted off, $\Delta F_{\eta=0}^{\ddagger}$; and D) reduction free energy change, ΔF , for the diabatic curves where $F^H(\Delta e) = F^{H^+}(\Delta e) + \Delta e$. The blue, red, green, and purple curves are computed from diabatic free energy curves at electrode voltages relative to PZC of $V - V_{\text{pzc}} = 0 \text{ V}$, -0.5 V , -1 V , -2 V , respectively.

Next, we vary the electrode potential V and repeat the calculations presented in Figure 3.2 for fixed z values in order to explore how the electric field of the electrode affects the diabatic free energy profiles. We have simulated a capacitor cell filled with electrolyte and control the overall cell potential, ΔV . In Figure A.1, we establish the relationship between cell potential, single electrode potentials, and surface charge. The potential of the electrode near H is defined on an absolute scale such that $V - V_{\text{pzc}} = -\Delta V/2$. Figure 3.3A shows that the monotonic decrease in λ with decreasing z persists at non-zero electrode potentials, once again, on account of the proton being

progressively desolvated as it approaches the surface. More interestingly, at fixed values of z *the variation in λ with V is statistically insignificant*. Correspondingly in Figure 3.3C, there is no obvious trend in the intrinsic barrier. The electrode's field ($\sim 0.1 \text{ V}/\text{\AA}$) is not strong enough to disrupt the polarization of the solvent experiencing the proton's strong field ($> 1 \text{ V}/\text{\AA}$ within 3\AA). The very limited effect of the electrode field on the reorganization energy, even at very short distances from the surface, is manifested in the unchanging equilibrium distribution of the orientation of water molecules in the proton's solvation shell (see Figure A.2), indicating that the solvent polarization is also unchanged.

As the surface is negatively charged, nearby H^+ experiences an increasingly more negative potential, increasing $\Delta e_{\text{min}}^{\text{H}^+}$ and the reduction ΔF (Figures 3.3B and 3.3D). The increase in ΔF with more negative surface potential resembles the Frumkin effect⁴⁴, where the driving force for redox must be corrected to include the influence of the ion's electrostatic potential near the charged surface. The effect observed here is due to the incomplete screening of the field at the position where redox occurs. As we will show later, the H^+ local electrostatic potential plays an important role in surface charge dependent kinetics.

3.3.2 Potential-dependent solvent dynamics.

Having established that λ is insensitive to the interfacial field, we now explore how solvent dynamics change with field strength, which could also impact redox kinetics. Interestingly, our calculations do not support the Ledezma-Yanez view that the water network becomes more rigid with increasing interfacial field strength⁴⁶. To measure trends in dipolar relaxation times, we calculate the normalized dipole autocorrelation function for individual water molecules as follows:

$$C_{\mu\mu}(t) = \frac{\langle \delta\mu(t) \cdot \delta\mu(0) \rangle}{\langle \delta\mu(0)^2 \rangle}$$

where μ is the unit dipole vector of a water molecule, $\delta\mu(t)$ is fluctuation from the mean, and the ensemble average is conditional over waters in a given region relative to the surface.

In Figure 3.4, we plot the conditional dipole autocorrelation function for waters around the outer Helmholtz layer and for waters adsorbed on the surface, calculated for three electrode potential values, $V - V_{\text{pzc}} = 0 \text{ V}, -1 \text{ V}, -2 \text{ V}$. At short times (<1 ps), librational relaxation is dominant. At longer times, relaxation near the surface (Figure 3.4B) is much slower than in the outer Helmholtz layer (Figure 3.4A). Slower relaxation indicates a more sluggish solvent near the surface and concomitant decrease in the dielectric susceptibility (related to the negative of the derivative of $C_{\mu\mu}(t)$ ⁷⁶), which implies weaker equilibrium polarization of the surface water due to the ordering induced by the surface.

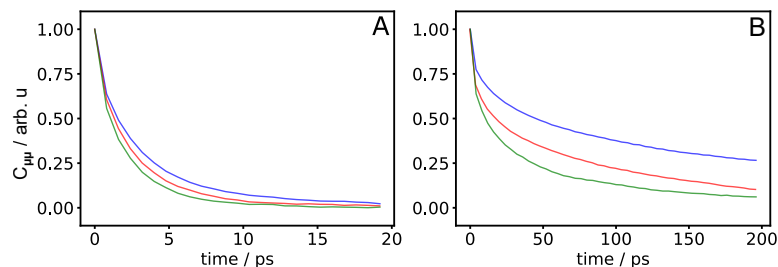


Figure 3.4. Dipole vector autocorrelation function for water molecules near the Pt (111) electrode. A) Double layer waters near the outer Helmholtz layer within $4 < z < 5$ Å. B) Adsorbed waters where $z < 3$ Å. Surface water is attracted to the Pt surface, and the lattice spacing of Pt (111) is suitable for water to form a network of hydrogen bonds parallel to the electrode plane. Consequently, the reorientation time of water increases at the surface due to confinement effects. (Blue, red, and green curves correspond to water near the electrode with voltages of $V - V_{pzc} = 0$ V, -1 V, -2 V, respectively.)

At increasingly negative electrode potentials, we see increasingly faster relaxation both at the surface and in the outer Helmholtz layer and thus higher polarization. The change in polarization due to the electrode field seems to be more pronounced for surface water. Remarkably, although water retains some of its rigidity due to the presence of the surface (inferred by the lower susceptibility), the rotational mobility of the surface water seems to increase with $|V|$. It is likely that solvent dynamics accelerate at negative voltages because the interfacial field disrupts the hydrogen bond network at the surface; the average number of hydrogen bonds per water decreases as hydrogen bonding is disrupted parallel to the electrode plane (Figure A.3).

We expect that the relaxation time for waters in the vicinity of the proton are more relevant to the hydrogen ion dynamics at the Volmer transition state in comparison to the average relaxation behavior of EDL waters. Thus, we show that the dipole relaxation of water in the proton's solvation shell similarly becomes faster

when the surface is more negative (Figure A.4). We also compute the autocorrelation of the proton's electrostatic potential (Figure A.5) to estimate changes in the solvation time, and we find that it also accelerates somewhat at more negative potentials, consistent with a slight *increase* in the electron transfer rate⁷⁷. The decrease in solvation time is significant when the proton is close to the surface at $z = 2 \text{ \AA}$ but insignificant at $z = 6 \text{ \AA}$, again, because the interfacial field accelerates dipolar relaxation more so for surface waters than non-adsorbed waters. Contrary to expectations, the solvent network is less rigid near the negative electrode as well as near the proton, and another explanation must be invoked to understand surface-charge dependent HOR/HER kinetic trends.

3.3.3 Adiabatic Free Energy Surfaces.

To understand the interplay between chemisorption, electric potential effects, and solvent reorganization, we simulate the adiabatic free energy surfaces for the Volmer step. Close to the surface, electronic coupling between the ion and the surface is strong, and the reaction may be treated as electronically adiabatic. We perform importance sampling to obtain the potentials of mean force with respect to the solvent collective motion (ΔE) and the proton translational motion in the z -direction.

It is important to clarify the relationship between the reaction overpotential and the electrode potential in the context of this model. When the ANH is embedded into classical MD, the Fermi level is a model input parameter which determines the overpotential. The Fermi level corresponds to the real potential of the *uncharged* electrode which is coupled to the hydrogen ion. The applied potential difference ΔV is another independent input parameter which sets the cell potential. In a real cell, these two variables are inextricable; as the cell potential is changed, the working electrode's

overpotential and electrostatic potential vary together, connected by the electrochemical potential of electrons in the metal. The behavior of changing the electron electrochemical potential is known: at more negative applied potentials, the upward shift in Fermi level biases the reaction to reduction. In Figure A.6, we show how increasing the ANH overpotential with a commensurate change in the surface potential biases the reaction to reduction. Here, however, we emphasize that our aim is to explore how changing the surface electrostatic potential $V - V_{pzc}$ affects the Volmer step, which is useful for addressing the claim that the PZC of an electrode is relevant as a kinetic descriptor. Therefore, we set a constant ANH overpotential across different cases, and we vary ΔV . Effectively, we control $V - V_{pzc} = -\Delta V/2$ for the working electrode. We set the Fermi level such that the reaction overpotential is slightly biased to adsorbed hydrogen.

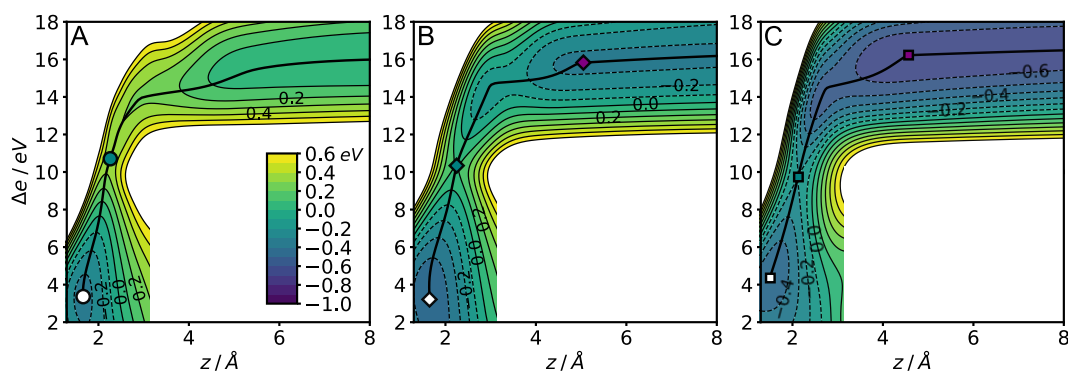


Figure 3.5. Simulated adiabatic free energy surfaces of the H^+/H redox pair near a Pt (111) electrode as functions of the collective solvent coordinate, Δe , and the H 's z -coordinate along the normal to the surface, at varying cell electrostatic potentials: A) $V - V_{pzc} = 0$ V B) $V - V_{pzc} = -1$ V C) $V - V_{pzc} = -2$ V . The Fermi level is set such that $\epsilon_a - \epsilon_f = -10.19$ eV. Minimum free energy paths (MFEP) are shown as traced solid lines. The white filled shapes mark the H^* minima, the teal shapes mark the redox saddle point, H^\ddagger , and the purple shapes mark the H^+_{dl} minima at negative voltages. The hydrogen adsorption energy is calculated as the free energy difference between the H^* minima and H^+ in the bulk, which is the reference for all cases.

Figure 3.5 shows the adiabatic free energies for three values of the electrode potential. Approaching the surface, H^+ is attracted by the image potential and the negative surface. Below $z = 4 \text{ \AA}$, H^+ becomes less coordinated to nearby waters, see Figure A.7. At more negative $V - V_{pzc}$, H^+ becomes trapped near the surface around $z = 4 - 5 \text{ \AA}$, where it experiences a significant negative potential but still retains a solvation structure like that of bulk H^+ . In comparison to the PZC, the trapping of H^+ in the double layer results in a later reduction transition state with concomitant increase in the reduction activation free energy. At $z < 3 \text{ \AA}$, most of the change along the minimum free energy pathway (MFEP) is solvent reorganization. Adsorption energies of H^* at this value of $\epsilon_a - \epsilon_f$ are calculated to be $-0.34 \pm 0.03 \text{ eV}$ at $V - V_{pzc} = 0 \text{ V}$, $-0.49 \pm 0.03 \text{ eV}$ at -1 V , and $-0.47 \pm 0.03 \text{ eV}$ at -2 V .

In Figure 3.5, we connected the three cases with a constant reference state to compare the changes in free energies as ΔV is varied. Since we have not considered the presence of electrolyte salt, the solution has a long Debye length, and H^+ is influenced by the surface field even far away. We select the constant reference state for all the adiabatic simulations as the proton at $z = 25 \text{ \AA}$ and $V - V_{pzc} = 0 \text{ V}$ where it is not influenced by excess surface charge. Our choice of reference is consistent with experiment: in a macroscopic cell, protons ultimately are sourced from the bulk, i.e., where the proton activity is determined purely by its solution chemical potential. As shown in Appendix A, as the cell potential is varied, the only difference in proton free energy in the solution is due to the difference in its electrostatic potential, which is easily calculated to establish a common scale.

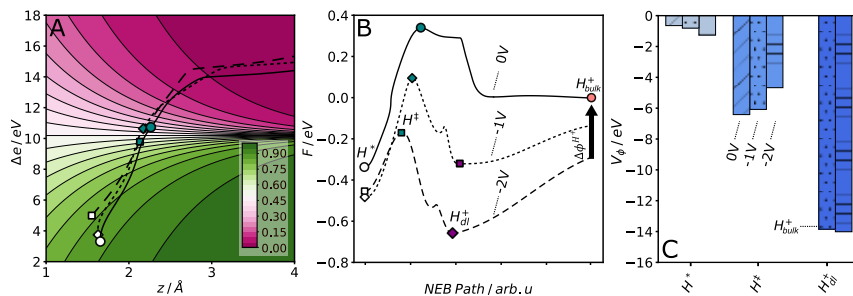


Figure 3.6. Further analysis of the adiabatic free energy surfaces at varying $V - V_{pzc}$. A) Contours of expected H orbital occupancy $\langle n_a \rangle$ versus the collective solvent coordinate, Δe , and the z-coordinate of redox H along the normal to the surface. B) Free energy profiles along respective MFEPs of adiabatic free energy surfaces shown previously in Figure 4. C) Average electrostatic potential energy $V_\phi = q_H \langle \phi \rangle$ experienced by H^* , H^\ddagger , H_{dl}^+ at the three applied potentials. The partial charge of hydrogen is related to its occupancy by $q_H = 1 - \langle n_a \rangle$. In A: The overlaid solid, dotted, and dashed lines are the minimum free energy paths for the free energy surfaces corresponding to $V - V_{pzc} = 0$ V, -1 V, -2 V, respectively. In B: White shapes: Adsorbed H (H^*). Teal shapes: Redox transition states (H^\ddagger). Purple shapes: Proton minima in the double layer (H_{dl}^+). Pink circle: bulk proton reference state (H_{bulk}^+). In C: the bars correspond to 0 V (diagonal hatches), -1 V (dots), and -2 V (horizontal hatches). V_ϕ for the reference, H_{bulk}^+ , is shown for comparison to H_{dl}^+ .

The changes in hydrogen binding energy can be understood in terms of the expected orbital occupancy $\langle n_a \rangle$ of H^* and its electrostatic attraction to the surface. In Figure 3.6A, we show how $\langle n_a \rangle$ changes along the MFEPs for the adiabatic surfaces shown in Figure 3.5. The equilibrium ΔE value for H^* , $\Delta e_{min}^{H^*}$, is still significantly positive, due to the stabilization of the oxidized state by water and the polarizable surface. Consequently, the oxidized state is more favored in comparison to adsorbed H *in the absence of solvent*, and $\langle n_a \rangle$ ranges from 0.8-0.9. The expected occupancy of H^* determines its partial positive charge, which takes a value of $q_H = 1 - \langle n_a \rangle$. At $V - V_{pzc} = 0$ V, q_H for H^* is about $+0.12$, increasing to $+0.16$ at $V - V_{pzc} = -2$ V. Furthermore, going from $V - V_{pzc} = 0$ V to -1 V and to -2 V, H^* experiences a more

negative electrostatic potential due to the surface charge. From Figure 3.6C, the electrostatic potential energy of H^* correspondingly becomes more negative, and consequently binding energy increases. While H adsorption becomes more favorable by 0.15 eV going from 0 V to -1 V, there is no similar increase as the potential is further lowered to -2 V. At very negative potentials, the stronger electrostatic attraction to the surface is offset by a weaker Pt-H bond as $\langle n_a \rangle$ for H^* decreases.

The experimental voltametric feature for H adsorption on Pt (111) is quite broad and we cannot directly compare our theoretical HBE trends to experiment without a model of coverage effects. We also cannot attempt to explain pH-dependent hydrogen electrosorption peak shifts with this argument due to the neglect of electronic structure changes that accompany changes in absolute electrode potential⁷⁸. However, because the change in HBE observed here is likely due to surface charge, we hypothesize that shifts in the PZC induced by surface adsorbates cause non-Nernstian shifts in HBE⁷⁹. In the future, grand-canonical DFT calculations of hydrogen-metal electronic interactions with explicit solvation may be useful to estimate the partial charge of H^* with greater quantitative accuracy⁷⁸.

We observe that the oxidation event at $V - V_{pzc} = -2$ V is more facile than at the PZC, however, H_{dl}^+ cannot easily escape the double layer, slowing HOR kinetics. In Figure 3.6B, we plot the free energy profiles along the MFEPs of the adiabatic surfaces in Figure 3.5; they track the progress of the reaction from surface H^* to the bulk solution H^+ at $z = 25$ Å. The oxidation activation barrier decreases from 0.67eV to 0.58eV to 0.29eV going from $V - V_{pzc} = 0$ V to -1 V and to -2 V, respectively. However, in the $V - V_{pzc} = -1$ V case, there is a barrier of 0.31 eV for the proton to move from the double layer around 5 Å to the bulk. In the $V - V_{pzc} = -2$ V case, that

barrier increases to 0.68 eV. In the double layer free energy well, the H atom is proton-like in character and $\langle n_a \rangle \cong 0.005$, thus the partial charge of H_{dl}^+ is $q_H \cong +.995$ and H_{dl}^+ is attracted to the negative surface. In the present case of dilute solution, there are insufficient electrolyte ions to screen the surface charge at 5-6 Å from the surface. However, in cases where the ionic strength is high, the negative surface is expected to concentrate cations in the double layer region, which will screen the surface charge and diminish the depth of the observed proton free energy well.

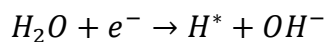
At more negative surface potentials, the reduction activation energy rises due to the increase in reduction ΔF , notably not due to changes in λ . At $V - V_{pzc} = -2V$, the reduction activation energy is about 0.15eV larger than at the PZC. It is seemingly counterintuitive that the reduction becomes more difficult, since the H^+ should be increasingly attracted towards the negatively charged surface where reduction occurs—in this case, the Frumkin effect would predict an *increase* in reduction kinetics, rather than a decrease. However, there is significant coupling between the two reaction coordinates, that is, we must consider how the solvent reorganizes as the proton proceeds toward the surface. In agreement with Marcus-Hush theory (and with Hammond's postulate), the reduction transition state shifts towards the H^* state along the solvent coordinate as the reduction ΔF increases. At the saddle point H^\ddagger , $\langle n_a \rangle$ is 0.42 at 0 V and increases to 0.57 at $-2 V$, indicating an increase in the reduction charge transfer coefficient, consistent with a later transition state. At the transition state, the solvent's inertial (mainly rotational) polarization is farther out of equilibrium with respect to solvated H^+ when the surface is more negative, increasing the reduction activation energy. In Figure 3.6C, V_ϕ at H^\ddagger is increasingly less negative relative to H_{dl}^+ as $V - V_{pzc}$ is set more negatively, consistent with a decrease in

solvation energy at the TS. Changes in the coordination numbers of water atoms around H^{\ddagger} further confirm weaker solvation at negative voltages (Figure A.8). Earlier, we observed that λ is unaffected by V . λ is a measure of the intrinsic redox barrier, proportional to the equilibrium polarization difference between the two states. To be clear, near more negatively charged electrodes, the transition state simply occurs farther from equilibrium H^+ solvation *due to the increase in ΔF* .

3.3.4 Implications for pH-dependent HOR/HER kinetics.

We have studied the electrosorption of hydrogen at the Pt (111) surface, often called the acidic Volmer step. However, to make the direct comparison to experimental results for alkaline HOR/HER, we must also consider how hydroxide participates in the reaction. While we have not simulated OH^- here, our insights from the electrostatics and solvent reorganization data could clarify existing debates.

Recently, there has been considerable debate regarding the importance of surface charge and hydroxide binding as descriptors for alkaline HOR/HER kinetics. For example, it is unclear whether $Ni(OH)_2$ promotes alkaline HER by shifting the PZC or by a bifunctional effect, or possibly even both. Several authors have argued that alkaline HER is rate limited by water splitting at the interface since there is very little free H^+ available as a proton source³⁵⁻⁴⁰. Markovic et al. proposed that alkaline HER kinetics may be tailored by tuning both HBE as well as the energy required to dissociate water, with the following RDS³⁵:



Where tuning surface oxophilicity promotes the dissociation of water at the surface by stabilization of OH^* , and oxophilic surface species such as $Ni(OH)_2$ are proposed to accelerate water splitting on catalysts which have favorable HBE. By studying

decorated step sites on Pt, McCrum et al. clarified how hydroxide binding energy (OHBE) affects the activation energy in the HOR/HER bifunctional mechanism⁴⁰. On the other hand, Ledezma-Yanez and Sarabia et al. argue that alkaline HER may be limited by OH⁻ transport through the double layer, where solvent structure has been thought to be more rigid and difficult to reorganize due to negative surface charge^{46, 47}. These authors attributed faster HER for Ni(OH)₂ on Pt (111) to a decrease in negative surface charge. Furthermore, Rebollar et al. showed that adding caffeine to Pt surfaces similarly shifts the PZC negatively and improves alkaline HOR and HER kinetics⁸⁰. Rebollar et al. also observed a weakening of OHBE on Pt(pc), inconsistent with the OHBE theory. Although OHBE may be an important catalytic descriptor, it is not the whole story, and it appears that surface charge is yet another kinetic descriptor.

Here, we showed that negative surface charge does not appreciably impact solvent reorganization energy. Moreover, we show that solvation relaxation is slightly faster near the surface when it is negatively charged, indicating the solvent network does *not* become more rigid. Interestingly, our findings are consistent with experimental data of Rebollar et al.⁸⁰ Using the HER/HOR kinetic isotope effect as a probe, the authors concluded negative surface charge did not cause sluggish solvent dynamics, rather, negative surface charge was associated with slightly faster dynamics. Rebollar et al. then concluded that sluggish alkaline kinetics occur due to changes in the activation energy, not the Arrhenius prefactor. Our work and Rebollar's findings together show that the effect of surface charge on HOR/HER kinetics is not mediated by changes in solvent reorganization energy or dynamics.

We suggest that the modulation of H⁺/OH⁻ interfacial electrochemical potentials by surface charge directly affects redox activation barriers, which could

explain why the PZC is correlated with HOR/HER kinetics. This argument is experimentally supported by recent estimates of electrostatic potential near the interface. Using a pH-sensitive probe reaction, Ryu and Surendranath showed that there is incomplete screening near the outer Helmholtz layer (OHL) on Pt/C at HOR/HER potentials up to a significant ionic strength of 280 mM⁸¹. The Volmer HOR/HER transition state is even closer to the surface, around 2 – 2.5 Å. At these small distances, the local electrostatic potential at the transition state is even more incompletely screened relative to the OHL and thus is strongly sensitive to surface charge. In our view, the change in the local electrostatic potential of H⁺, not changes in solvent polarization induced by the surface electric field, is a relevant factor that modifies the HOR/HER activation barrier.

We can outline a plausible mechanism by which surface charge affects both alkaline HOR and HER kinetics. In base, since the Volmer equilibrium potential is much more negative than in acid, the reduced state is more favored relative to bulk H₃O⁺, and OH⁻—not H₂O—must directly aid the removal of H* for HOR. When the electrode surface is negatively charged, just as we showed H⁺ is more energetically favorable near the surface, OH⁻ will be less favorable. As Ramaswamy et al. earlier concluded, the energy penalty to bring OH⁻ to the negative surface should result in higher HOR activation energy⁷⁴. The HER activation energy is also expected to be larger when OH⁻ is a product, since it is unfavorable for OH⁻ to form near the negative surface as water splits. One caveat of this work is that we have not simulated concentrated solutions and therefore neglect the accumulation/depletion of H⁺ and OH⁻ in the double layer and their associated first-order kinetic rate dependence. Clearly, understanding surface charge effects in alkaline HOR/HER deserves further

study. Studying how OH^- interfacial concentration responds to surface charge and its interrelationship with supporting electrolyte effects will be left to future work.

3.4 Conclusions

Using controlled-potential Anderson-Newns Hamiltonian molecular dynamics, we have computed the diabatic and adiabatic free energies for the Volmer step on Pt (111). The Volmer step does not obey the linear-response approximation with respect to solvent polarization over the whole range, and polarization fluctuations around H^* are much broader compared to H^+ . At physically relevant applied potentials below the PZC, solvent reorganization energy for the Volmer step is insensitive to surface charge, and solvation dynamics do not become more sluggish. As the surface becomes more negatively charged, we predict an increase in HBE due to electrostatic interactions between H^* and the surface. Additionally, we find that H^+ is highly attracted to the negatively charged surface and cannot easily leave to bulk. In the reduction direction, stabilization of H^+ by the negatively charged surface results in a late transition state where the solvent is farther from equilibrium H^+ solvation polarization, resulting in a higher activation energy.

Since surface charge effects on HOR/HER kinetics cannot be explained by changes in solvent reorganization or dynamics, we suggest that Volmer activation barriers change are affected by changes in H^+/OH^- electrochemical potentials in the double layer. Our findings help to clarify the role of surface charge in hydrogen electrocatalysis and highlight the need to engineer the double layer and catalyst surface charge for active alkaline catalysts.

3.5 Computational Resources

This research used resources of the National Energy Research Scientific Computing Center (NERSC), a U.S. Department of Energy Office of Science User Facility located at Lawrence Berkeley National Laboratory, operated under Contract No. DE-AC02-05CH11231 using NERSC award m1893 for years 2021-2022.

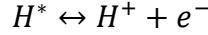
This research was also supported in part through the use of DARWIN computing system: DARWIN – A Resource for Computational and Data-intensive Research at the University of Delaware and in the Delaware Region, University of Delaware, 2021, URL: <https://udspace.udel.edu/handle/19716/29071>

This work was supported as part of the Catalysis Center for Energy Innovation, an Energy Frontier Research Center funded by the US Dept. of Energy, Office of Science, Office of Basic Energy Sciences under award number DE-SC0001004

3.6 Methods

3.6.1 Electronic Hamiltonian.

Here we simulate the Volmer step on the Pt (111) surface to gain insight into interfacial-field dependent HOR/HER kinetics:



In heterogeneous electron transfer, the redox ion electronic state couples to the catalyst continuum of electronic states, and the ion orbital's energy is additionally coupled to the fluctuating solvent. We treat this interaction approximately by utilizing solutions to the Anderson-Newns Hamiltonian, which has been successfully used to study heterogeneous ET reactions. The electronic Hamiltonian term is embedded in the molecular dynamics Hamiltonian to describe the electronically adiabatic reaction:

$$\mathcal{H} = \mathcal{H}_{sol} + \mathcal{H}_{el}$$

Where \mathcal{H}_{sol} represents the Hamiltonian for the electrolyte-electrolyte, electrolyte-catalyst, and all other interactions not involving the redox ion electronic state. The electronic Hamiltonian term simplifies to yield an analytic form when we consider a single redox ion state with broadband coupling to the metal states:

$$E_0(\Delta E) = \frac{1}{2}\Delta E + 1/\pi(\epsilon_a + \Delta E - \epsilon_f)\tan^{-1}\left[\frac{\epsilon_f - (\epsilon_a + \Delta E)}{\Delta}\right] + \frac{\Delta}{2\pi}\ln\left[(\epsilon_a + \Delta E - \epsilon_f)^2 + \Delta^2\right]$$

Where ϵ_f is the Fermi level of the metal, Δ is the metal-ion coupling matrix element, and ΔE is the random variable for the vertical excitation coordinate which tracks the collective solvent fluctuations. As the MD simulation proceeds, Δ and ΔE are calculated at every timestep and used to update the electronic term $E_0(\Delta E)$ and the associated electronic forces. The form of E_0 used here follows from the behavior of the expected occupancy of the orbital state, which varies with ΔE as follows:

$$\langle n_a(\Delta E) \rangle = \frac{1}{2} + \frac{1}{\pi} \tan^{-1} \left(\frac{\epsilon_f - (\epsilon_a + \Delta E)}{\Delta} \right)$$

The occupancy smoothly switches from 0 to 1 as ΔE decreases, i.e. accompanying proton desolvation. The charge transfer occurs most rapidly as ΔE crosses the Fermi level, and the rate of change is proportional to the broadening, Δ . We fit the electronic coupling to a function which decays exponentially with z :

$$\Delta(z) = \Delta_0 \exp(-\beta z)$$

Where $\Delta_0 = 16eV$ and $\beta = 1.1\text{\AA}^{-1}$. These values are approximated using DFT calculations and provide a reasonable estimate of the broadening— 3.0eV for adsorbed hydrogen. We have developed custom code for the embedded-ANH term in LAMMPS and perform all MD simulations in LAMMPS. More detail about the derivation of the electronic term can be found in previous works by Grimley and Newns and in Chapter 2^{22, 82, 83}. The details of the H+\H interaction potentials are also available in Chapter 2.

3.6.2 Diabatic and Adiabatic Simulations.

In the Volmer step, we model the reaction as proceeding along the relevant reaction coordinates of the collective solvent polarization ΔE and the hydrogen's distance from the surface z . We perform importance sampling along ΔE and z in canonical MD simulation at 300K. In diabatic fixed- z simulations, \mathcal{H}_{el} is not included in the total Hamiltonian, and the ion is fixed in one of the two states. For each diabatic curve, we used 33 umbrella sampling windows of length 60ps each. Simulations for each window were performed in series, with each simulation picking up from the last snapshot of the prior adjacent window. Equilibration for the initialized system lasted 2ns and subsequent equilibration for the first bias window lasted 60ps. The restraining potential was smoothly ramped from one window to another initially and subsequent equilibration lasted 6ps. Unbiased free energies were estimated using WHAM. For 1D diabatic curves, block averaging of the window means was performed to estimate error

and ensure adequate sampling. The standard error in the diabatic reduction free energy change for redox at fixed z is estimated to be ± 0.03 eV using the procedure from Zhu et al.⁸⁴. For the 2D adiabatic surfaces, similar harmonic restraint window settings were used to sample along ΔE , and we additionally sample along the z coordinate in window increments of 0.2 \AA . Errors in calculated adsorption energies are similarly estimated to be ± 0.03 eV.

3.6.3 Electrolyte Interaction Potentials and Simulation Cell Details.

The interaction potentials for the \mathcal{H}_{sol} terms include both the solvent-solvent and solvent-metal contributions. For the solvent-solvent contribution, we use TIP3P waters⁸⁵. For the water-metal potential, the non-Coulombic interactions are modeled using the Siepmann and Sprik force field⁸⁶, and the Coulombic interactions are modeled using the constant potential method from Voth's group⁶⁰. For all short-range interactions, we use a cutoff of 12.0 \AA . Long-range coulomb interactions are computed using the PPPM solver with an RMSE force accuracy setting of $0.14 \text{ meV \AA}^{-1}$ in LAMMPS. The k-space slab correction is used for long-range electrostatics in the z direction with a slab vacuum length of $5.0 \times$ the cell z length. A small timestep of 0.3 fs was used due to the fast motion of the H^+ and provided good energy conservation.

For the capacitor cell geometry, the electrolyte region is defined by a box of size $x = 24.0 \text{ \AA}$, $y = 24.9 \text{ \AA}$, $z = 50.0 \text{ \AA}$. Two Pt electrodes with exposed (111) facets are placed on either side of the electrolyte, each containing 3 layers of Pt atoms. The electrolyte contains 960 rigid waters and yields an average density equal to the bulk density of TIP3P waters, $\rho = 0.98 \text{ g cm}^{-3}$. The electrolyte Pt atoms are frozen and not integrated in the Verlet algorithm. The top layer of Pt atoms on each electrode is chosen as the conducting plane where constant potential is maintained.

Chapter 4

INVESTIGATING NON-COVALENT CATION EFFECTS IN THE VOLMER STEP ON Pt (111) WITH MOLECULAR DYNAMICS

Jon C. Wilson^{1,2}, Stavros Caratzoulas^{1,2}, Dionisios G. Vlachos^{1,2}, Yushan Yan¹

1) Department of Chemical and Biological Engineering, University of Delaware, 150 Academy St, Newark, DE 19713 USA,

2) Catalysis Center for Energy Innovation, University of Delaware, 221 Academy St, Newark, DE 19716, USA.

Corresponding Authors: yanys@udel.edu, vlachos@udel.edu, cstavros@udel.edu

Abstract. We study the Volmer redox event on Pt (111) in two electrolyte solutions, 1M NaCl and 1M CsCl, to investigate how the choice of cation type affects HOR and HER kinetics. It is well-established that alkali cations inhibit HOR and HER in order of increasing cation size, but the mechanism is not well understood. We show that the redox reorganization energy is larger near the surface in the electrolyte containing Cs⁺ compared to the electrolyte containing Na⁺. However, surprisingly, the increase in reorganization energy is not due to the solvent but due to the reorganization of the ions. Outer Helmholtz Layer Cs⁺ situates closer to reduced H compared to H⁺, and Cs⁺ translation affects the electrostatic fluctuations in the collective reorganization process. Moreover, the high interfacial density of solvated Cs⁺ ions hinders the approach of H⁺ to the surface, reducing the entropy of H⁺ and thus increasing the activation energy for the Volmer step.

4.1 Introduction

It has become clear that designing catalysts with high activity for electrochemical reactions necessitates tuning both the structure and composition of the electrochemical double layer (EDL), in addition to the usual approach of engineering catalyst-ion electronic interactions^{31, 45, 87}. Specifically, the importance of non-covalent interactions between redox species and other electrolyte ions in the EDL has been emphasized in recent research. For example, Huang et al. showed that for alkaline hydrogen evolution and oxidation (HOR/HER), changing the cation in the electrolyte from Cs⁺ to Li⁺ resulted in an improvement of two orders of magnitude on polycrystalline platinum (Pt(pc))⁴⁸. Here, we are particularly interested in understanding the molecular origin of electrolyte effects on HOR/HER kinetics.

The type and concentration of EDL cations have been proposed to alter Volmer step solvent reorganization energy⁴⁸, block active sites⁸⁸, change water binding energy and structure^{32, 34, 48}, and electrostatically modulate the energy of EDL species^{73, 87, 89}. However, the relative importance of these proposed effects is still unclear. To better understand these complexities, we study the Volmer step on Pt (111), a well-defined and experimentally relevant system. We aim to shed light on how alkali cation type modulates redox kinetics for HOR/HER. To that end, we use molecular dynamics to simulate the electronically adiabatic Volmer step reaction in aqueous NaCl and CsCl electrolytes.

Due to the difficulty of probing electrolyte effects in the EDL experimentally, computational efforts have been utilized to clarify how cations affect heterogeneous ET atomistically^{32, 34, 39}. Because solvent reorganization is an essential determinant of electron transfer activation barriers, sampling nonequilibrium solvation polarization is required to understand the mechanism of EDL kinetic effects. Here, we construct a

composite model which incorporates proton-metal electronic coupling, solvent reorganization, and constant voltage electrodes. To model the heterogeneous electron transfer event, we use an embedded Anderson-Newns Hamiltonian (ANH) approach. A simple electronic coupling approximation is embedded into a classical molecular dynamics model of the electrochemical interface²². With this approach, we use importance sampling to collect statistics of redox events in HOR/HER along two reaction coordinates: the vertical energy gap coordinate and the distance of the hydrogen ion from the surface.

We show the HOR/HER solvent reorganization energy at a fixed proton distance from the surface is affected by the type of cations present in the EDL. Notably, changes in the solvent reorganization energy significantly depend on the how far redox hydrogen is from the surface due to the large spatial heterogeneity of the interfacial electrolyte species. When H^+/H is at $z = 2 \text{ \AA}$, solvent reorganization energy increases by 0.21 eV in CsCl relative to NaCl, whereas at $z = 3 \text{ \AA}$, it is 0.18 eV lower in CsCl. Unexpectedly, the supporting electrolyte ion translation contributes significantly to changes in the reorganization energy. Cs^+ in the Outer Helmholtz Layer (OHL) proximally exists much closer to adsorbed hydrogen in its neutral, reduced state compared to the proton state, raising the solvent reorganization energy at the Volmer transition state. However, we find the changes in reorganization energy are not the only factor which determine cation-dependent kinetics due to coupling between the reaction coordinates. To explain the large cation-dependence of HER rates, we show how the high surface density of Cs^+ results in a decrease in the entropy of the proton as it approaches the OHL, thereby raising the free energy of the Volmer transition state.

4.2 Results

4.2.1 Z Distributions of Ionic Species

To understand how electrolyte ions affect the interfacial solvent network and the Volmer step, we first examine the location and concentration of ions in the interfacial region. In Figure 4.1, we present the z distributions of electrolyte species in the capacitor simulation cell for two solutions: 1 M CsCl and 1 M NaCl. The z dimension corresponds to the distance normal to the electrode surface. There is considerable variation in the distributions depending on cation type. We observe narrow peaks in the electrolyte ion distributions with respect to distance from the surface as ions find favorable places to fit in the water network. Cs^+ density peaks sharply at $z = 3 \text{ \AA}$ (the OHL) and 5.3 \AA , whereas Na^+ peaks sharply around $z = 3 \text{ \AA}$, 4.5 \AA , and 7 \AA , depending on the electrode potential. Our results are qualitatively similar to data from Huang et al⁴⁸, where the large Cs^+ cation electrostatically adsorbs more readily than the smaller Na^+ ion due to weaker retention of the Cs^+ solvation shell. In the present work, we use the force field of Siepmann and Sprik to model Pt-water interactions, which was parametrized to accurately reproduce the water adsorption energy and ordered water network on the Pt surface⁸⁶. In the double layer, waters are strongly hydrogen bonded parallel to the electrode plane⁶³. Moreover, the interfacial water structure displays significant spatial heterogeneity – the density of water varies sharply as a function of distance from the Pt surface as shown in Figure A.3. Importantly, the distribution of ions in the EDL are sensitive to the local water structure.

When an ion approaches the surface, the ordered interfacial water must accommodate the ion and its solvation shell. Consequently, the free energy of an ion displays significant spatial heterogeneity depending on how well the ion is stabilized by the solvent within the structured water network at the interface. For example, in Figure 4.1A, calculating the potential of mean force (PMF) from the Cs^+ z distribution yields a Cs^+ free energy of -0.09eV at $z = 3\text{\AA}$ relative to the bulk when the electrode is at the PZC. When the electrode is 1 V below the PZC, the Cs^+ electrostatic adsorption becomes more favorable, and adsorption energy is -0.11eV . On the other hand, the Cl^- distribution peak around $z = 5.3\text{\AA}$ in Figure 4.1B is mostly unaffected by the electrode electrostatic potential. The Cl^- PMF yields a free energy of -0.08eV at the density peak. As we will show, the heterogeneous distribution of electrolyte ions significantly influences the electrostatic potential and entropy of redox hydrogen.

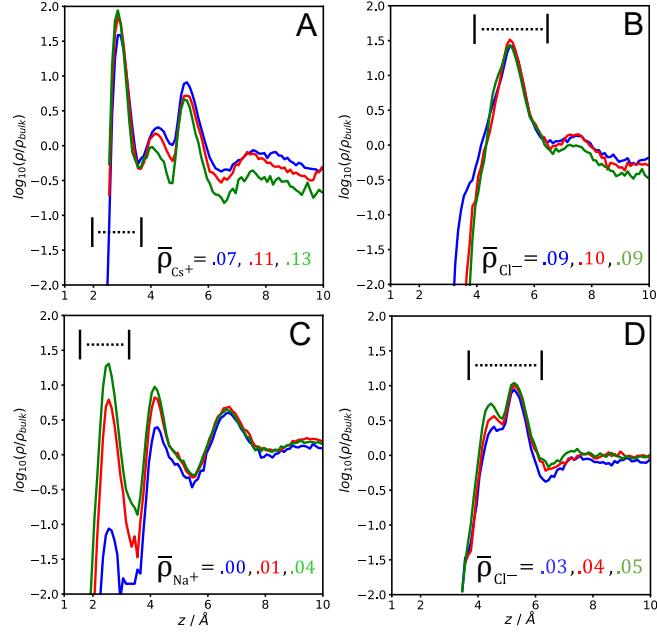


Figure 4.1. Z distribution functions for supporting electrolyte species above the Pt (111) surface. A) Cs^+ in 1M CsCl, B) Cl^- in 1M CsCl, C) Na^+ in 1M NaCl, D) Cl^- in 1M NaCl. The coverages shown in A and C are obtained by integration of the first peak of the ZDF. Colors are $V - V_{\text{pzc}} = 0 \text{ V}$, -1 V , -2 V in blue, red, and green, respectively. In this case, the distributions are obtained when no redox hydrogen is in the system to enable a larger timestep ($\Delta t = 2\text{fs}$, 20ns sampling) and to show how the electrolyte ions spatially arrange before H^+ approaches the surface.

To provide a sense of how much space is occupied by electrolyte ions and ion solvation shells in the double layer, we quantify the number of electrolyte ions in each region of the interfacial layer. By integrating the peaks in the z distribution function, we estimate the planar density of ions corresponding to different z regions in the cell:

$$\bar{\rho}_i(z_0, z_1) = \frac{L_x L_y}{N_{\text{Pt}}} \int_{z_0}^{z_1} \rho_i(z) dz$$

Where L_x and L_y are the box lengths parallel to the surface, ρ_i is the ion number density of species i , and N_{Pt} is the number of surface Pt atoms in the simulation cell. Z_0 and z_1 are chosen as the minima on either side of distribution peaks in ρ_i . The

planar densities obtained from the z distributions are normalized to the number of surface Pt atoms to provide values analogous to fractional coverages. Density values obtained from this procedure are useful to gauge the average composition in different regions of the EDL.

In Figure 4.1, the labeled integrated peaks and corresponding planar densities are shown. Figure 4.1A shows the Cs^+ surface density is quite high at $1/14 ML$ when the electrode is at the potential of zero charge (PZC). At $V - V_{pzc} = -0.5 V$, the surface density increases to $1/9 ML$. Decreasing the electrode potential further has a smaller effect on the surface density; the EDL near the surface likely becomes saturated with Cs^+ at negative potentials because Cs^+ remains solvated and competes for space with other nearby Cs^+ . The average interatomic spacing of Cs^+ at the surface is about $r = 5 - 6 \text{ \AA}$, comparable to the diameter of the first solvation shell, see Figure B.1. Moreover, the high density of Cs^+ at $z = 3 \text{ \AA}$ implies that most of the EDL waters are involved in the solvation of Cs^+ . Conversely, Figure 4.1C shows that Na^+ electrostatic adsorption is unfavorable at the PZC. While Na^+ adsorption does become increasingly favorable as the electrode potential becomes more negative, even at $V - V_{pzc} = -1 V$, the surface concentration of Na^+ is less than a third of the Cs^+ concentration under the same conditions. Thus, a much lower percentage of EDL waters participate in Na^+ solvation as compared to Cs^+ solvation.

Increased cation density at the surface induces an accumulation of Cl^- in the double layer above the surface, as expected based on classical double layer charging theory. The high OHL concentration of Cs^+ attracts Cl^- to the double layer, depicted in Figures 4.1B and 4.1D. Unlike Cs^+ or Na^+ , Cl^- does not electrostatically adsorb and

localizes in the double layer around $z = 5.3 \text{ \AA}$, which we label as the start of the diffuse layer. The planar density of the diffuse layer Cl^- distribution peak in 1M CsCl is approximately 1/11 at the PZC. In 1M of NaCl, the planar density of diffuse layer Cl^- is considerably lower at 1/30. In both solutions, the concentration of Cl^- in the diffuse layer is less sensitive to electrode potential than cations due to screening of the charged surface. As we discuss later, the Cl^- concentration in the diffuse layer region affects the local electrostatic potential of redox hydrogen. Since H^+ traverses the EDL in HOR and HER, nearby cations and anions are expected to modulate the local electrochemical potential of H^+ .

In this work, we acknowledge the lack of consideration for the chemisorption and discharge of the supporting electrolyte ion species on the surface. Only electrostatic adsorption is possible in the present model. The only species that chemisorbs is redox hydrogen, which is investigated in subsequent sections.

4.2.2 Cylindrical Pair Correlations

While pair correlation functions provide clues about the spatial dependence of proton / supporting electrolyte interactions, radial distributions do not capture the broken symmetry caused by the presence of the electrode surface. To provide a more granular view of the double layer structure and ion-ion interactions, we calculated the cylindrical pair correlation functions between atoms as follows:

$$g_{ij}(r_{\parallel}, r_z) = \frac{\langle \rho_{ij}(r_{\parallel}, r_z) \rangle}{\rho_{bulk}} = \frac{\langle \Delta n_{ij}(r_{\parallel}, r_z) \rangle}{\Delta V \rho_{bulk}}$$

Where g_{ij} are pair correlations between species i and j , $r_{\parallel} = \sqrt{r_x^2 + r_y^2}$ is the ij separation parallel to the surface, and r_z is the ij separation in the direction normal to the surface. We assume symmetry over the cylindrical solid angle. For the ensemble

averaging of ρ_{ij} , binning of counts is performed over the r_{\parallel} and r_z dimensions, and each volume slice is calculated as $\Delta V = 2\pi r_{\parallel} \Delta r_{\parallel} \Delta r_z$. ρ_{bulk} is the nominal bulk number density of the ions, $6.07 * 10^{-4} \text{ \AA}^{-3}$ for Cs^+ , Na^+ , and Cl^- in 1 M solutions. Here, we simulate 1 M NaCl and 1M CsCl solutions containing a single H^+ ion which is placed at a fixed z distance. Cylindrical pair correlations between H^+ and supporting electrolyte ions in the NaCl and CsCl systems are shown in Figure 4.2. Decomposition of pair correlations onto r_{\parallel} and r_z clearly illustrates the strong spatial heterogeneity of ion distributions in the double layer as well as the ionic response to the presence of H^+ in the interfacial layer.

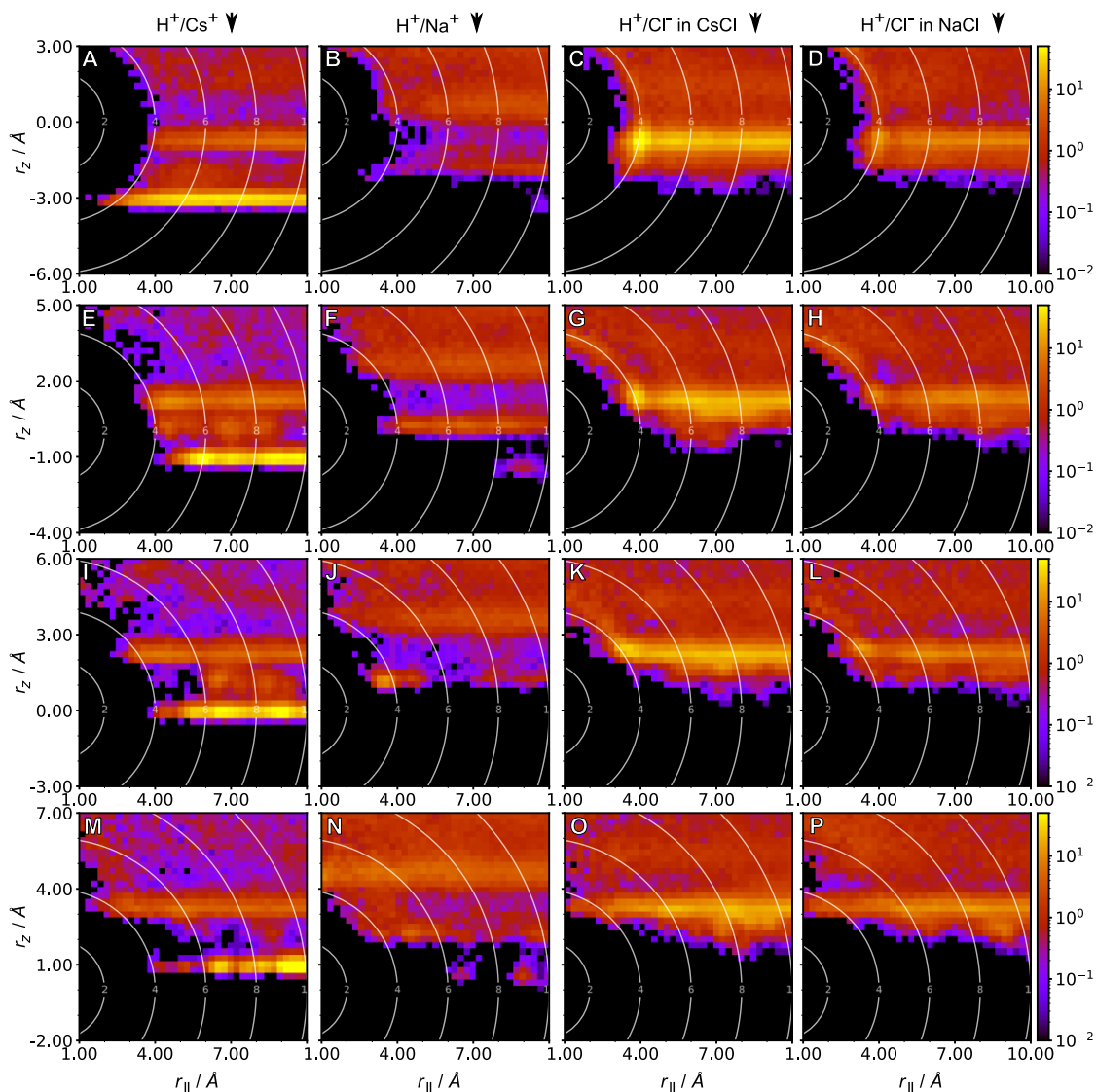


Figure 4.2. Cylindrical pair correlation functions $\rho_{ij}/\rho_{\text{bulk}}$ between the H^+ ion and supporting electrolyte ions in CsCl and in NaCl. The single H^+ ion is placed at fixed z in the cell in each case. A-D) $z = 6 \text{ \AA}$ for H^+ , E-H) $z = 4 \text{ \AA}$, I-L) $z = 3 \text{ \AA}$, M-P) $z = 2 \text{ \AA}$. From left to right, the columns correspond to H^+/Cs^+ , H^+/Na^+ , H^+/Cl^- in CsCl, and H^+/Cl^- in NaCl. Gray curves on the plot correspond to radial distance isolines $r = (r_{\parallel}^2 + r_z^2)^{1/2}$.

In CsCl, double layer Cs^+ and Cl^- significantly rearrange as H^+ traverses the EDL. In NaCl, most Na^+ remain in the diffuse layer near Cl^- , and the interfacial

density of both ions are lower than in the CsCl case. Consequently, supporting electrolyte ion rearrangement is less evident in NaCl. In Figures 4.2A, 4.2E, 4.2I, and 4.2M, OHL Cs^+ increasingly migrates away from H^+ as H^+ approaches the surface due to Coulomb repulsion and likely also due to unfavorable solvation shell interactions. In Figures 4.2C and 4.2D, we observe a significant density increase of Cl^- near H^+ in both solutions at separations of around $r = 4 \text{ \AA}$. Therefore, Cl^- localizing around $z = 5 \text{ \AA}$ displays electrostatic ion pairing with nearby H^+ . However, in Figure 4.2D, H^+/Cl^- ion pairing in NaCl is smaller in magnitude compared to CsCl. In both systems, the H^+/Cl^- ion pairing increasingly diminishes as H^+ approaches the surface since it is unfavorable for Cl^- to follow H^+ to the surface. However, the stronger H^+/Cl^- ion pairing in CsCl in the diffuse layer implies a greater *loss* of ion pairing as H^+ approaches the surface as compared to NaCl.

More generally, we expect that when H^+ migrates through the EDL, the accompanying rearrangement of electrolyte ions and solvent will affect the free energy of the proton. Solvation shells consisting of waters oriented around a cation adopt a preferred geometry which resists orientational polarization. This resistance to solvation shell deformation makes it unfavorable for a solvated cation to approach the solvated proton; in Figure 4.2, supporting electrolyte ions rarely approach H^+ within $r < 4 \text{ \AA}$. Beyond these unfavorable solvation shell interactions, translation of electrolyte ions accompanying proton motion is also expected to affect the local electrostatic potential of the proton due to ion-ion Coulomb interactions.

4.2.3 Contributions to the electrostatic potential of H^+ in the double layer

To investigate how the choice of electrolyte may influence the energetics of H^+ migration through the EDL, we separate the component contributions to the H^+ local

electrostatic potential. Because both water and the supporting electrolyte ions rearrange around H^+ as it migrates through the EDL, we decompose the Madelung electrostatic potential of H^+ into the sum of all water contributions and into the sum of all electrolyte (water + ions) contributions, shown in Figure 4.3.

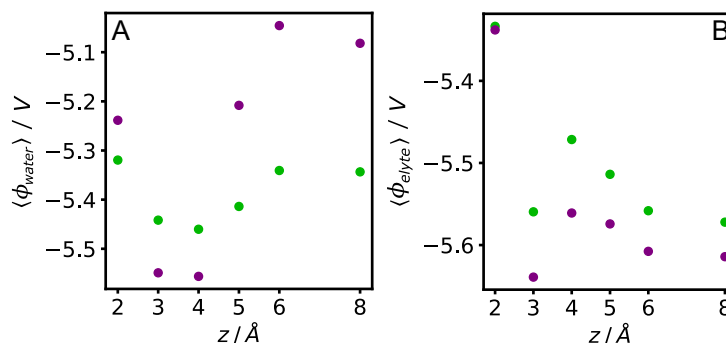


Figure 4.3. Electrostatic potential decomposition of the H^+ ion at various fixed z above the electrode surface. A) proton-water electrostatic potential, B) proton-electrolyte electrostatic potential, including the sum of both water and the supporting electrolyte ions. The CsCl and NaCl cases are shown in purple and green, respectively.

Figure 4.3A shows that H^+ solvation is weaker in the diffuse layer region at $z = 6 - 8 \text{\AA}$ in CsCl. In this region, the locally high Cs^+ and Cl^- density displaces water from the EDL and reduces the stabilization of H^+ by water. Despite weaker solvation, the H^+ total electrolyte electrostatic potential in 4.3B is more negative in the CsCl case in this region due to H^+/Cl^- ion pairing. Approaching the surface around $z = 3 - 4 \text{\AA}$, the electrostatic potential due to solvation of H^+ becomes increasingly negative in CsCl, but the overall electrolyte potential does not also decrease by the same degree. Because Cl^- is localized around $z = 5 \text{\AA}$, H^+/Cl^- ion pairing diminishes as H^+

approaches the surface, however, Figures 4.3A and 4.3B indicate that stronger solvation compensates for the loss of H⁺/Cl⁻ ion pairing in CsCl.

Regardless of the z position above the surface, the local electrostatic potential of H⁺ in CsCl is more negative than in NaCl. Therefore, the sum of solvation and ion-pairing contributions to $\langle \phi_{elyte} \rangle$ are stronger throughout the EDL in CsCl. In Figure 4.3B, the trends in local potential as H⁺ traverses the EDL are similar in the two cases. Therefore, despite the charge separation layer set up by electrostatically adsorbed Cs⁺ and diffuse layer Cl⁻, Figure 4.3 indicates that cation-dependent changes in H⁺ electrostatic potential do not directly influence how easily H⁺ migrates from the bulk to the surface. These trends provide clues about the energetics and rearrangement of the electrolyte which are relevant to the Volmer step kinetics.

4.2.4 Diabatic Electron Transfer Analysis

To understand the interplay between solvent reorganization energy, redox free energy, and supporting ion effects, we calculate the free energies along the solvent collective coordinate corresponding to the diabatic reaction $H \leftrightarrow H^+ + e^-$ for a single redox hydrogen in 1M NaCl and in 1M CsCl. The solvent fluctuations are tracked using the vertical energy gap collective variable, denoted ΔE . The vertical energy gap is modeled by the difference in potential energy between the redox ion's reduced and oxidized states at a fixed nuclear configuration:

$$\Delta E(\mathbf{R}) = V^{red}(\mathbf{R}) - V^{ox}(\mathbf{R})$$

Where \mathbf{R} is the set of all nuclear coordinates of the system at a given time and V^{red} , V^{ox} are the energies of the reduced and oxidized states given by the sum of interaction potential contributions. To be clear, ΔE includes the interaction potential contributions from the solvent, supporting electrolyte ions, and fluctuating charges on the constant-

voltage electrodes. We perform importance sampling along the vertical gap coordinate and obtain unbiased free energies using standard umbrella sampling and weighted histogram analysis⁹⁰. The free energy curves can be defined up to a constant and satisfy the relation²²:

$$F^H(\Delta E) = F^{H^+}(\Delta E) + \Delta E$$

Where F^H and F^{H^+} are the free energies of the reduced H and H^+ states, respectively.

We use ΔE to denote the random variable for the vertical energy gap and Δe to denote specific values of ΔE . For the fixed z calculations, the reduction ΔF is defined by:

$$\Delta F = F^H(\Delta e_{min}^H) - F^{H^+}(\Delta e_{min}^{H^+})$$

Where Δe_{min}^H is location of the free energy minimum in the reduced state and $\Delta e_{min}^{H^+}$ is the location of the minimum in the proton state, i.e. equilibrium solvation, illustrated in Figure 4.4A. The expression for ΔF does not include the contribution due to ET to the metal, which shifts ΔF by a constant related to the overpotential.

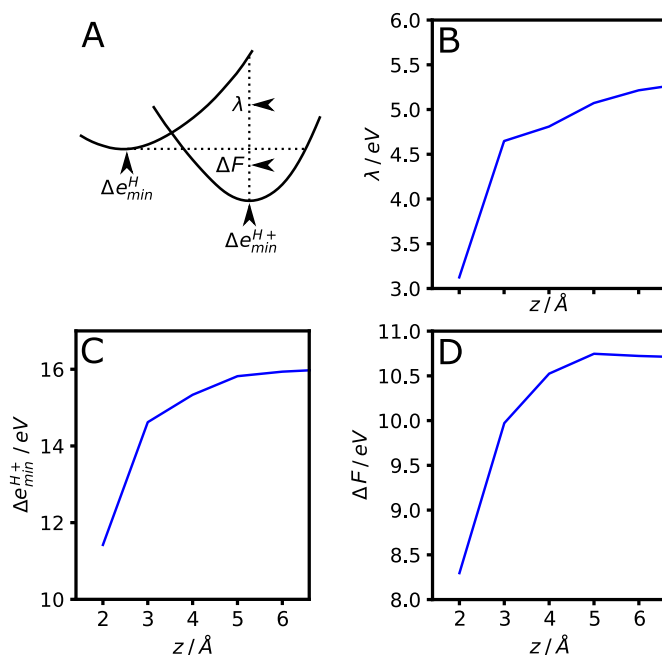


Figure 4.4. Diabatic free energy analysis for H^+/H redox at fixed z in 1M CsCl. A) Schematic showing how λ , Δe_{min} , and ΔF are calculated from the simulated free energies. Values for B-D are for 1M CsCl. B) Solvent reorganization energy, λ , C) equilibrium ΔE value for H^+ , Δe_{min}^{H+} , D) Diabatic reduction free energy change, ΔF .

In Figure 4.4, we calculate the diabatic free energies for the proton at fixed z distances from the Pt surface for 1M CsCl. In Figures 4.4B-4.4C, H^+ loses solvation energy as it approaches the surface, shrinking the solvent reorganization energy. Figure 4.4C indicates that the vertical difference at equilibrium proton solvation shrinks closer to the surface due to weakening solvation, that is, the difference $\Delta E = V^{red} - V^{ox}$ is smaller when V^{ox} is less negative. Since H^+ is less stabilized by the solvent near the surface, reduction becomes more favorable, shown in Figure 4.4D. The diabatic free energy curves used to produce Figure 4.4 are shown in Figure B.3.

The choice of electrolyte alters H^+/H solvent reorganization energy in a spatially varying manner. In Figure 4.5, we compare the differences in the diabatic free energy curves for the 1M NaCl and 1M CsCl systems when H is at fixed z .

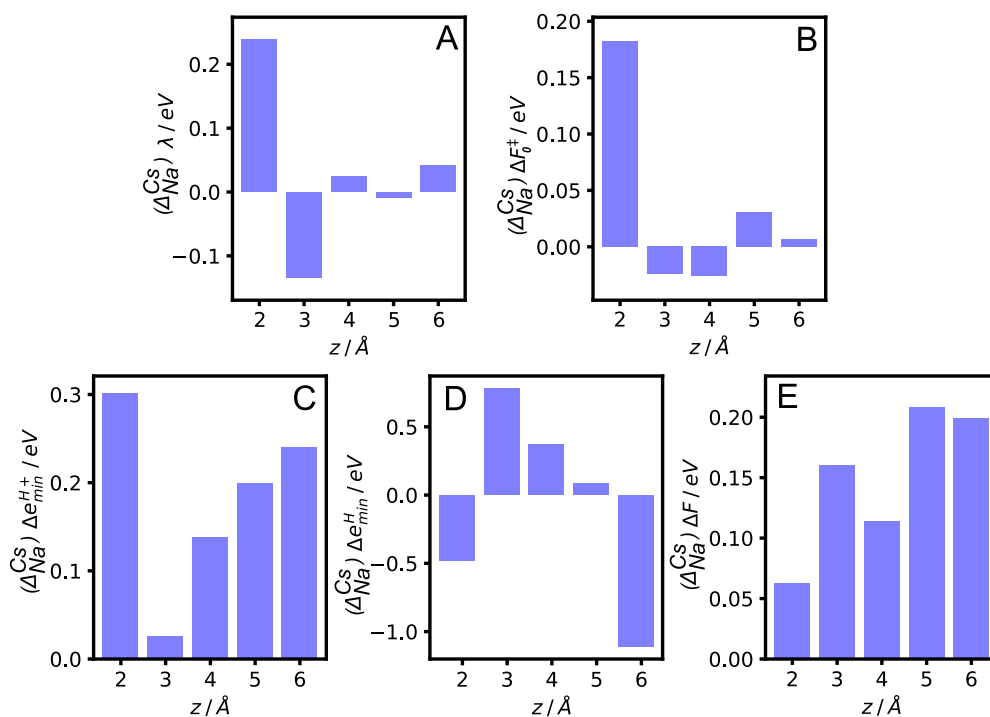


Figure 4.5. Further analysis of diabatic free energies for H^+/H redox at fixed z . Differences in values calculated for the 1M CsCl cases relative to the 1M NaCl cases (notated using Δ_{Na}^{Cs}) are shown. A) differences in λ values calculated by the vertical difference at $\Delta e^{H^+}_{min}$, B) Differences in the intrinsic barrier for diabatic crossing when $\Delta F = 0$, ΔF_0^\ddagger , C) differences in $\Delta e^{H^+}_{min}$ values, D) differences in $\Delta e^{H^+}_{min}$ values, and E) differences in H^+ reduction ΔF values.

Figure 4.5A displays statistically significant differences in the H^+/H reorganization energy and the intrinsic activation barriers between the two electrolyte systems. The variation in $\Delta_{Na}^{Cs}\lambda$ with z is a consequence of electrostatic interactions

between redox hydrogen and the electrolyte ions which display considerable spatial heterogeneity along the EDL. In CsCl, OHL Cs^+ tends to situate much closer to reduced H at $z = 2 \text{ \AA}$ as compared to H^+ due to the lack of electrostatic repulsion between Cs^+ and neutral H, see Figure B.4. When OHL Cs^+ is present, the vertical energy gap is less positive for reduced H at equilibrium near the surface (Δe_{min}^H), shown in Figure 4.5D. Essentially, the vertical gap Δe_{min}^H shrinks because the Coulomb potential between H and nearby Cs^+ would be highly positive if H was oxidized; V^{ox} is less negative. Interestingly, the mean electrolyte polarization for the reduced (Δe_{min}^H) and oxidized states ($\Delta e_{min}^{H^+}$) are *differentially impacted* by the choice of electrolyte. At $z = 2 \text{ \AA}$, H^+ at equilibrium is more stabilized by Cl^- in CsCl than in NaCl, increasing $\Delta e_{min}^{H^+}$ by making V^{ox} more negative. Because reorganization energy λ is proportional to the *difference* in equilibrium polarization between the two states, the larger $\Delta e_{min}^{H^+} - \Delta e_{min}^H$ in CsCl at $z = 2 \text{ \AA}$ results in larger reorganization energy. Critically, the translation of electrolyte ions contribute to the collective fluctuations and thus affect the reorganization energy. The translation of Cs^+ (and perhaps Cl^- to a lesser degree) along the collective coordinate incurs an energetic penalty, increasing the reorganization energy. In Figure 4.5B, the larger solvent reorganization energy at $z = 2 \text{ \AA}$ in CsCl induces a larger intrinsic redox barrier, ΔF_0^\ddagger .

At $z = 3 \text{ \AA}$, the opposite trend in reorganization energy occurs, and λ is 0.18 eV *higher* in NaCl than in CsCl (Figure 4.5A). When H is at $z = 3 \text{ \AA}$, Cl^- situates near reduced H due to weak dispersion attraction (Figure B.4), resulting in a more negative local electrostatic potential and consequently an increased vertical energy gap Δe_{min}^H , i.e., V^{ox} is more negative. The density of Cl^- near reduced H at $z = 3 \text{ \AA}$ is larger in magnitude in CsCl due to the higher concentration of excess diffuse layer Cl^- .

Consequently, the difference in polarization between the two equilibrium states, $\Delta e_{min}^{H^+} - \Delta e_{min}^H$ is smaller in CsCl and so is the reorganization energy. However, despite the significant difference in λ between the two systems, only a small change in the intrinsic barrier ΔF_0^\ddagger is seen at $z = 3 \text{ \AA}$, in contrast to the significant change in ΔF_0^\ddagger at $z = 2 \text{ \AA}$. This result is likely a consequence of the nonlinear electrolyte polarization response. Evidently, the redox intrinsic barrier ΔF_0^\ddagger is not as sensitive to the change in λ at $z = 3 \text{ \AA}$ as it is to the change in λ at $z = 2 \text{ \AA}$. While Cl^- is responsible for the change in λ at $z = 3 \text{ \AA}$, we speculate that the translation of diffuse-layer Cl^- ions is more facile as compared to the OHL Cs^+ ions, resulting in only minor changes to ΔF_0^\ddagger .

Besides changes in the reorganization energy, the redox free energy also significantly differs between 1M NaCl and 1M CsCl. In Figure 4.5E, H^+ reduction is *less favorable* in CsCl than in NaCl due to proton stabilization by H^+/Cl^- ion pairing. Moreover, despite the consistently more negative H^+ electrostatic potential throughout the EDL in CsCl (Figure 4.3), the difference in the reduction driving force between the two electrolyte systems shrinks when H^+ is closer to the surface. Thus, another factor unrelated to H^+ electrostatics *favors* H^+ reduction closer to the surface in CsCl relative to NaCl. As we will show later, decreased entropy favors reduction in CsCl when H^+ is near the surface. Clearly, there is significant coupling between electrolyte reorganization around the redox hydrogen and its distance from the surface.

Huang et al. argued that because disruption of the interfacial hydrogen bonding network varies by cation identity, cation-dependent changes in HOR/HER activation energy are due to changes in solvent reorganization energy⁴⁸. Here, we do observe a disruption of the surface water H-bond network by Cs^+ more so than Na^+ , depicted in Figure B.5. Figure B.5 shows that more surface waters have only one or two hydrogen

bonds in CsCl as compared to NaCl, in agreement with SEIRAS data which showed that CsCl has a higher fraction of “isolated waters” at the surface⁴⁸. Moreover, the increased redox solvent reorganization energy and intrinsic activation barrier when Cs⁺ is present near hydrogen at the surface is consistent with Huang’s argument that the presence of Cs⁺ increases the solvent reorganization energy.

However, we would like to emphasize the larger reorganization energy at the surface in CsCl is primarily due to direct interactions between the redox hydrogen and supporting electrolyte ions, not due to changes in water polarization. At $z = 2 \text{ \AA}$, Figure 4.3A showed that the electrostatic potential of H⁺ due to water is weaker in CsCl, which, all else equal, would imply a smaller $\Delta e_{min}^{H^+}$ and a smaller λ , contrary to what we observe in Figure 4.5. Instead, reorganization energy is larger in CsCl at $z = 2 \text{ \AA}$ due to direct ion/redox hydrogen interactions. Moreover, the trends in solvent reorganization energy vary significantly with the H⁺ z distance; free energy profiles for redox hydrogen near $z = 3 \text{ \AA}$ suggest a slightly *lower* redox intrinsic barrier in the CsCl electrolyte. The two reaction coordinates are significantly coupled. Thus, to understand the interplay between z and ΔE and uncover trends in the overall Volmer activation barriers, we next analyze the free energy surfaces $F(z, \Delta E)$.

4.2.5 Adiabatic Free Energy Surfaces

Next, we show how the choice of electrolyte affects the Volmer free energy surface. We simulate the electronically adiabatic charge transfer between a single proton and the electrode in the limit of low coverage. The embedded ANH term describes the switching between the reduced and oxidized states as a function of the ion-metal electronic coupling and the vertical gap coordinate, ΔE . An additional H-surface Morse bond term is added to the reduced state interaction potential to bind H*

to the Pt surface. To obtain free energy surfaces, we perform importance sampling along the two relevant reaction coordinates, z and ΔE .

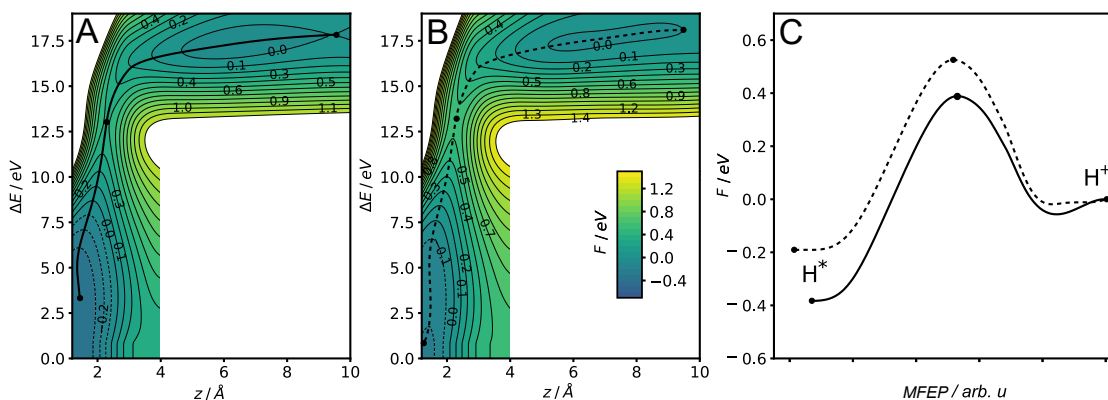


Figure 4.6. Adiabatic free energy surfaces for H^+/H redox with 1 M CsCl and 1 M NaCl electrolytes. A) 1 M CsCl, B) 1 M NaCl, C) minimum free energy pathways for the CsCl case (solid) and the NaCl case (dashed). For the electronic model, the Fermi level is set such that $\epsilon_a - \epsilon_f = -12.14$ eV. The cell electrostatic potential is set to $V - V_{pzc} = 0$ V.

In Figure 4.6, the Volmer oxidation barrier is 0.04eV smaller in CsCl due to the presence of OHL Cs^+ which weakens HBE. However, given the magnitude of the observed change in HBE, a much larger decrease in Volmer oxidation barrier was expected. However, solvent reorganization energy is larger in the CsCl case vs. the NaCl case. For the adiabatic hydrogen oxidation, most of the collective reorganization on the MFEP leading up to the transition state occurs around $z = 2\text{\AA}$ where the reorganization energy was shown to be larger in the CsCl case. The larger reorganization energy in the CsCl system is consistent with the smaller Δe value for reduced H at equilibrium, matching up with Figure 4.5D. Based on our findings shown in Figure 4.5, H^*/Cs^+ separation must increase by translation of either species for

oxidation to occur. To summarize, a larger magnitude of electrolyte reorganization is necessary to drive the oxidation in the CsCl case, and the collective reorganization includes Cs^+ translation in addition to water rearrangement. Therefore, translation of the electrolyte species relative to H^*/H^+ play an important role in cation-dependent HOR and HER kinetics.

In Figure 4.6, we similarly show that the reduction Volmer activation energy in Cs^+ -containing electrolyte is 0.18eV larger versus the Na^+ -containing electrolyte, consistent with experimental trends in HOR/HER activity versus cation size^{48,91}. In CsCl, Figure 4.6A shows that the minimum free energy pathway (MFEP) rises quicker as H^+ approaches the transition state with a larger concomitant decrease in Δe . The largest differences between the two cases are most evident in the region of $z = 2 - 4\text{\AA}$. Just before the reduction transition state, the higher proton free energy in CsCl shifts the transition state earlier along the reaction coordinate, in accordance with Marcus-Hush theory.

As explored earlier, Cs^+ is abundant in the EDL around $z = 3\text{\AA}$, and a much higher fraction of interfacial waters participate in Cs^+ solvation compared to interfacial waters in the NaCl case. Because the overlap of the solvation shells of like-charged ions is unfavorable, H^+ solvation is expected to be frustrated by Cs^+ as it approaches the surface, increasing the free energy of the proton near the surface and the Volmer activation barrier. Unexpectedly, Figure 4.3A showed that the water contribution to the H^+ electrostatic potential at $z = 3 - 4\text{\AA}$ is about 0.1eV more negative in CsCl vs. NaCl, implying stronger rather than weaker solvation. To resolve this apparent discrepancy, we analyze the entropic contribution to the Volmer surface in the next section.

4.2.6 Entropic contributions to H⁺ free energies in the EDL

While the presence of OHL Cs⁺ certainly increases the Volmer activation barrier, weaker H⁺ solvation is unlikely to be the cause. We noted earlier that entropic effects related to proton translation through the EDL are important. Specifically, the presence of OHL ions can effectively increase the degree of structural ordering near H⁺ and restrict its motion. Thus, to isolate the entropic contributions to the redox activation barriers, we estimate the entropy along the Volmer reaction coordinates from the free energy surface and potential energy surface:

$$-T\langle S\rangle(\Delta E, z) = \langle F\rangle(\Delta E, z) - \langle U\rangle(\Delta E, z)$$

Where $\langle U\rangle$ is the total system internal energy. Like in the free energy calculations, statistics for $\langle U\rangle$ are collected using umbrella sampling and debiased using standard WHAM. Figure 4.7 shows the entropic contribution to the free energy surfaces, $-T\langle S\rangle$, as a function of the collective coordinate and distance of redox H from the surface.

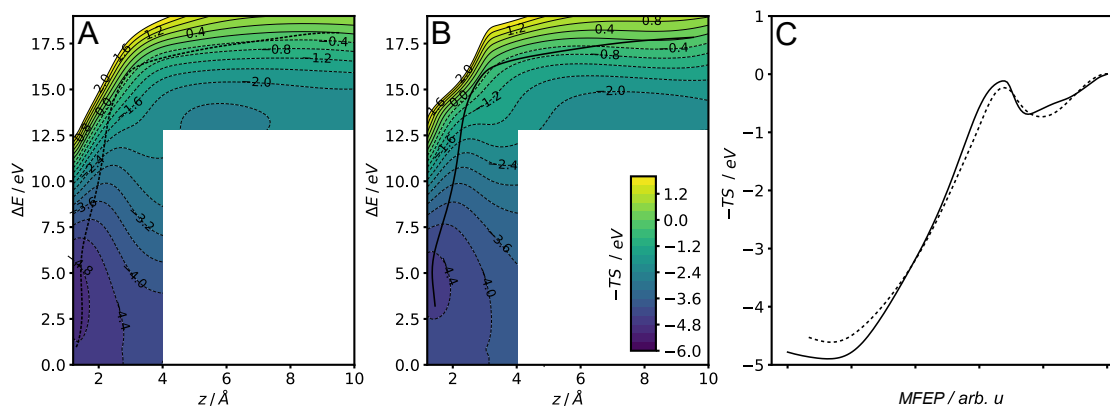


Figure 4.7. Entropy contribution to the free energy of adiabatic ET in the Volmer step. Entropy is calculated as a function of the collective coordinate ΔE and the redox hydrogen distance from the surface, z , at 300K. A) $-T\langle S \rangle$ for H⁺/H redox in 1M CsCl, B) $-T\langle S \rangle$ for H⁺/H redox in 1M NaCl, C) entropy contribution along the Volmer step minimum free energy pathways (MFEP) from A) and B) projected onto 1D. The dashed line is the MFEP for the NaCl system and the solid line is for the CsCl system. In A) and B), data in the white regions are omitted due to limited sampling.

Proceeding towards the reduction transition state along the MFEP, the proton entropy significantly increases due to desolvation. Interestingly, in the CsCl case, the entropy loss is not as rapid as redox H passes through the reduction transition state. Near the TS, $-T\langle S \rangle$ is 0.3eV higher in the CsCl case vs the NaCl case. The largest deviation in entropy between the two cases along the MFEP coincides with the location of OHL Cs⁺, that is, near $z = 3\text{\AA}$. Moreover, Figure 4.2 shows a large excess of Cs⁺ near H⁺ when H⁺ crosses the OHL. In the NaCl case, Na⁺ does not adsorb on the surface and thus does not “crowd out” H⁺ near the OHL. Because strong pair correlations are a direct cause of lower configurational entropy⁹², the high concentration of surface Cs⁺ lowers the entropy of H near the redox transition state, increasing Volmer activation energy.

4.3 Implications for Cation-Dependent and pH-dependent HOR/HER Kinetics

Cation-dependent interfacial water restructuring has been proposed to alter HOR/HER reorganization energy to explain kinetic trends. Huang et al. proposed that Marcus-Hush-Chidsey (MHC) kinetics apply to HOR/HER and fit changes in reorganization energy from experimental current density data⁴⁸. However, within the MHC formalism, variations in the free energy of the redox ion as it moves normal to the surface are not explicitly accounted for, as these variations are absorbed implicitly into the solvent reorganization energy term. Moreover, the vertical energy gap coordinate and redox ion z coordinate are significantly coupled. In addition to solvent reorganization energy, the activation energy for heterogeneous ET is dependent on the free energy to bring the reactants to the surface^{44, 45, 93}. For example, the z -dependence of ion free energy is the essence of the Frumkin correction, where negative electrode surface charge repels anions from the surface and causes sluggish oxidation kinetics⁴⁴. To reconcile these perspectives, more studies which incorporate both solvent reorganization and ion migration through the EDL are needed to clarify the interplay between redox kinetics and EDL features such as electrolyte composition, solvent structure, and surface charge^{41, 45, 93}.

Cs^+/H^+ EDL interactions can be considered in a similar way to lateral interactions between adsorbates which depend sensitively on interatomic separation. Even when the Pt (111) surface is uncharged, our data show that Cs^+ electrostatically adsorbs with 1/11ML coverage. Moreover, electrostatically adsorbed cations repel each other and tend to maximize distance from each other. As a result, there are few surface sites where H^+/H can easily adsorb/desorb far from Cs^+ atoms. In Huang et al, supplementary cyclic voltammetry data on Pt(pc) surfaces showed significant suppression of hydrogen underpotential deposition (H_{upd}) corresponding to current

peaks attributed to Pt (100) and Pt (110) sites⁴⁸. H_{upd} peak suppression increased in order of increasing cation size and is likely caused by cation adsorption. Since the Volmer step is inhibited by OHL Cs^+ , we speculate that large alkali cations adsorbed on Pt (100) and Pt (110) sites significantly raise the Volmer activation barrier both at and adjacent to those sites. On polycrystalline Pt surfaces, Pt (100) and Pt (110) sites are more active for HOR and HER than Pt (111). Therefore, larger solvent reorganization energy and lower proton entropy near Pt (100) and Pt (110) sites may account for a large part of the considerable decrease in Pt (pc) HOR/HER activity in electrolytes containing large cations.

The role of activation entropy has been proposed to be relevant for both cation type-dependent HOR/HER kinetics as well as pH-dependent HOR/HER kinetics. It is intriguing that our simulation results support the argument by Huang et al. that the presence of large cations at the interface increase the entropic barrier for HOR/HER. Similarly, the apparent link between cation type and proton entropy is in the same spirit as the hypothesis put forward by Rossmeisl et al⁹⁴. The authors proposed that, when comparing high pH and low pH, larger Volmer activations barriers in alkaline are caused by a larger entropy loss as H^+ approaches the surface⁹⁴. H^+ in solution has a higher entropy at higher pH, but the entropy of H^* stays about the same, thus, the entropy loss of the proton migrating to the surface is larger in alkaline. At the same time, at high pH, electrode surface charge is more negative and the cation concentration is much higher, so a higher concentration of surface cations is expected in alkaline. While the cation-dependent trend in exchange current density occurs at both high and moderately low pH, the cation-dependence of HOR/HER activity is much higher in alkaline on Pt⁴⁸. Therefore, we suggest that entropic effects caused by

interfacial cations could be at least partially responsible for larger entropic barriers to HOR/HER redox in the high-pH environment⁹⁴.

Here, we have studied the Volmer step where the acidic proton is the hydrogen donor in NaCl and CsCl electrolytes. In the case of alkaline HOR/HER, H₂O (OH⁻) is the proton donor (acceptor). On Pt (111), it is unlikely that OH* is a stable intermediate in the HOR/HER potential region. Thus, aqueous OH⁻ participates in the alkaline mechanism. The activation energy in the alkaline mechanism is also expected to correlate with the local free energy of OH⁻. Moreover, the type of counterion to the alkali ions is likely important. Here, the counterion is Cl⁻, but in alkali solutions, OH⁻ will be present in significant concentrations. We expect that the free energy of double layer OH⁻ exhibits spatial heterogeneity which is affected by cation type; the trend in OH⁻ density in the EDL may be similar to the trend observed for the Cl⁻ anion here. Depending on whether cations electrostatically adsorb or stay in the diffuse layer, entropic effects and/or ion-pairing between cations and OH⁻ may significantly modulate alkaline redox kinetics. In the future, additional research is required to model the water splitting reaction with solvent reorganization and an atomistic double layer to understand how spatial distributions of cations affect the rate of the alkaline Volmer step.

4.4 Conclusions

We have shown from molecular dynamics calculations how Volmer kinetics are slower in 1 M CsCl electrolyte compared to 1 M NaCl. The effects are mediated by two phenomena:

1. OHL Cs^+ induces an increase in H^+/H reorganization energy because Cs^+ situates near H^* more closely than H^+ , resulting in reorganization of the electrolyte ions along the collective polarization coordinate.
2. The high Cs^+ concentration near the surface decreases the entropy of the proton near the surface, increasing the Volmer activation energy.

We also observed that changing the cation identity changes the relative accumulation of counter-ions to the diffuse layer. Thus, cation identity effects on HOR/HER may also more generally depend on the counter-ion type and how counter-ions fit into the heterogeneous water network structure near the surface. For pH-dependent HOR/HER, the presence of OH^- in alkaline and the change in proton donor identity to H_2O may significantly alter the cation-dependence of the free energy surface for the Volmer step.

4.5 Computational Resources

This research used resources of the National Energy Research Scientific Computing Center (NERSC), a U.S. Department of Energy Office of Science User Facility located at Lawrence Berkeley National Laboratory, operated under Contract No. DE-AC02-05CH11231 using NERSC award m1893 for years 2021-2022.

This research was also supported in part through the use of DARWIN computing system: DARWIN – A Resource for Computational and Data-intensive Research at the University of Delaware and in the Delaware Region, University of Delaware, 2021, URL: <https://udspace.udel.edu/handle/19716/29071>

Chapter 5

FUTURE DIRECTIONS

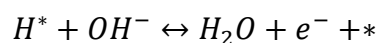
5.1 Introduction

The mechanism of pH-dependent hydrogen electrocatalysis kinetics remains an active area of research, and much evidence indicates that sluggish alkaline HOR/HER kinetics has multiple contributions related to electrode electrostatic potential, cation effects, and changes in reaction mechanism^{31, 37}. Many challenges remain in the way of a more complete understanding of HOR/HER kinetics trends as well as fundamental theoretical electrochemistry. In this work, we have developed a composite model and taken a step towards understanding interfacial electrostatics and supporting electrolyte effects in the Volmer step for HOR/HER. However, as with all models of electrocatalysis, significant simplifying assumptions are necessary to make studying EDL effects tractable. For the future, we suggest how the present approach can be adapted to study other outstanding questions in pH-dependent HOR/HER. Secondly, we suggest a potential route toward modeling constant-voltage electrodes with greater quantitative accuracy within a classical MD approach.

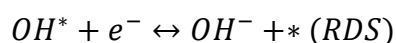
5.2 The role of hydroxide in alkaline hydrogen electrocatalysis

One important contribution to alkaline electrocatalysis kinetics that we have not studied is the role of hydroxide. In the present work, we have studied the Volmer step at the water / platinum interface without the presence of hydroxide. However, as briefly discussed in earlier chapters, double layer and/or adsorbed hydroxide likely

participate in the alkaline HOR/HER mechanism. In alkaline where the HOR/HER onset potential is much more negative, it is unlikely that H_2O abstracts H^* from the surface- as it does in acid- due to the higher potential bias towards the reduced H^* state. Instead, OH^- or OH^* must abstract H^* from the surface, which is more thermodynamically favorable. As a reminder, the alkaline Volmer step can be written as:



where $*$ denotes a catalyst surface site. When the binding of OH^* to the surface is strong, several lines of reasoning indicate that the alkaline HOR/HER mechanism proceeds through a bifunctional mechanism:

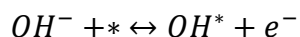


In this case, a strongly oxophilic catalyst promotes facile water dissociation/reassociation on the surface, accelerating HOR/HER kinetics^{35, 39, 40, 95, 96}. However, the effect of catalyst electrostatic potential and the presence of interfacial cations alters the energy of interfacial OH^* and OH^- , complicating the kinetic trends in these proposed alkaline mechanisms^{31, 37}. Thus, further investigations are necessary to clearly map out the interconnected factors in pH-dependent HOR/HER kinetics.

To provide deeper mechanistic insights into the interplay between alkaline HOR/HER kinetics and interfacial properties such as electrode electrostatic potential and supporting electrolyte effects, there is a need to develop a framework to study hydroxide adsorption in simulations including the explicit EDL. While DFT studies have generated mechanistic insights into the relationship between hydroxide binding energies and the alkaline Volmer mechanism^{39, 40}, EDL effects in alkaline HOR/HER

remain poorly understood. For example, Jia et al showed that increasing the concentration of alkali cations selectively promotes HER kinetics on Pt/C, PtNi/C, and Ni/C; however, changing the cation identity affects both HOR and HER kinetics³⁷. The reasons for this discrepancy are unclear. To give a second example, on some catalyst facets such as Pt (111), experimental evidence indicates that hydroxide does not adsorb²⁸, but interfacial OH⁻ is still a product/reactant for HER/HOR respectively. Therefore, the energy of interfacial OH⁻ is expected to correlate with reaction kinetics⁴⁰. The electrode electrostatic potential has been proposed to affect how favorable it is for OH⁻ to access the double layer³⁷; more negative electrode surfaces are thought to repel OH⁻ and slow HOR/HER kinetics. To our knowledge, theoretical studies have not been performed to quantify how cations or interfacial electrostatic potential affect the stability of aqueous OH⁻ situated in the EDL.

We suggest that, in the future, embedded-ANH molecular dynamics models for the hydroxide adsorption reaction will be useful to evaluate the nature of cation and interfacial electrostatic potential effects on alkaline HOR and HER. This reaction is written as follows:



As we have argued, molecular simulations of EDL effects in HOR and HER should incorporate the atomistic EDL structure, solvent reorganization, and constant potential electrodes. Statistics of EDL fluctuations at the heterogeneous interface tend to converge slowly, hence the necessity for embedded redox models within classical molecular dynamics as a complement to other ab-initio based techniques. First, controllable electrode potential is necessary to elucidate how OH* adsorption kinetics depend on EDL electrostatics, which is key to understanding OH⁻ transport to the

surface. Thus, we propose that the potential-dependent adsorption of OH* should be studied in the embedded-ANH framework. Second, spatial heterogeneity of interfacial water structure and supporting electrolyte ions create significant spatial variation in the free energy of EDL ionic species as well as adsorbates. To clarify how EDL cations affect OH* adsorption kinetics, we propose that alkali cation-dependent adsorption of OH* should be studied in the embedded-ANH framework as well. Specifically, these works should aim to compute the adiabatic free energy surfaces as well as the solvent reorganization energy for OH* adsorption. Overall, these proposed studies are expected to provide a granular perspective of OH* and OH⁻ / electrolyte interactions and clarify how EDL properties affect OH binding energies and adsorption activation barriers.

5.3 Opportunities for improved constant voltage techniques

Modeling the electrified interface in classical molecular dynamics is a difficult task because of the dual challenge of maintaining constant potential at the surface and accurately modeling the spatial distribution of electron charge density. At the electrode surface, the electron density decays gradually and spills over into the electrolyte, forming a surface dipole⁹⁷. The electronic spillover has significant effects on the work function, local potential at the surface, and the adsorption energy of surface species⁹⁷⁻⁹⁹. However, in the present work, we employed a classical molecular dynamics technique to sample the statistics of solvent reorganization and the dynamics of the electrochemical interface. In the classical MD simulations performed here, we make the simplification of using point charges. In the future, progress is needed to model the electrified interface in classical MD simulation with greater accuracy to improve the quantitative and qualitative agreement with quantum chemical simulation

techniques. In this section, I briefly summarize the constant electrode potential algorithm used in this work and suggest a possible modification for use in future work.

One of the simplest techniques to model the constant-voltage electrode is the method of images¹⁰⁰. In classical electrostatics, the induced polarization of a grounded planar conductor can be modeled using the classical method of images. For every point charge q with position d above a planar conductor, placing a virtual point charge $-q$ at position $-d$ below the planar surface solves the constant-potential boundary value problem. The method of images simplifies the spatially inhomogeneous charge density of the atomic electrode surface to a classical planar conductor. The classical image approximation captures the qualitative behavior of the induced charging for the dense and well-defined (111) crystal facet, but fails for atomically corrugated facets.

Within the method of images approximation, the placement of the image plane can be treated as an adjustable parameter. Specifically, Schmickler et al. has argued that, to treat short range electrostatics more accurately for electrochemical simulation, the position of the image plane must be chosen carefully and in correspondence with the centroid of polarization charge density as calculated from DFT^{101, 102}. Essentially, because of the inhomogeneous charge distribution at the surface of metals, the placement of the effective image plane should reflect the approximate position where charge accumulates when the metal is polarized. At the interface between the solution and transition metals, the image plane is ideally not placed at the center of the surface atoms but rather further towards the solution side. For example, for Ag (111), the effective image plane has been calculated to be about 1.4 Å above the atomic centers of the surface atoms, about half the interplanar spacing of the electrode atoms⁹⁷. Placing the image plane at the fitted, effective position greatly affects the short-range

image attraction potential. Consider two cases where the image plane is placed either coplanar with the center of the surface atoms or 1.4Å above the center, i.e. $z_{im} = 0\text{Å}$ or $z_{im} = 1.4\text{Å}$. If a singly charged ion is 3Å from the electrode surface, the image potential will differ by 1eV between the two cases, a huge difference. Moreover, fitting the image plane distance greatly improves the agreement between experiment and theory for double layer capacitance, implying greater accuracy in modeling the induced surface charge density^{101, 102}.

However, even after fitting the image plane position, the classical method of images approach is not without flaws. While the classical image potential is an accurate model of the surface polarization induced by charged atoms in the long range, it becomes an increasingly poor approximation at very small ion / electrode separations. Choosing the image plane position based on the centroid of charge polarization presents another issue for molecular simulation: for charged species which adsorb on the surface and cross the effective image plane position, the z^{-1} image potential unphysically diverges. In the case of hydrogen adsorption on Pt (111), the image plane should ideally be placed around $z_{im} = 1.5\text{Å}$, but H* adsorbs at $z = 1.0\text{--}1.5\text{Å}$. The singularity is an artifact of treating the adsorbates as point charges and the surface as an ideal plane. In reality, the spatial electron density distributions of adsorbates and surface electrode atoms have some width, and these electron densities significantly overlap at short range.

Here I propose a simple method to circumvent the singularity in the short-range image potential for molecular dynamics simulations. Essentially, the goal is to reproduce the correct long-range image potential behavior but fit the short-range interaction energies empirically based on quantum chemical calculations. Here, I

suggest using a functional form originally recommended by Chulkov et al¹⁰³. Chulkov et al. previously used semi-empirical equations to fit the potential of electronic image states at the surface of transition metals¹⁰³. The classical image potential is modified to be attenuated very close to the surface, with the following expression in atomic units:

$$V_{im} = (\exp(-\gamma(z - z_{im})) - 1) * \frac{1}{4(z - z_{im})}$$

Where z_{im} is the effective image plane position and λ is an empirical screening parameter. The Chulkov potential recovers the correct image potential at long range and behaves as an empirical interaction potential in the short range. The physical justification for the exponential term is the repulsion between the charge density of an electron close to the surface and the core electrons of the metal surface, which attenuates the image attraction. While Chulkov's approach was used to calculate the energy of electronic image states, similar physical phenomena are involved for ionic species approaching the metal surface. Electron-electron repulsion becomes dominant as the electron density of an ion close to the surface increasingly overlaps with the surface electron density of the metal. To fit the parameter γ , modern constrained density functional theory (CDFT) techniques can be used to compute the potential energy of atoms constrained to their ionic state close to metal surfaces¹⁰⁴. Additionally, with this approach, the image plane position can be fit based on the induced charge density centroid calculated using DFT as recommended by Schmickler¹⁰⁵. By fitting γ and the image plane position, the magnitude of short-range electrostatic attraction between EDL ions and electrode surfaces could be represented more accurately without introducing unphysical divergences in the potential.

REFERENCES

- [1] Bockris, J. O. M. The hydrogen economy: Its history. *International Journal of Hydrogen Energy* **2013**, 38 (6), 2579-2588. DOI: 10.1016/j.ijhydene.2012.12.026.
- [2] Arias, P. A., N. Bellouin, E. Coppola, et al. 2021: Technical Summary. In *Climate Change 2021: The Physical Science Basis. Working Group I Contribution to the IPCC Sixth Assessment Report*, 2021.
- [3] Wallace-Wells, D. *The Uninhabitable Earth*; Tim Duggan Books, 2019.
- [4] Pörtner, H.-O., D.C. Roberts, H. Adams, et al. 2022: Technical Summary. In *Climate Change 2022: Impacts, Adaptation and Vulnerability*, Cambridge University Press, Cambridge, UK and New York, NY, USA, 2022.
- [5] Way, R.; Ives, M. C.; Mealy, P.; Farmer, J. D. Empirically grounded technology forecasts and the energy transition. *Joule* **2022**, 6 (9), 2057-2082. DOI: 10.1016/j.joule.2022.08.009.
- [6] Lazard. *Levelized Cost of Energy*. 2021. <https://www.lazard.com/perspective/levelized-cost-of-energy-levelized-cost-of-storage-and-levelized-cost-of-hydrogen/> (accessed December 9, 2022).
- [7] Nagy, B.; Farmer, J. D.; Bui, Q. M.; Trancik, J. E. Statistical basis for predicting technological progress. *PLoS One* **2013**, 8 (2), e52669. DOI: 10.1371/journal.pone.0052669.
- [8] Jones-Albertus, B. *Confronting the Duck Curve: How to Address Over-Generation of Solar Energy*. 2017. <https://www.energy.gov/eere/articles/confronting-duck-curve-how-address-over-generation-solar-energy> (accessed 2022 December 10).
- [9] Hydrogen Council, M. C. *Hydrogen for Net Zero*; 2021. <https://hydrogencouncil.com/en/hydrogen-for-net-zero/>.
- [10] IRENA. *Hydrogen from Renewable Power: Technology Outlook for the Energy Transition*; 2018. <https://www.irena.org/publications/2018/sep/hydrogen-from-renewable-power>.

- [11] Hydrogen Council, M. C. *Path to Hydrogen Competitiveness: A Cost Perspective*; 2020. <https://hydrogencouncil.com/en/path-to-hydrogen-competitiveness-a-cost-perspective/>.
- [12] *Parts of a Fuel Cell*. US Office of Energy Efficiency and Renewable Energy, <http://archive.today/2023.01.02-202259/https://www.energy.gov/eere/fuelcells/parts-fuel-cell> (accessed 2023 January 2).
- [13] Hydrogen Council, M. C. *Hydrogen Insights 2021*; 2021. <https://hydrogencouncil.com/en/hydrogen-insights-2021/>.
- [14] IRENA. *Green hydrogen cost reduction: Scaling up electrolyzers to meet the 1.5C climate goal*; International Renewable Energy Agency, Abu Dhabi, 2020. <https://www.irena.org/publications/2020/Dec/Green-hydrogen-cost-reduction>.
- [15] Setzler, B. P.; Zhuang, Z.; Wittkopf, J. A.; Yan, Y. Activity targets for nanostructured platinum-group-metal-free catalysts in hydroxide exchange membrane fuel cells. *Nat Nanotechnol* **2016**, *11* (12), 1020-1025. DOI: 10.1038/nnano.2016.265.
- [16] Abbasi, R.; Setzler, B. P.; Lin, S.; Wang, J.; Zhao, Y.; Xu, H.; Pivovar, B.; Tian, B.; Chen, X.; Wu, G.; et al. A Roadmap to Low-Cost Hydrogen with Hydroxide Exchange Membrane Electrolyzers. *Adv Mater* **2019**, *31* (31), e1805876. DOI: 10.1002/adma.201805876.
- [17] Durst, J.; Siebel, A.; Simon, C.; Hasche, F.; Herranz, J.; Gasteiger, H. A. New insights into the electrochemical hydrogen oxidation and evolution reaction mechanism. *Energy & Environmental Science* **2014**, *7* (7), 2255-2260. DOI: 10.1039/c4ee00440j.
- [18] Marcus, R. A. On the Theory of Electron-Transfer Reactions. VI. Unified Treatment for Homogeneous and Electrode Reactions. *The Journal of Chemical Physics* **1965**, *43* (2), 679-701. DOI: 10.1063/1.1696792.
- [19] Marcus, R. A. Electrostatic Free Energy and Other Properties of States Having Nonequilibrium Polarization. *Journal of Chemical Physics* **1956**, *24*, 979-985.
- [20] Marcus, R. A. On the Theory of Oxidation-Reduction Reactions Involving Electron Transfer. *Journal of Chemical Physics* **1956**, *24*, 966-977.
- [21] Hush, N. S. Adiabatic theory of outer sphere electron-transfer reactions in solution. *Transactions of the Faraday Society* **1961**, *57*. DOI: 10.1039/tf9615700557.

- [22] Straus, J. B.; Calhoun, A.; Voth, G. A. Calculation of solvent free energies for heterogeneous electron transfer at the water–metal interface: Classical versus quantum behavior. *The Journal of Chemical Physics* **1995**, *102* (1), 529-539. DOI: 10.1063/1.469431.
- [23] Bligaard, T.; Nørskov, J. K.; Dahl, S.; Matthiesen, J.; Christensen, C. H.; Sehested, J. The Brønsted–Evans–Polanyi relation and the volcano curve in heterogeneous catalysis. *Journal of Catalysis* **2004**, *224* (1), 206-217. DOI: 10.1016/j.jcat.2004.02.034.
- [24] Jie Zheng, W. S., Zhongbin Zhuang, Bingjun Xu, Yushan Yan. Universal dependence of hydrogen oxidation and evolution reaction activity of platinum-group metals on pH and hydrogen binding energy. *Science Advances* **2016**. DOI: 10.1126/sciadv.1501602.
- [25] Sheng, W. C.; Myint, M.; Chen, J. G. G.; Yan, Y. S. Correlating the hydrogen evolution reaction activity in alkaline electrolytes with the hydrogen binding energy on monometallic surfaces. *Energy & Environmental Science* **2013**, *6* (5), 1509-1512. DOI: 10.1039/c3ee00045a.
- [26] Hammer, B.; Nørskov, J. K. Theoretical surface science and catalysis - Calculations and concepts. *Adv Catal* **2000**, *45*, 71-129. DOI: 10.1016/S0360-0564(02)45013-4.
- [27] Zheng, J.; Nash, J.; Xu, B.; Yan, Y. Perspective—Towards Establishing Apparent Hydrogen Binding Energy as the Descriptor for Hydrogen Oxidation/Evolution Reactions. *Journal of The Electrochemical Society* **2018**, *165* (2), H27-H29. DOI: 10.1149/2.0881802jes.
- [28] Giles, S. A.; Wilson, J. C.; Nash, J.; Xu, B. J.; Vlachos, D. G.; Yan, Y. S. Recent advances in understanding the pH dependence of the hydrogen oxidation and evolution reactions. *Journal of Catalysis* **2018**, *367*, 328-331. DOI: 10.1016/j.jcat.2018.09.030.
- [29] Cheng, T.; Wang, L.; Merinov, B. V.; Goddard, W. A., 3rd. Explanation of Dramatic pH-Dependence of Hydrogen Binding on Noble Metal Electrode: Greatly Weakened Water Adsorption at High pH. *J Am Chem Soc* **2018**, *140* (25), 7787-7790. DOI: 10.1021/jacs.8b04006.
- [30] Herranz, J.; Durst, J.; Fabbri, E.; Patru, A.; Cheng, X.; Permyakova, A. A.; Schmidt, T. J. Interfacial effects on the catalysis of the hydrogen evolution, oxygen evolution and CO₂-reduction reactions for (co-)electrolyzer development. *Nano Energy* **2016**, *29*, 4-28. DOI: 10.1016/j.nanoen.2016.01.027.

- [31] Rebollar, L.; Intikhab, S.; Oliveira, N. J.; Yan, Y.; Xu, B.; McCrum, I. T.; Snyder, J. D.; Tang, M. H. "Beyond Adsorption" Descriptors in Hydrogen Electrocatalysis. *ACS Catalysis* **2020**, *10* (24), 14747-14762. DOI: 10.1021/acscatal.0c03801.
- [32] Chen, X.; McCrum, I. T.; Schwarz, K. A.; Janik, M. J.; Koper, M. T. M. Co-adsorption of Cations as the Cause of the Apparent pH Dependence of Hydrogen Adsorption on a Stepped Platinum Single-Crystal Electrode. *Angew Chem Int Ed Engl* **2017**, *56* (47), 15025-15029. DOI: 10.1002/anie.201709455.
- [33] Janik, M. J.; McCrum, I. T.; Koper, M. T. M. On the presence of surface bound hydroxyl species on polycrystalline Pt electrodes in the "hydrogen potential region" (0-0.4 V-RHE). *Journal of Catalysis* **2018**, *367*, 332-337. DOI: 10.1016/j.jcat.2018.09.031.
- [34] McCrum, I. T.; Janik, M. J. pH and Alkali Cation Effects on the Pt Cyclic Voltammogram Explained Using Density Functional Theory. *The Journal of Physical Chemistry C* **2015**, *120* (1), 457-471. DOI: 10.1021/acs.jpcc.5b10979.
- [35] Danilovic, N.; Subbaraman, R.; Strmcnik, D.; Chang, K. C.; Paulikas, A. P.; Stamenkovic, V. R.; Markovic, N. M. Enhancing the alkaline hydrogen evolution reaction activity through the bifunctionality of Ni(OH)₂/metal catalysts. *Angew Chem Int Ed Engl* **2012**, *51* (50), 12495-12498. DOI: 10.1002/anie.201204842.
- [36] Strmcnik, D.; Lopes, P. P.; Genorio, B.; Stamenkovic, V. R.; Markovic, N. M. Design principles for hydrogen evolution reaction catalyst materials. *Nano Energy* **2016**, *29*, 29-36. DOI: 10.1016/j.nanoen.2016.04.017.
- [37] Jia, Q. Y.; Liu, E. S.; Jiao, L.; Li, J. K.; Mukerjee, S. Current understandings of the sluggish kinetics of the hydrogen evolution and oxidation reactions in base. *Current Opinion in Electrochemistry* **2018**, *12*, 209-217. DOI: 10.1016/j.coelec.2018.11.017.
- [38] Li, J.; Ghoshal, S.; Bates, M. K.; Miller, T. E.; Davies, V.; Stavitski, E.; Attenkofer, K.; Mukerjee, S.; Ma, Z. F.; Jia, Q. Experimental Proof of the Bifunctional Mechanism for the Hydrogen Oxidation in Alkaline Media. *Angew Chem Int Ed Engl* **2017**, *56* (49), 15594-15598. DOI: 10.1002/anie.201708484.
- [39] Lamoureux, P. S.; Singh, A. R.; Chan, K. R. pH Effects on Hydrogen Evolution and Oxidation over Pt(111): Insights from First-Principles. *ACS Catalysis* **2019**, *9* (7), 6194-6201. DOI: 10.1021/acscatal.9b00268.

- [40] McCrum, I. T.; Koper, M. T. M. The role of adsorbed hydroxide in hydrogen evolution reaction kinetics on modified platinum. *Nature Energy* **2020**, *5* (11), 891-899. DOI: 10.1038/s41560-020-00710-8.
- [41] Huang, J.; Li, P.; Chen, S. L. Quantitative Understanding of the Sluggish Kinetics of Hydrogen Reactions in Alkaline Media Based on a Microscopic Hamiltonian Model for the Volmer Step. *J Phys Chem C* **2019**, *123* (28), 17325-17334. DOI: 10.1021/acs.jpcc.9b03639.
- [42] Schouten, K. J.; van der Niet, M. J.; Koper, M. T. Impedance spectroscopy of H and OH adsorption on stepped single-crystal platinum electrodes in alkaline and acidic media. *Phys Chem Chem Phys* **2010**, *12* (46), 15217-15224. DOI: 10.1039/c0cp00104j.
- [43] Intikhab, S.; Snyder, J. D.; Tang, M. H. Adsorbed Hydroxide Does Not Participate in the Volmer Step of Alkaline Hydrogen Electrocatalysis. *ACS Catalysis* **2017**, *7* (12), 8314-8319. DOI: 10.1021/acscatal.7b02787.
- [44] Frumkin, A. N. Wasserstoffüberspannung und Struktur der Doppelschicht. *Zeitschrift für Physikalische Chemie* **1933**, *164*, 121. DOI: 10.1515/zpch-1933-16411.
- [45] Huang, J.; Chen, S. L. Interplay between Covalent and Noncovalent Interactions in Electrocatalysis. *J Phys Chem C* **2018**, *122* (47), 26910-26921. DOI: 10.1021/acs.jpcc.8b07534.
- [46] Ledezma-Yanez, I.; Wallace, W. D. Z.; Sebastian-Pascual, P.; Climent, V.; Feliu, J. M.; Koper, M. T. M. Interfacial water reorganization as a pH-dependent descriptor of the hydrogen evolution rate on platinum electrodes. *Nature Energy* **2017**, *2* (4). DOI: 10.1038/nenergy.2017.31.
- [47] Sarabia, F. J.; Sebastian-Pascual, P.; Koper, M. T. M.; Climent, V.; Feliu, J. M. Effect of the Interfacial Water Structure on the Hydrogen Evolution Reaction on Pt(111) Modified with Different Nickel Hydroxide Coverages in Alkaline Media. *ACS Appl Mater Interfaces* **2019**, *11* (1), 613-623. DOI: 10.1021/acsami.8b15003.
- [48] Huang, B.; Rao, R. R.; You, S.; Hpone Myint, K.; Song, Y.; Wang, Y.; Ding, W.; Giordano, L.; Zhang, Y.; Wang, T.; et al. Cation- and pH-Dependent Hydrogen Evolution and Oxidation Reaction Kinetics. *JACS Au* **2021**, *1* (10), 1674-1687. DOI: 10.1021/jacsau.1c00281.

- [49] Magnussen, O. M.; Gross, A. Toward an Atomic-Scale Understanding of Electrochemical Interface Structure and Dynamics. *J Am Chem Soc* **2019**, *141* (12), 4777-4790. DOI: 10.1021/jacs.8b13188.
- [50] Yang, G.; Akhade, S. A.; Chen, X.; Liu, Y.; Lee, M. S.; Glezakou, V. A.; Rousseau, R.; Lercher, J. A. The Nature of Hydrogen Adsorption on Platinum in the Aqueous Phase. *Angew Chem Int Ed Engl* **2019**, *58* (11), 3527-3532. DOI: 10.1002/anie.201813958.
- [51] Chen, L. D.; Bajdich, M.; Martinez, J. M. P.; Krauter, C. M.; Gauthier, J. A.; Carter, E. A.; Luntz, A. C.; Chan, K.; Norskov, J. K. Understanding the apparent fractional charge of protons in the aqueous electrochemical double layer. *Nat Commun* **2018**, *9* (1), 3202. DOI: 10.1038/s41467-018-05511-y.
- [52] Le, J. B.; Fan, Q. Y.; Li, J. Q.; Cheng, J. Molecular origin of negative component of Helmholtz capacitance at electrified Pt(111)/water interface. *Sci Adv* **2020**, *6* (41). DOI: 10.1126/sciadv.abb1219.
- [53] Abidi, N.; Lim, K. R. G.; Seh, Z. W.; Steinmann, S. N. Atomistic modeling of electrocatalysis: Are we there yet? *WIREs Computational Molecular Science* **2020**, *11* (3). DOI: 10.1002/wcms.1499.
- [54] Melander, M. M. Grand canonical ensemble approach to electrochemical thermodynamics, kinetics, and model Hamiltonians. *Current Opinion in Electrochemistry* **2021**, *29*. DOI: 10.1016/j.coelec.2021.100749.
- [55] Melander, M. M.; Kuisma, M. J.; Christensen, T. E. K.; Honkala, K. Grand-canonical approach to density functional theory of electrocatalytic systems: Thermodynamics of solid-liquid interfaces at constant ion and electrode potentials. *J Chem Phys* **2019**, *150* (4), 041706. DOI: 10.1063/1.5047829.
- [56] Sundararaman, R.; Goddard, W. A., 3rd; Arias, T. A. Grand canonical electronic density-functional theory: Algorithms and applications to electrochemistry. *J Chem Phys* **2017**, *146* (11), 114104. DOI: 10.1063/1.4978411.
- [57] Santos, E.; Lundin, A.; Potting, K.; Quaino, P.; Schmickler, W. Model for the electrocatalysis of hydrogen evolution. *Physical Review B* **2009**, *79* (23). DOI: 10.1103/PhysRevB.79.235436z.
- [58] Lam, Y. C.; Soudackov, A. V.; Goldsmith, Z. K.; Hammes-Schiffer, S. Theory of Proton Discharge on Metal Electrodes: Electronically Adiabatic Model. *J Phys Chem C* **2019**, *123* (19), 12335-12345. DOI: 10.1021/acs.jpcc.9b02148.

- [59] Lam, Y. C.; Soudackov, A. V.; Hammes-Schiffer, S. Kinetics of Proton Discharge on Metal Electrodes: Effects of Vibrational Nonadiabaticity and Solvent Dynamics. *J Phys Chem Lett* **2019**, *10* (18), 5312-5317. DOI: 10.1021/acs.jpcclett.9b01984.
- [60] Petersen, M. K.; Kumar, R.; White, H. S.; Voth, G. A. A Computationally Efficient Treatment of Polarizable Electrochemical Cells Held at a Constant Potential. *J Phys Chem C* **2012**, *116* (7), 4903-4912. DOI: 10.1021/jp210252g.
- [61] Reed, S. K.; Lanning, O. J.; Madden, P. A. Electrochemical interface between an ionic liquid and a model metallic electrode. *J Chem Phys* **2007**, *126* (8), 084704. DOI: 10.1063/1.2464084.
- [62] Merlet, C.; Limmer, D. T.; Salanne, M.; van Roij, R.; Madden, P. A.; Chandler, D.; Rotenberg, B. The Electric Double Layer Has a Life of Its Own. *J Phys Chem C* **2014**, *118* (32), 18291-18298. DOI: 10.1021/jp503224w.
- [63] Limmer, D. T.; Willard, A. P. Nanoscale heterogeneity at the aqueous electrolyte-electrode interface. *Chemical Physics Letters* **2015**, *620*, 144-150. DOI: 10.1016/j.cplett.2014.11.013.
- [64] Limmer, D. T.; Willard, A. P.; Madden, P.; Chandler, D. Hydration of metal surfaces can be dynamically heterogeneous and hydrophobic. *P Natl Acad Sci USA* **2013**, *110* (11), 4200-4205. DOI: 10.1073/pnas.1301596110.
- [65] Newns, D. M. Self-Consistent Model of Hydrogen Chemisorption. *Physical Review* **1969**, *178* (3), 1123-1135. DOI: 10.1103/PhysRev.178.1123.
- [66] Santos, E.; Lundin, A.; Pötting, K.; Quaino, P.; Schmickler, W. Model for the electrocatalysis of hydrogen evolution. *Physical Review B* **2009**, *79* (23). DOI: 10.1103/PhysRevB.79.235436.
- [67] Huang, J. Mixed quantum-classical treatment of electron transfer at electrocatalytic interfaces: Theoretical framework and conceptual analysis. *J Chem Phys* **2020**, *153* (16), 164707. DOI: 10.1063/5.0009582.
- [68] Mejías, J. A.; Lago, S. Calculation of the absolute hydration enthalpy and free energy of H⁺ and OH⁻. *The Journal of Chemical Physics* **2000**, *113* (17), 7306-7316. DOI: 10.1063/1.1313793.
- [69] Calhoun, A.; Koper, M. T. M.; Voth, G. A. Large-scale computer simulation of an electrochemical bond-breaking reaction. *Chemical Physics Letters* **1999**, *305* (1-2), 94-100. DOI: 10.1016/s0009-2614(99)00353-x.

- [70] Sheng, W.; Zhuang, Z.; Gao, M.; Zheng, J.; Chen, J. G.; Yan, Y. Correlating hydrogen oxidation and evolution activity on platinum at different pH with measured hydrogen binding energy. *Nat Commun* **2015**, *6*, 5848. DOI: 10.1038/ncomms6848.
- [71] Intikhab, S.; Rebollar, L.; Fu, X.; Yue, Q.; Li, Y.; Kang, Y.; Tang, M. H.; Snyder, J. D. Exploiting dynamic water structure and structural sensitivity for nanoscale electrocatalyst design. *Nano Energy* **2019**, *64*. DOI: 10.1016/j.nanoen.2019.103963.
- [72] Ledezma-Yanez, I.; Wallace, W. D. Z.; Sebastián-Pascual, P.; Climent, V.; Feliu, J. M.; Koper, M. T. M. Interfacial water reorganization as a pH-dependent descriptor of the hydrogen evolution rate on platinum electrodes. *Nature Energy* **2017**, *2* (4). DOI: 10.1038/nenergy.2017.31.
- [73] Liu, E.; Li, J.; Jiao, L.; Doan, H. T. T.; Liu, Z.; Zhao, Z.; Huang, Y.; Abraham, K. M.; Mukerjee, S.; Jia, Q. Unifying the Hydrogen Evolution and Oxidation Reactions Kinetics in Base by Identifying the Catalytic Roles of Hydroxyl-Water-Cation Adducts. *J Am Chem Soc* **2019**, *141* (7), 3232-3239. DOI: 10.1021/jacs.8b13228.
- [74] Ramaswamy, N.; Ghoshal, S.; Bates, M. K.; Jia, Q. Y.; Li, J. K.; Mukerjee, S. Hydrogen oxidation reaction in alkaline media: Relationship between electrocatalysis and electrochemical double-layer structure. *Nano Energy* **2017**, *41*, 765-771. DOI: 10.1016/j.nanoen.2017.07.053.
- [75] Tsirlina, G. A.; Petrii, O. A.; Nazmutdinov, R. R.; Glukhov, D. V. Frumkin correction: Microscopic view. *Russian Journal of Electrochemistry* **2002**, *38* (2), 132-140. DOI: 10.1023/A:1016812130377.
- [76] McQuarrie, D. A. *Statistical Mechanics*; Harpercollins College Div, 1976.
- [77] Hynes, J. T. Chemical reaction rates and solvent friction. *Journal of Statistical Physics* **1986**, *42* (1-2), 149-168. DOI: 10.1007/bf01010844.
- [78] Hörmann, N. G.; Marzari, N.; Reuter, K. Electrosorption at metal surfaces from first principles. *npj Computational Materials* **2020**, *6* (1). DOI: 10.1038/s41524-020-00394-4.
- [79] Intikhab, S.; Rebollar, L.; Li, Y.; Pai, R.; Kalra, V.; Tang, M. H.; Snyder, J. D. Caffeinated Interfaces Enhance Alkaline Hydrogen Electrocatalysis. *ACS Catalysis* **2020**, *10* (12), 6798-6802. DOI: 10.1021/acscatal.0c01635.

- [80] Rebollar, L.; Intikhab, S.; Zhang, S. H.; Deng, H. Q.; Zeng, Z. H.; Snyder, J. D.; Tang, M. H. On the relationship between potential of zero charge and solvent dynamics in the reversible hydrogen electrode. *Journal of Catalysis* **2021**, *398*, 161-170. DOI: 10.1016/j.jcat.2021.04.008.
- [81] Ryu, J.; Surendranath, Y. Tracking Electrical Fields at the Pt/H₂O Interface during Hydrogen Catalysis. *J Am Chem Soc* **2019**, *141* (39), 15524-15531. DOI: 10.1021/jacs.9b05148.
- [82] Muscat, J. P.; Newns, D. M. Chemisorption on metals. *Progress in Surface Science* **1978**, *9* (1), 1-43. DOI: 10.1016/0079-6816(78)90005-9.
- [83] Grimley, T. B. Chemisorption Theory. In *Progress in Surface and Membrane Science*, Cadenhead, D. A., Danielli, J.F., and Rosenberg, M.D. Ed.; Vol. 9; 1975; pp 71-161.
- [84] Zhu, F.; Hummer, G. Convergence and error estimation in free energy calculations using the weighted histogram analysis method. *J Comput Chem* **2012**, *33* (4), 453-465. DOI: 10.1002/jcc.21989.
- [85] MacKerell, A. D.; Bashford, D.; Bellott, M.; Dunbrack, R. L.; Evanseck, J. D.; Field, M. J.; Fischer, S.; Gao, J.; Guo, H.; Ha, S.; et al. All-atom empirical potential for molecular modeling and dynamics studies of proteins. *J Phys Chem B* **1998**, *102* (18), 3586-3616. DOI: 10.1021/jp973084f.
- [86] Siepmann, J. I.; Sprik, M. Influence of Surface-Topology and Electrostatic Potential on Water Electrode Systems. *Journal of Chemical Physics* **1995**, *102* (1), 511-524. DOI: 10.1063/1.469429.
- [87] Strmcnik, D.; Kodama, K.; van der Vliet, D.; Greeley, J.; Stamenkovic, V. R.; Markovic, N. M. The role of non-covalent interactions in electrocatalytic fuel-cell reactions on platinum. *Nat Chem* **2009**, *1* (6), 466-472. DOI: 10.1038/nchem.330.
- [88] Waagele, M. M.; Gunathunge, C. M.; Li, J.; Li, X. How cations affect the electric double layer and the rates and selectivity of electrocatalytic processes. *J Chem Phys* **2019**, *151* (16), 160902. DOI: 10.1063/1.5124878.
- [89] Weber, D. J.; Janssen, M.; Oezaslan, M. Effect of Monovalent Cations on the HOR/HER Activity for Pt in Alkaline Environment. *Journal of the Electrochemical Society* **2019**, *166* (2), F66-F73. DOI: 10.1149/2.0301902jes.

- [90] Kumar, S.; Rosenberg, J. M.; Bouzida, D.; Swendsen, R. H.; Kollman, P. A. THE weighted histogram analysis method for free-energy calculations on biomolecules. I. The method. *Journal of Computational Chemistry* **1992**, *13* (8), 1011-1021. DOI: 10.1002/jcc.540130812.
- [91] Wang, F. N.; Xu, G.; He, Y. H.; Liu, Z. P.; Zhang, Z. G.; Mao, Q.; Huang, Y. Q. Into the "secret" double layer: Alkali cation mediates the hydrogen evolution reaction in basic medium. *Journal of Energy Chemistry* **2020**, *51*, 101-104. DOI: 10.1016/j.jechem.2020.03.037.
- [92] Baranyai, A.; Evans, D. J. Direct entropy calculation from computer simulation of liquids. *Phys Rev A Gen Phys* **1989**, *40* (7), 3817-3822. DOI: 10.1103/physreva.40.3817.
- [93] Limaye, A. M.; Willard, A. P. Modeling Interfacial Electron Transfer in the Double Layer: The Interplay between Electrode Coupling and Electrostatic Driving. *The Journal of Physical Chemistry C* **2019**, *124* (2), 1352-1361. DOI: 10.1021/acs.jpcc.9b08438.
- [94] Rossmeisl, J.; Chan, K.; Skulason, E.; Bjorketun, M. E.; Tripkovic, V. On the pH dependence of electrochemical proton transfer barriers. *Catalysis Today* **2016**, *262*, 36-40. DOI: 10.1016/j.cattod.2015.08.016.
- [95] Subbaraman, R.; Tripkovic, D.; Chang, K. C.; Strmcnik, D.; Paulikas, A. P.; Hirunsit, P.; Chan, M.; Greeley, J.; Stamenkovic, V.; Markovic, N. M. Trends in activity for the water electrolyser reactions on 3d M(Ni,Co,Fe,Mn) hydr(oxy)oxide catalysts. *Nat Mater* **2012**, *11* (6), 550-557. DOI: 10.1038/nmat3313.
- [96] Strmcnik, D.; Uchimura, M.; Wang, C.; Subbaraman, R.; Danilovic, N.; van der Vliet, D.; Paulikas, A. P.; Stamenkovic, V. R.; Markovic, N. M. Improving the hydrogen oxidation reaction rate by promotion of hydroxyl adsorption. *Nat Chem* **2013**, *5* (4), 300-306. DOI: 10.1038/nchem.1574.
- [97] Schmickler, W. Electronic Effects in the Double Layer. *Chem. Rev.* **1996**, *96*, 3177-3200.
- [98] Tripkovic, V.; Bjorketun, M. E.; Skulason, E.; Rossmeisl, J. Standard hydrogen electrode and potential of zero charge in density functional calculations. *Physical Review B* **2011**, *84* (11). DOI: 10.1103/PhysRevB.84.115452.
- [99] Le, J.-B.; Cheng, J. Modeling electrified metal/water interfaces from ab initio molecular dynamics: Structure and Helmholtz capacitance. *Current Opinion in Electrochemistry* **2021**, *27*. DOI: 10.1016/j.coelec.2021.100693.

- [100] Jackson, J. D. *Classical Electrodynamics*; John Wiley & Sons, 1998.
- [101] Luque, N. B.; Schmickler, W. The electric double layer on graphite. *Electrochimica Acta* **2012**, *71*, 82-85. DOI: 10.1016/j.electacta.2012.03.083.
- [102] Schmickler, W. The electronic response of the metal in simulations of the electric double layer. *Journal of Electroanalytical Chemistry* **2020**, 856. DOI: 10.1016/j.jelechem.2019.113664. [103] Chulkov, E. V.; Silkin, V. M.; Echenique, P. M. Image potential states on lithium, copper and silver surfaces. *Surface Science* **1997**, *391* (1-3), L1217-L1223. DOI: 10.1016/s0039-6028(97)00653-5.
- [104] Melander, M.; Jonsson, E. O.; Mortensen, J. J.; Vegge, T.; Garcia Lastra, J. M. Implementation of Constrained DFT for Computing Charge Transfer Rates within the Projector Augmented Wave Method. *J Chem Theory Comput* **2016**, *12* (11), 5367-5378. DOI: 10.1021/acs.jctc.6b00815.
- [105] Quaino, P.; Luque, N. B.; Nazmutdinov, R.; Santos, E.; Schmickler, W. Why is gold such a good catalyst for oxygen reduction in alkaline media? *Angew Chem Int Ed Engl* **2012**, *51* (52), 12997-13000. DOI: 10.1002/anie.201205902.
- [106] Li, C. Y.; Le, J. B.; Wang, Y. H.; Chen, S.; Yang, Z. L.; Li, J. F.; Cheng, J.; Tian, Z. Q. In situ probing electrified interfacial water structures at atomically flat surfaces. *Nat Mater* **2019**, *18* (7), 697-701. DOI: 10.1038/s41563-019-0356-x.
- [107] Maroncelli, M.; Fleming, G. R. Computer simulation of the dynamics of aqueous solvation. *The Journal of Chemical Physics* **1988**, *89* (8), 5044-5069. DOI: 10.1063/1.455649.

Appendix A

SUPPLEMENTARY INFORMATION FOR CHAPTER 3

Double layer charging relation

Here we explain the relationship between the cell potential and the single-electrode potentials and their surface charge. During the simulation, the induced surface charges on the two electrodes fluctuate to maintain constant potential as the electrolyte species move. The constant potential algorithm allows us to control the potential difference ΔV across the capacitor cell with spacing d while maintaining overall charge neutrality for the system. If we consider an equivalent empty capacitor with cell potential ΔV , the cell is symmetric with field $\Delta V/d$, so we can define a vacuum reference as 0 V in the center of the cell which does not vary with ΔV . Because of the symmetry, the electrode electrostatic potentials can be defined as equal and opposite on an absolute scale versus the reference:

$$V_- = -\frac{\Delta V}{2}$$
$$V_+ = \frac{\Delta V}{2}$$

where V_- and V_+ are the negative and positive electrode potentials. When the empty capacitor is uncharged, both electrode potentials are equal to the reference, that is, $V_- = V_+ = V_{\text{pzc}} = 0$ V when $\Delta V = 0$ V. As defined, the potentials of the respective electrodes relative to the vacuum or PZC are unrelated to the presence of electrolyte, so the above absolute potential relations are well-defined in the electrolyte-filled cell.

The surface charging behavior of each electrode depends strongly on the electrolyte response. The average surface charge on each electrode is related to the double layer capacitance C_{dl} :

$$\langle \sigma \rangle (V) = \int_{V_{pzc}}^V C_{dl}(v) dv$$

Where $\langle \sigma \rangle$ is the ensemble average of the surface charge density and V_{pzc} is the potential of zero free charge. In Figure A.1, we show the capacitor configuration, spatial profile of electrostatic potential, and double layer charging relation for different voltages.

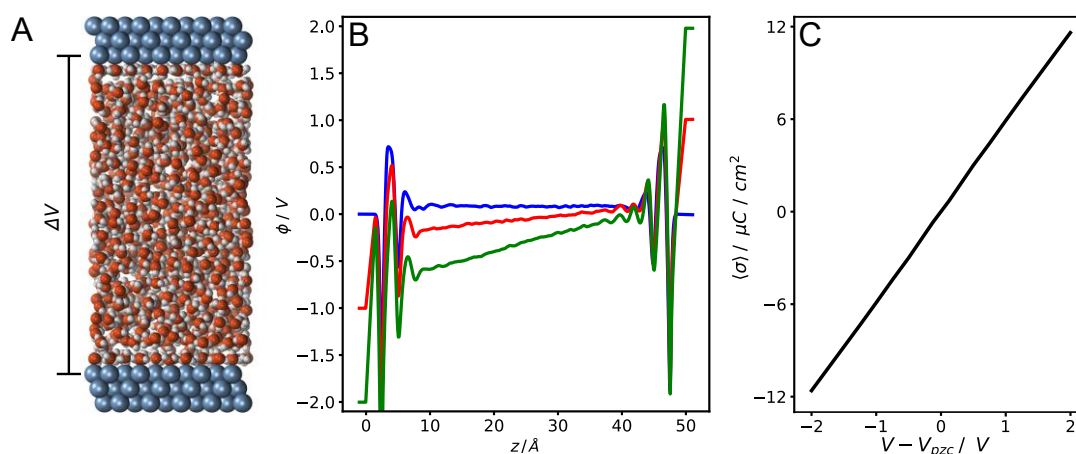


Figure A.1. Potential profile and double charging relation in capacitor cell with neat water. A) Diagram of capacitor cell with gap $D = 50 \text{ \AA}$ between image planes. Waters are placed between two slabs with Pt (111) facets exposed. B) planar-averaged Poisson potential along the length of the capacitor at various applied voltages, C) average surface charge as a function of applied potential, $V - V_{pzc}$. The slope of the line is the double layer capacitance, $C_{dl} \cong 6 \text{ \mu F/cm}^2$, and is due to reorientation of water molecules. (In B, the blue, red, and green curves correspond to $\Delta V = 0 \text{ V}$, 2 V , and 4 V , respectively.)

Figure A.1B shows the correct ΔV is established across the cell, with significant fluctuations in potential due to the orientation of water in the double layer. Moreover, the potential drop across the double layer is asymmetric with respect to the sign of voltage. Adsorbed water naturally tends to orient with its dipole pointing slightly away from the Pt electrodes, but in-plane hydrogen bonding aligns O-H bonds parallel to the surface. Thus, water dipoles more easily rotate away from the positive surface than towards the negative surface, hence the potential drop across the positive electrode double layer is larger.

In Figure A.1C, we show the double layer charging behavior. C_{dl} is nearly constant for the potentials studied and lacks the bell-shaped curve observed on Pt, likely because this model does not reproduce the potential-induced desorption of water⁵². Nevertheless, the classical simulation with image charges maintains constant cell voltage as expected.

Water equilibrium orientation around H^+

In Figure A.2 we plot the equilibrium orientation of water molecules around the H^+ at a fixed position, z , relative to the surface for various electrode potential values. The orientation of the water is defined by the angle

$$\cos(\theta) = \vec{r}_{H^+-O} \cdot \vec{\mu}_{H_2O}$$

where \vec{r}_{H^+-O} is the vector between the proton and a water oxygen in the proton's solvation shell, and $\vec{\mu}_{H_2O}$ is the dipole vector of that solvating water. Only water molecules within 3.2 Å of the proton are included. In panels A, B and C, the proton is fixed at $z = 6$ Å and the electrode potential is 0, -1 and -2 V, respectively. Note how the three distributions are statistically similar, indicating that the electrode field has essentially no effect on the equilibrium polarization of the water solvating the proton.

In A.2D-F, the proton is fixed at $z = 2 \text{ \AA}$ and the electrode potential is 0, -1 and -2 V, respectively. Even at such short distance from the surface, the equilibrium orientation polarization of the solvating water is essentially determined by the proton's strong field. The distributions $P(\theta)$ become noticeably more localized as the proton approaches the surface due to desolvation.

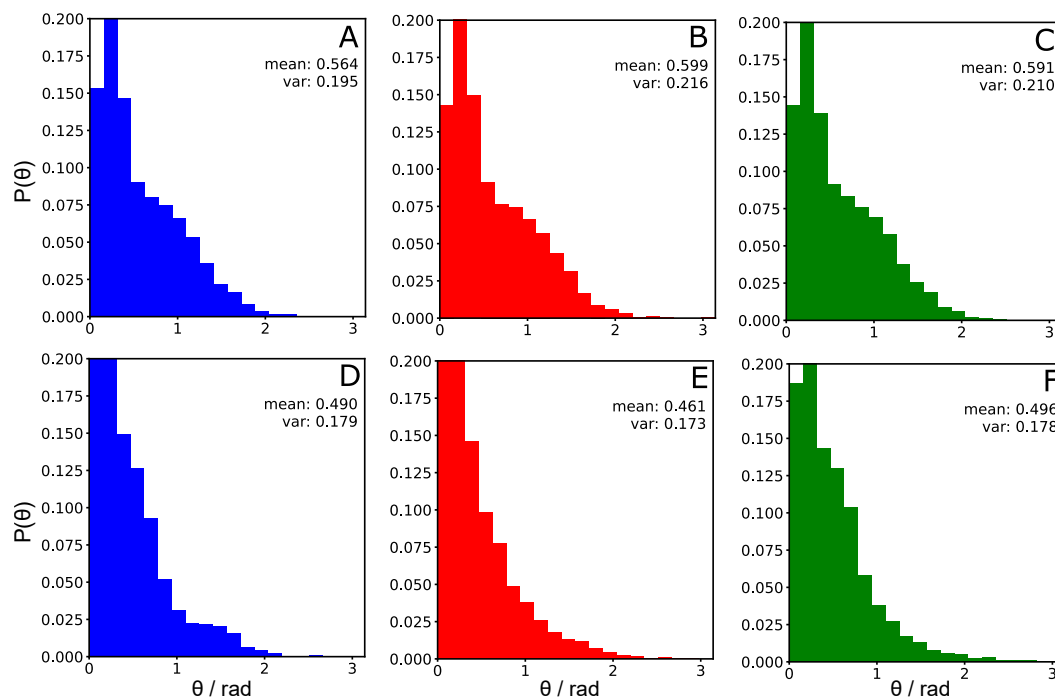


Figure A.2. Angular distribution functions of waters solvating the proton.

Statistics collected for the redox H oxidized diabatic state at fixed z . A), B), C): $z = 6.0 \text{ \AA}$ and D), E), F): $z = 2.0 \text{ \AA}$ for three different voltages. $V - V_{\text{pzc}} = 0 \text{ V}, -1 \text{ V}, -2 \text{ V}$ correspond to blue, red, and green, respectively.

Potential-dependent interfacial water configurations

Since the structure of the interfacial solvent plays an important role in the electrostatics and solvation of ions in the double layer, it is important to accurately model Pt-water interactions. Here we have used the force field from Siepmann and Sprik, which has been widely used for the Pt (111) surface and produces realistic water configurations. Here we show how adsorbed waters respond to changes in the applied voltage. The trends in water reorientation and hydrogen bonding that we observe here are qualitatively similar to results by Li et al. for water on Au, obtained using a combination of AIMD and Raman spectroscopy¹⁰⁶.

In Figure A.3A, snapshots of the surface and first layer of waters are shown at varying voltages. At $V - V_{pzc} = 0$ V, water OH bonds primarily hydrogen bond in-plane with neighboring waters. A few OH bonds point up towards the solution, i.e. “H-up” waters. From the z-distributions of water hydrogens in A.3C, the number of H atoms around $z=2.3\text{\AA}$ and 3.2\AA decreases at negative $V - V_{pzc}$, but increases around $z = 1.5\text{\AA}$. In A.3D, the distribution of angles between the water dipoles and surface normal are shown. Values closer to 1 correspond to H-up waters. As expected, there is a shift from more H-up to more H-down waters at negative voltage.

In A.3E we show the distribution of the number of hydrogen bonds (donors + acceptors) averaged over all surface waters. The criteria we use for a hydrogen bond between two water molecules is when the interoxygen distance between neighboring waters is less than 3.5\AA and the H–O···H angle is $<30^\circ$. At the PZC, most surface waters have 3 or 4 hydrogen bonds. At negative voltages, the number of waters with only 1 or 2 hydrogen bonds increases; there are fewer hydrogen bonds parallel to the

surface and fewer hydrogen bonds between adsorbed waters and waters above the surface. The disruption of hydrogen bonding slightly lowers the coverage of water (A.3B), and more waters occupying 3-fold surface sites are visible in A.3A.

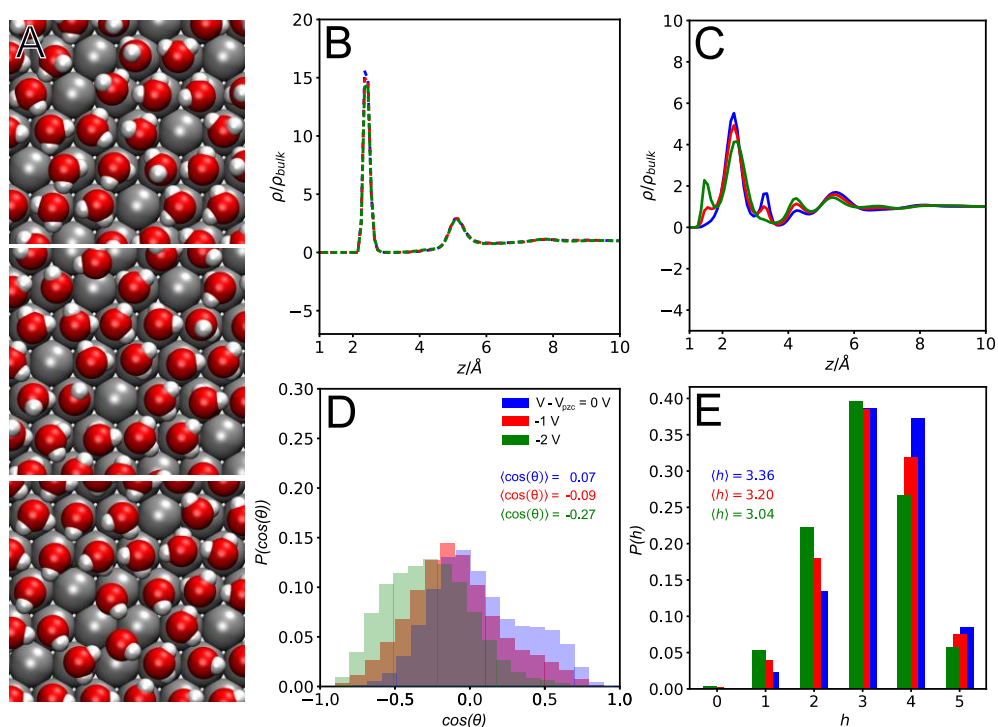


Figure A.3. Potential-dependent interfacial water configurations. A) Characteristic snapshot of adsorbed water configurations at different voltages $V - V_{pzc} = 0$ V, -1 V, -2 V (top to bottom). B) z -distribution functions of oxygen atoms belonging to water. C) z -distribution functions of hydrogen atoms belonging to water. D) distribution of $\cos(\theta)$ of adsorbed water's dipole angles with respect to the surface normal. E) probability distribution of the numbers of hydrogen bonds (donors + acceptors) per adsorbed water.

Solvation water dipole autocorrelation relaxation

In Figure A.4 we plot the dipole moment autocorrelation function $C_{\mu\mu}(t) = \langle \delta\mu(t) \cdot \delta\mu(0) \rangle / \langle \delta\mu(0)^2 \rangle$ for the water molecules in the first solvation shell of the proton at two positions, z , relative to the electrode, and for three values of the electrode potential; $\delta\mu(t)$ is the fluctuation from the mean. Only water molecules within 2 Å of the proton are included. Evidently, there is a distribution of solvation water relaxation times as a function of the distance from the surface. Far from the surface, $z = 6$ Å (Figure A.4A), the collective nuclear motion of the solvating waters results in faster relaxation than at $z=2$ Å (Figure A.4B) where, because of the depletion of the solvation shell due to the proximity to the surface, there is insufficient number of water molecules to achieve cooperativity and fast relaxation. Moreover, the water molecules solvating the proton are themselves adsorbed and reorient extremely slowly due to surface confinement effects. In the latter case, after the initial fast librational relaxation, the slow orientation relaxation is essentially determined by the slow response of a single molecule¹⁰⁷. Furthermore, we see once again that the electrode field has an insignificant effect on the relaxation time, which is primarily determined by the strong field of the proton. Thus, neither the equilibrium distribution of water dipoles around the proton (see Appendix A.3) nor the dynamics of the solvation water are influenced by the electrode field and this is reflected in the essentially unchanging solvent reorganization energy with electrode potential.

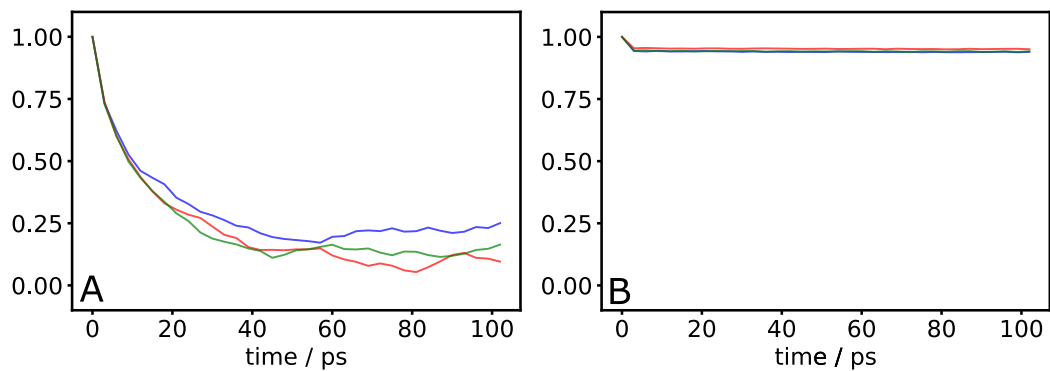


Figure A.4. Dipole moment autocorrelation functions for waters solvating H^+ . The results are plotted for the proton at fixed z where A) $z = 6.0 \text{ \AA}$ B) $z = 2.0 \text{ \AA}$ for three different voltages. $V - V_{\text{pzc}} = 0 \text{ V}, -1 \text{ V}, -2 \text{ V}$ shown in blue, red, and green, respectively.

Proton electrostatic potential autocorrelation functions

Since ion-solvent coupling is strong along the Volmer reaction coordinate, it is important to understand solvent dynamics, which can affect the shape of the transition state and recrossing rates beyond the classical transition state theory approximation. In the present regime of strong solute-solvent coupling, the electron transfer rate constant is inversely proportional to the solvation time⁷⁷, i.e. $k_{et} \propto \tau^{-1}$. To estimate the collective solvation relaxation time, here we calculate the autocorrelation function for the proton's local electrostatic potential, where the proton is placed at fixed z above the electrode. The electrostatic potential autocorrelation function is calculated as follows¹⁰⁷:

$$C_{\phi\phi} = \langle \delta\phi(t)\delta\phi(0) \rangle$$

$$\delta\phi = \phi(t) - \langle \phi \rangle$$

where $\delta\phi$ is the instantaneous deviation from the ensemble average of the potential.

We also estimate the mean relaxation time for this process by integrating the normalized autocorrelation function¹⁰⁷:

$$\langle \tau \rangle = \int_0^{\infty} C_{\phi\phi}(t) dt$$

where the integral is truncated to 3ps to avoid integrating through long times which have large sampling error. $\langle \tau \rangle$ is thus a lower bound estimate of the mean solvation time. Close to the surface, solvation is faster when the interfacial field is stronger, likely due to frustrated hydrogen bonding (Figure A.3A). Further from the surface, the interfacial field has less of an effect on solvation time due to the smaller magnitude of the electric field and lack of hydrogen bonding disruption (Figure A.4B, A.4C).

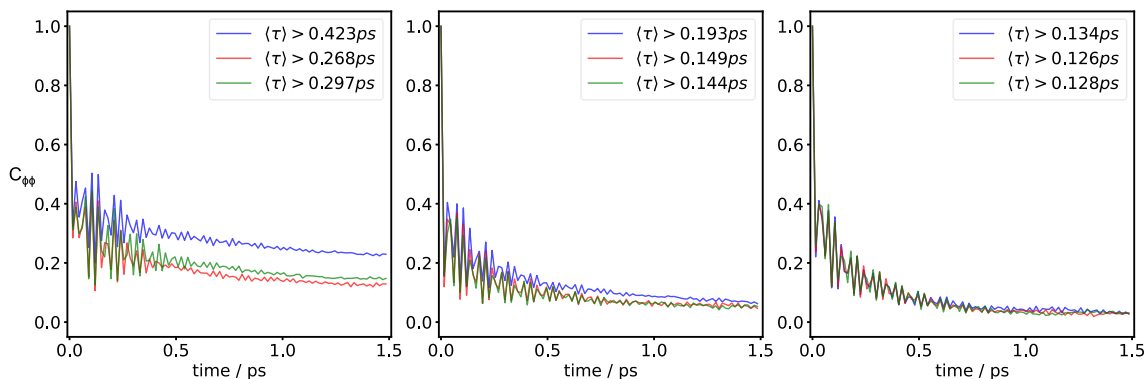


Figure A.5. Autocorrelation for electrostatic potential of the proton at fixed z . The rate of relaxation of the electrostatic potential is proportional to the solvation time of the ion. Close to the surface, the solvation becomes more sluggish due to confinement of water on Pt (111). At more negative potentials, the librational contribution at short times (< 50 fs) is faster, and solvation occurs more rapidly. A) $z = 2.0$ Å, B) $z = 4.0$ Å, C) $z = 6.0$ Å.

Effect of overpotential on adiabatic ET

In Figure A.6, we plot results from computing the Volmer adiabatic free energy surfaces where the electrode electrostatic potential $V - V_{pzc}$ varies along with the overpotential, e.g. at $V - V_{pzc} = -1$ V, the reduction overpotential is 1eV larger than at $V - V_{pzc} = 0$ V. Shifting the Fermi level higher biases the reaction to reduction (A.6B), and the reduction transition state occurs earlier (A.6A), indicating a shrinking reduction charge transfer coefficient. Additionally, the more negative electrostatic potential attracts H^+ to the surface. Interestingly, the reduction was expected to be barrierless at an overpotential of -1 V, however, we still observe a significant barrier because the H^+ state near the surface is stabilized by the negatively charged surface. In essence, the change in bias towards reduction with increasing overpotential is less than expected due to the poorly screened negative surface charge, which favors the oxidized state.

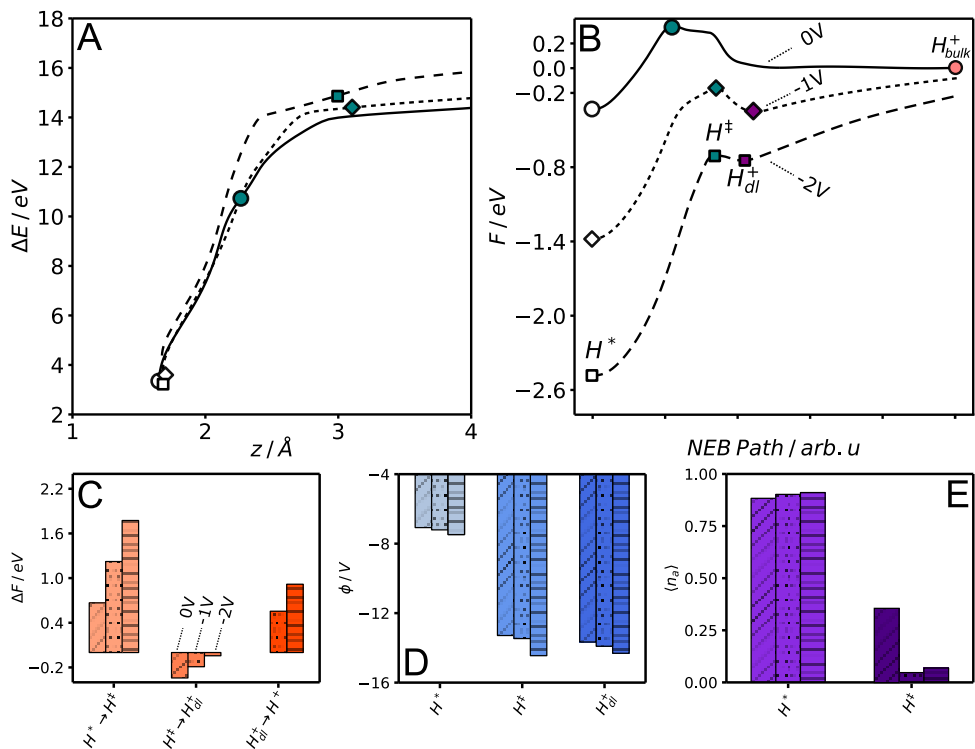


Figure A.6. Raising the Fermi level biases the reaction to reduction. 2D adiabatic surfaces analysis for H^+/H redox near Pt (111). Here, the electrode electrostatic potential $V - V_{\text{pzc}}$ and the Fermi level are connected. Three cases are shown: $V - V_{\text{pzc}} = 0$ V with $\epsilon_a - \epsilon_f = -10.2$ eV, $V - V_{\text{pzc}} = -1$ V with $\epsilon_a - \epsilon_f = -11.2$ eV, and $V - V_{\text{pzc}} = -2$ V with $\epsilon_a - \epsilon_f = -12.2$ eV. **A)** the MFEP along the reaction coordinates ΔE and z for the three electrode potentials. **B)** the free energies along the MFEP projected onto 1D. **C)** the free energy changes for the steps along the MFEP are shown. **D)** the average electrostatic potential experienced by hydrogen is shown for H^* , H^\ddagger , and H^\ddagger_{dl} . **E)** the average expected occupancy is shown for H^* and for H^\ddagger . (In A and B, the solid, dotted, and dashed lines correspond to the 0 V, -1 V, and -2 V cases, respectively. In C, D, and E, the diagonal bar hatches, dotted hatches, and horizontal bar hatches correspond to the 0 V, -1 V, and -2 V cases, respectively.)

Hydrogen – water coordination numbers for adiabatic ET

We calculate the coordination of water atoms around the H atom at various z distances where H is electronically coupled to the surface (Figure A.7). The H atom is prepared in its most favorable state at each z (i.e. reduced close to the surface, oxidized far away) and relaxes to equilibrium solvation. As hydrogen approaches the surface and eventually becomes reduced, it loses solvation energy, reflected in the loss of coordinating water oxygens in the first two solvation shells. The first two solvation shells approximately correspond to $r < 1.5 \text{ \AA}$ and $1.5 \text{ \AA} < r < 3.2 \text{ \AA}$, respectively. A stronger surface charge and corresponding interfacial field does not significantly affect the hydrogen solvation structure, and only minor changes in the coordination number profiles are noted (A.7A-D).

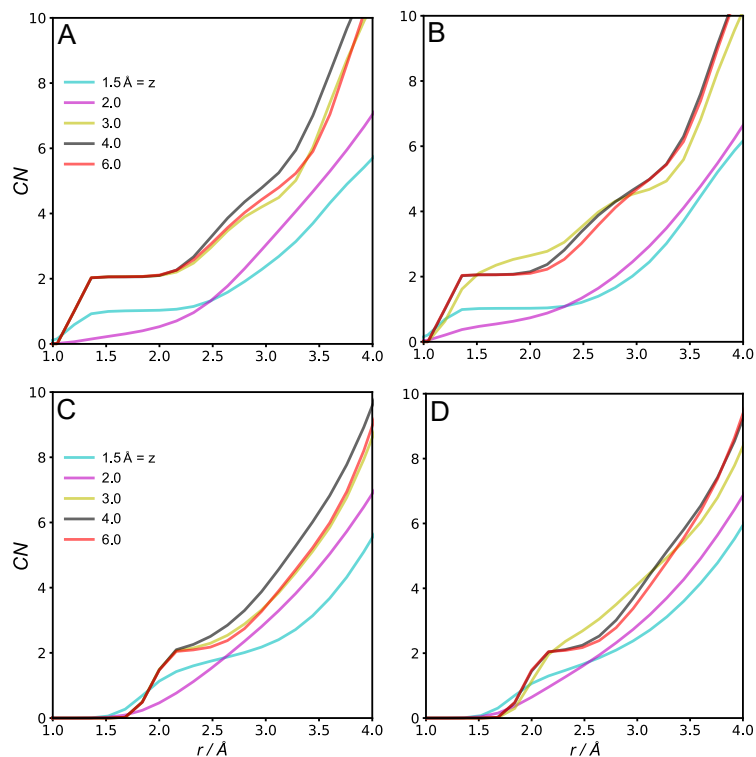


Figure A.7. Coordination numbers of water atoms around the redox hydrogen for adiabatic ET at fixed hydrogen z and varied cell voltage $V - V_{\text{pzc}}$. The Fermi level is set to $\epsilon_a - \epsilon_f = -10.2$ eV. At $z > 2.0$ Å, hydrogen is oxidized, and at $z \leq 2.0$ Å, hydrogen is reduced. Changing $V - V_{\text{pzc}}$ only slightly affects the equilibrium solvation of hydrogen. A) CNs of water O around redox H at $V - V_{\text{pzc}} = 0$ V. B) CNs of water O around redox H at $V - V_{\text{pzc}} = -2$ V. C) CNs of water H around redox H at $V - V_{\text{pzc}} = 0$ V. D) CNs of water H around redox H at $V - V_{\text{pzc}} = -2$ V.

Referencing procedure for proton free energies

Here, we outline a procedure for connecting the free energy scales of simulations performed at different electrode potentials. First, we must pick a reference state. In electrochemical experiments at constant potential, adsorbed hydrogen reaches an equilibrium with H^+ in bulk solution. H^+ in bulk solution is not influenced by the surface, so choosing bulk H^+ as a reference state is convenient. We can simulate a proton in solution in our system, which additionally makes it a convenient choice for a reference. However, we simulate a small capacitor cell, and we must be careful to consider the electrostatics of ion-surface interactions since the Coulomb interactions are long range.

In the simulation, H^+ reaches bulk solvation far from the double layer, and its free energy can be expressed as follows relative to vacuum:

$$F_{H^+} = F_{H^+}^{sol} + zF\phi_{H^+}$$

where ϕ_{H^+} is the local electrostatic potential at the H^+ position, $F_{H^+}^{sol}$ is the bulk solvation free energy, and z is the proton charge. In these simulations with water and no electrolyte salt, the Debye length is longer than the cell length. Consequently, when applying a potential difference $\Delta V \neq 0 V$, the proton is influenced by the surface potential at all points in the cell. However, at $\Delta V = 0 V$, both electrodes are at the PZC, and the proton at the center of the cell is unaffected by any excess surface charge. Thus, we choose the proton in the center of the cell at $\Delta V = 0V$ as the reference state, which approximates the bulk proton not influenced by surface charge:

$$F_{H^+} \left(\Delta V = 0, z = \frac{D}{2} \right) = 0$$

For our simulation cell, setting $\Delta V = 1 V$ creates an electric field near the middle of the cell on the order of $0.01V/\text{\AA}$, small enough to neglect entropic effects

from minor changes in bulk structure of water and the solvation shell of the proton. Thus, the only significant change in free energy of the proton is due to the electrostatic potential:

$$F_{H^+}(\Delta V = v, z) - F_{H^+}(\Delta V = 0, z) = zF(\phi_{H^+}(\Delta V = v, z) - \phi_{H^+}(\Delta V = 0, z))$$

In the simulation, the total electrostatic potential of the solvated proton can be decomposed as follows:

$$\phi'_{H^+,tot}(\Delta V, z) = \phi'_{sol} + \phi'_{img}(z) + \phi'_\sigma(\Delta V, z)$$

Where ϕ'_{sol} is the contribution from the solvation of the proton, ϕ'_{img} is the contribution from primary image charges, and ϕ'_σ is the contribution from the higher-order images and excess surface charge on the metal electrodes. We use the prime notation to indicate a Madelung potential is used. Since ϕ'_{img} varies with z , we connect the free energies for two simulations at constant z . Choosing $z = D/2 = 25 \text{ \AA}$, we can calculate the proton free energy change when the potential difference $\Delta V = v$ is switched on:

$$\begin{aligned} F_{H^+}(\Delta V = v, z = \frac{D}{2}) - F_{H^+}(\Delta V = 0, z = \frac{D}{2}) \\ = zF(\langle \phi'_{H^+,tot}(\Delta V = v, z = \frac{D}{2}) \rangle - \langle \phi'_{H^+,tot}(\Delta V = 0, z = \frac{D}{2}) \rangle) \end{aligned}$$

where the ensemble average of $\phi'_{H^+,tot}$ is performed for a solvated proton at fixed z .

When we perform importance sampling and obtain free energy surfaces as a function of ΔE and z , we can similarly establish a common energy scale. Given two free energy surfaces $F_{H^+}^{(1)}(\Delta E, z)$ and $F_{H^+}^{(2)}(\Delta E, z)$ for ET calculations performed at different cell voltages, we can connect the energy scales across voltages by the following:

$$\begin{aligned} F_{H^+}^{(2)}(\Delta E = \Delta e_{\min}, z = \frac{D}{2}) - F_{H^+}^{(1)}(\Delta E = \Delta e_{\min}, z = \frac{D}{2}) \\ = zF(\langle \phi'_{H^+,tot}(\Delta V = v, z = \frac{D}{2}) \rangle - \langle \phi'_{H^+,tot}(\Delta V = 0, z = \frac{D}{2}) \rangle) \end{aligned}$$

where the connection is performed at Δe_{min} , which is the solvent coordinate value corresponding to equilibrium solvation for the proton. Similarly, the statistics collected for ϕ'_{H^+} are at equilibrium solvation, i.e., no harmonic restraint with respect to ΔE . In our results, we have used the connection formula to establish a common reference for all cell voltages evaluated.

Coordination Numbers of water around H^\ddagger

From our adiabatic free energy calculations for the Volmer step, we see that the reduction transition state occurs later, i.e., at greater solvent polarization, when the Pt surface is negatively charged. Here, we quantify the change in the solvation structure at the transition state by plotting coordination numbers (CNs) of waters solvating H^\ddagger . In Figure A.8, the CNs for both water-hydrogens and water-oxygens are shown. The CNs are calculated by de-biasing statistics from a single biased simulation where the proton is harmonically restrained in ΔE and z to the saddle point on the adiabatic 2D surface.

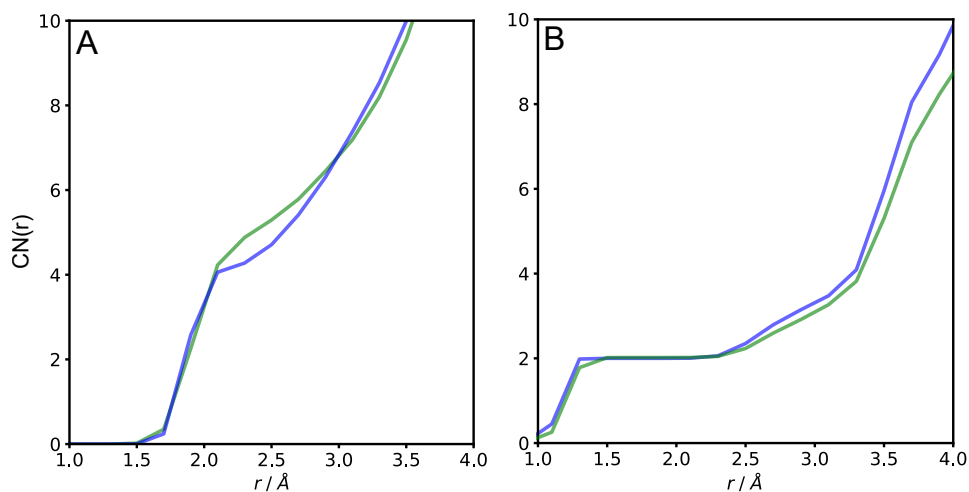


Figure A.8. Coordination numbers (CN) of water atoms around redox H at the transition state from adiabatic ET simulations. Here we set $\epsilon_a - \epsilon_f = -10.2$ eV. A) H^\ddagger / water-hydrogen CNs. B) H^\ddagger / water-oxygen CNs. At $V - V_{pzc} = -2$ V, there is higher water-H density near H^\ddagger around $r = 2.5$ Å and slightly lower water - O density in the 2nd layer of solvating waters, $r > 2.5$ Å. Since H^\ddagger has a partial positive charge, the change in CNs imply less attractive H^\ddagger /water interactions, thus the solvent is polarized further away from equilibrium solvation at the negative voltage transition state. (Blue: electrode at $V - V_{pzc} = 0$ V, Green: $V - V_{pzc} = -2$ V.)

Appendix B

SUPPLEMENTARY INFORMATION FOR CHAPTER 4

Cs⁺ Cylindrical Pair Correlation Functions

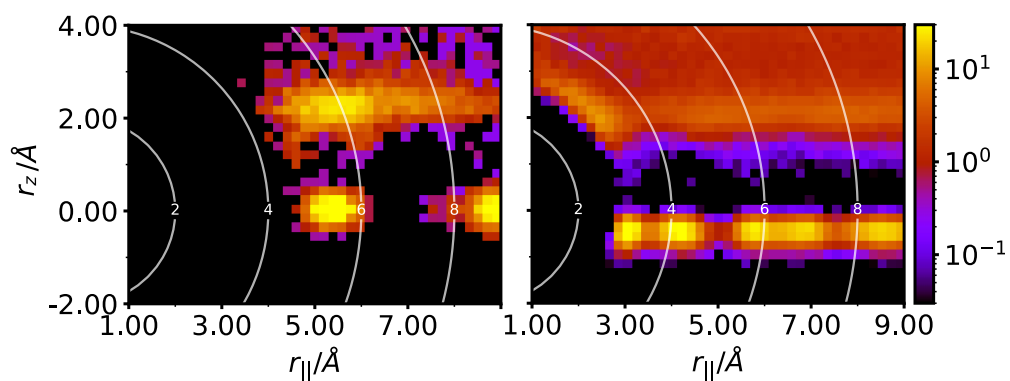


Figure B.1. Surface Cs⁺ cylindrical pair correlations. A) conditional pair correlations between surface Cs⁺ atoms (within $z < 3\text{\AA}$ of the surface) and A) other Cs⁺ atoms, B) water oxygen atoms. The average spacing between surface Cs⁺ atoms is about $r_{||} = 5.2\text{\AA}$, which is slightly smaller than the diameter of the first solvation shell of $d \cong 6\text{\AA}$, indicating a high degree of overlap between OHL Cs⁺ solvation shells.

H⁺ Radial Distribution Functions

As H⁺ migrates through the double layer in the HOR/HER process, the distribution of electrolyte species around the proton changes significantly, shown in Figure B.2. In Figure B.2A, as H⁺ approaches the surface, the peak of the Cs⁺ distribution increases, becoming increasingly ordered when $z = 2\text{\AA}$. In Figure B.2C, the H⁺ / Na⁺ ions are essentially uncorrelated even as H⁺ approaches the surface since Na⁺ does not adsorb.

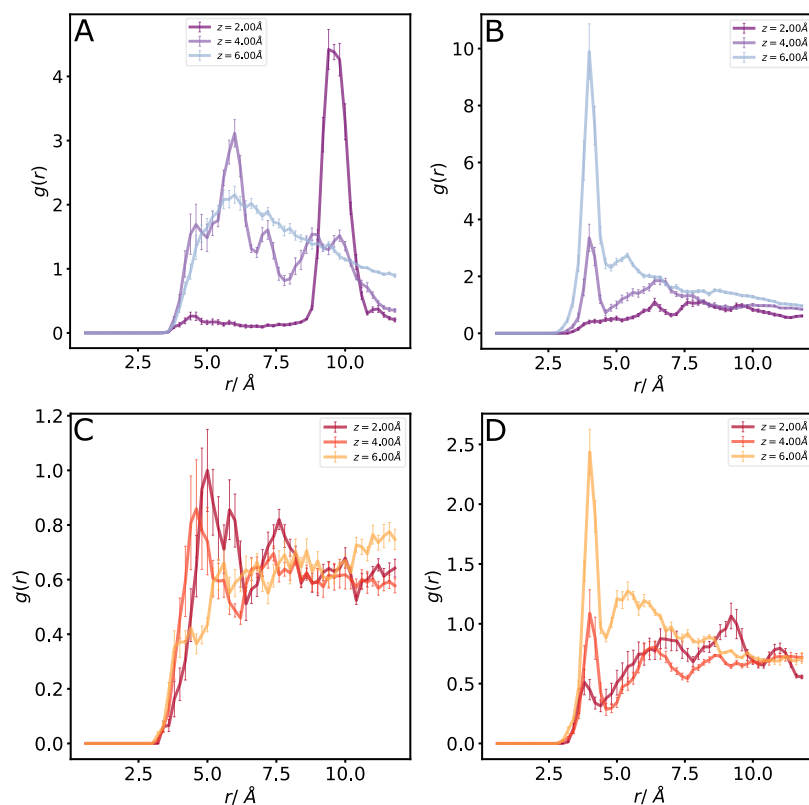


Figure B.2. Radial distribution functions of electrolyte ions around H⁺ at various fixed distances z from the Pt surface. The surface potential is set to $V - V_{\text{pzc}} = 0\text{ V}$. A) H⁺/Cs⁺ RDFs in 1M CsCl, B) H⁺/Cl⁻ RDFs in 1M CsCl, C) H⁺/Na⁺ RDFs in 1M NaCl, D) H⁺/Cl⁻ RDFs in 1M NaCl. Error bars are estimated from the variance in distribution function bin block averages after dividing the trajectories into five blocks.

Diabatic free energies for H^+/H redox in 1M CsCl and 1M NaCl

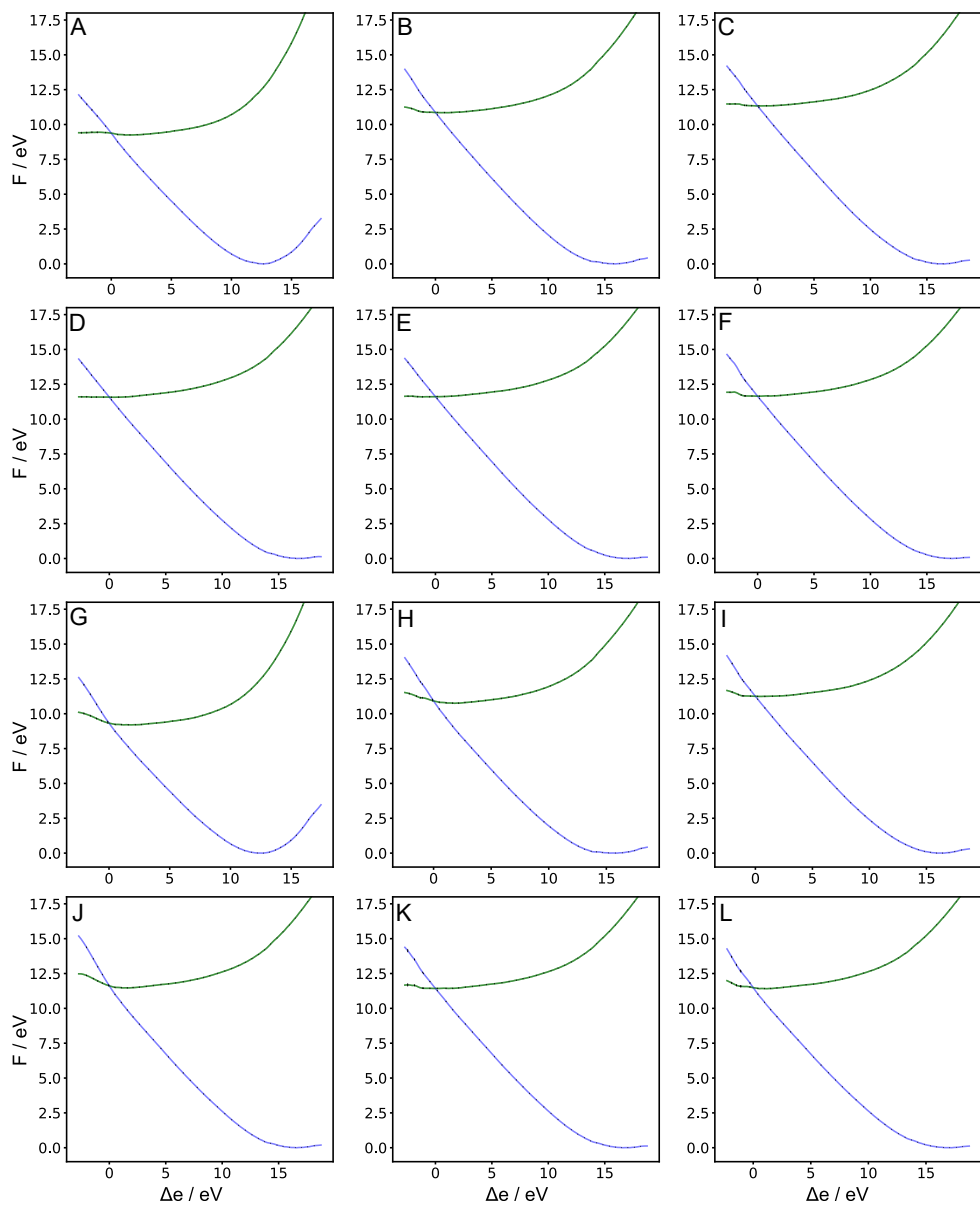


Figure B.3. Diabatic free energy curves for H^+/H redox at fixed z ; used to produce Figure 4.3. A-F) Free energies in 1 M CsCl where z of Green: neutral H free energies F^H calculated from $F^H(\Delta e) = F^{H^+}(\Delta e) + \Delta e$. Error bars are shown but are small.

Cylindrical pair correlation functions for OHL Cs⁺ atoms

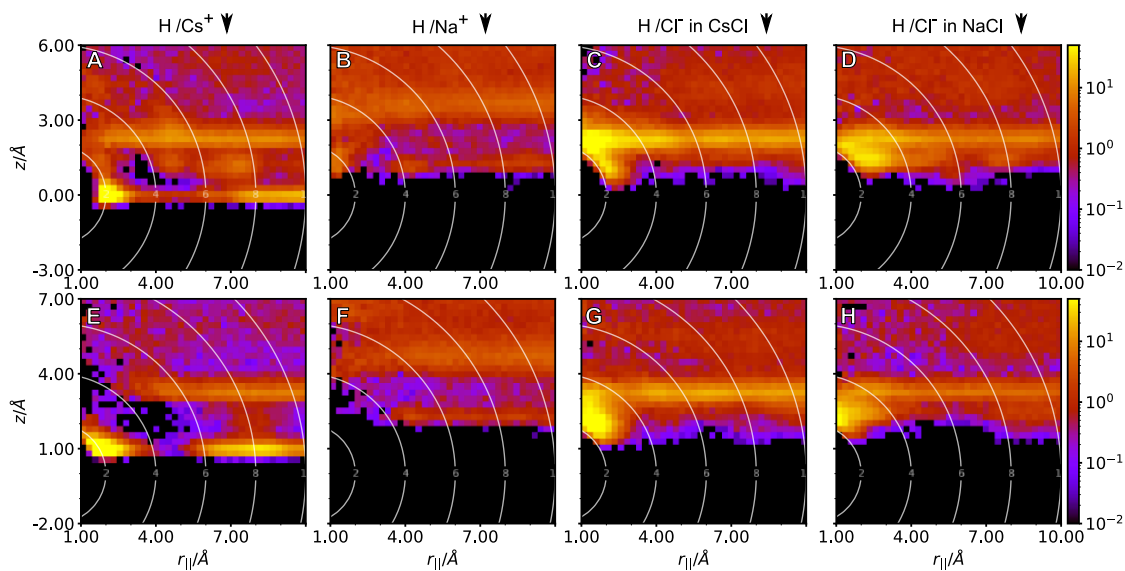


Figure B.4. Cylindrical pair correlation functions $\rho_{ij}/\rho_{\text{bulk}}$ between the reduced redox H at fixed z and supporting electrolyte ions in 1 M CsCl and in 1 M NaCl. A-D) $z = 3 \text{ \AA}$, E-H) $z = 2 \text{ \AA}$. From left to right, the columns correspond to H/Cs⁺, H/Na⁺, H/Cl⁻ in CsCl, H/Cl⁻ in NaCl. Gray curves on the plot correspond to radial distance isolines $r = (r_{||}^2 + r_z^2)^{1/2}$.

Hydrogen bonding and water dipole angle distributions for waters adsorbed on Pt (111)

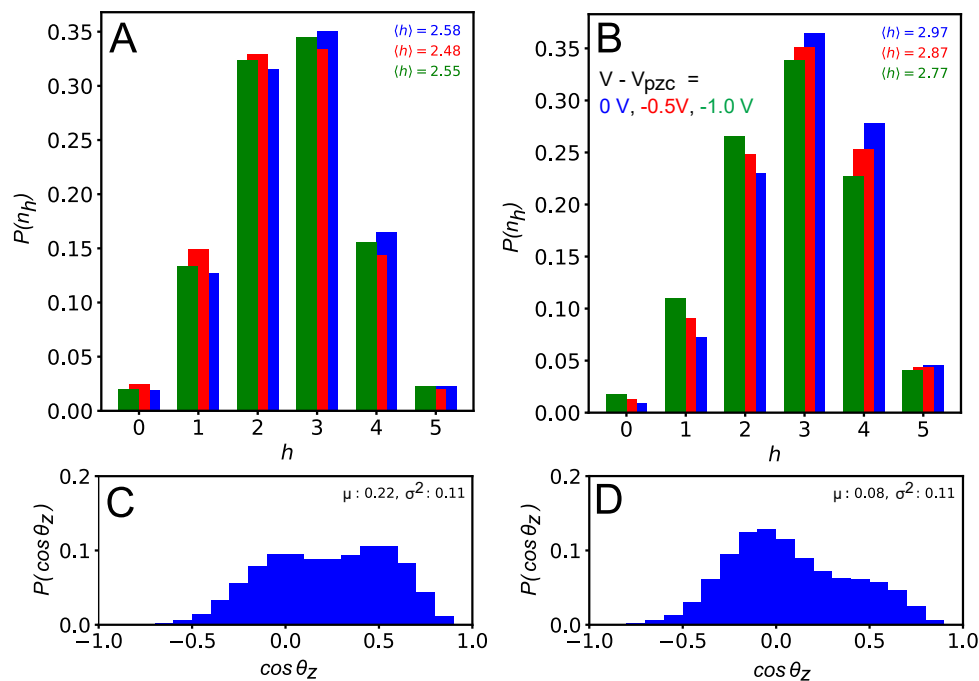


Figure B.5. Adsorbed water hydrogen bonding & water dipole angle statistics.

Water molecules are included in the statistics if its oxygen z position is less than $z = 3.0 \text{ \AA}$. Statistics are collected from a trajectory of 10 ns with no proton included in the cell. A) Mean and distribution of the number of hydrogen bonds (donors + acceptors) per adsorbed water in 1 M CsCl and B) 1 M NaCl. C) Distribution of water dipole vector angles with respect to the surface normal vector in 1 M CsCl at $V - V_{pzc} = 0$ V and D) 1 M NaCl. Cs^+ adsorption is more favorable and significantly disrupts hydrogen bonding. As the surface potential is set more negatively, Na^+ has a stronger tendency to migrate to the surface and disrupt the hydrogen bonding network. Cs^+ decreases the number of water molecules hydrogen bonded parallel to the surface compared to Na^+ . Instead, more water hydrogens point away from the surface.